ALFRED-WEGENER-INSTITUT
HELMHOLTZ-ZENTRUM FÜR POLAR- UND MEERESFORSCHUNG

Universität Bremen

University of Bremen

Doctoral Thesis

Climate - cryosphere interactions for past, present and future climates with the comprehensive Earth system model AWI-ESM

Author:
Lars Ackermann

Supervisor & First Reviewer:
Prof. Dr. Gerrit Lohmann
Second Reviewer:
Prof. Dr. Sergey Danilov

A thesis submitted in fulfillment of the requirements
for the degree of doctor rerum naturalium (Dr. rer. nat.)

in Physics/Electrical Engineering
Faculty 1

Date of Submission: July 31, 2023

Date of Defence: November 27, 2023

Abstract

Ice sheets constitute an important component of Earth's climate system. They affect Earth's reflectivity due to their high albedo, alter topography, and act as a source and sink for vast amounts of fresh water. During the late Pleistocene, Northern Hemisphere ice sheets repeatedly grew and declined, substantially affecting global sea level. On shorter time scales, freshwater discharge affects ocean dynamics like deep-water formation in the North Atlantic or the Southern Ocean, with implications for global climate. Enhancing the understanding of these processes is key for long-term future climate projections. Earth system models (ESM) are a meaningful tool for investigating the processes involved in climate-cryosphere feedbacks, but only recently computational resources allow for such comprehensive model applications.

The Alfred Wegener Institute Earth System Model (AWI-ESM) is applied to study the role of the Greenland Ice Sheet (GIS) in different future warming scenarios. The model includes an interactive Ice Sheet Model (ISM) to capture ice sheet dynamics and enhance the representation of spatial freshwater discharge. The ISM leads to a strong decadal variability to the freshwater release, resulting in intervals in which it reduces the surface runoff by high accumulation rates. This compensating effect is missing in climate models without dynamic ice sheets.

To investigate processes involved in the buildup phase of ice sheets, transient simulations of the Last Glacial Inception (LGI) are performed. These cooling climate simulations complement the future warming scenarios. The model is run asynchronously from 125 ka to 110 ka with prescribed orbital and greenhouse gas forcing. Large-scale glaciation occurs in a simulation with implemented anomaly coupling. This anomaly coupling is applied to compensate for model biases in high-latitude near-surface air temperature. Large areas of Quebec and Baffin Island glaciate, mainly driven by the thickening of snowfields.

In order to assess the effects of heat and freshwater fluxes by iceberg melting on deep-ocean characteristics, multi-centennial simulations under fixed pre-industrial forcing are run with a fully coupled ESM including interactive icebergs. Compared to simulations without interactive icebergs, the results show a cooling of deep ocean water masses and enhanced deep water formation in the continental shelf area of the Ross Sea, a process commonly underestimated by current climate models. The results emphasize the importance of realistically representing both heat and freshwater fluxes in the high southern latitudes.

Publications

Ackermann, L., C. Danek, P. Gierz, and G. Lohmann (2020). "AMOC Recovery in a multicentennial scenario using a coupled atmosphere-ocean-ice sheet model". In: *Geophysical Research Letters* 47.16.

Ackermann, L., P. Gierz, G. Knorr, and G. Lohmann (2023a). "Simulating the last glacial inception with a comprehensive earth system model including interactive ice sheets". In: *in preparation.*

Ackermann, L., T. Rackow, K. Himstedt, P. Gierz, G. Knorr, and G. Lohmann (2023b). "A comprehensive Earth System Model (AWI-ESM) with interactive icebergs: Effects on surface and deep-ocean characteristics". In: *in preparation.*

Matos, F. D. A. O., D. Sidorenko, P. Gierz, X. Shi, L. Ackermann, and G. Lohmann (2022). "z-and ρ-AMOC under pre-industrial, historical and abrupt 4xCO2 climates in AWI-ESM2.1". In: *Authorea Preprints.*

Sokolova, N., F. Dahlke, M. Butzin, L. Ackermann, B. T. Schwertfeger, H.-O. Pörtner, and G. Lohmann (2023). "Growth and reproductive capacity of Atlantic cod (Gadus morhua) under future warming". In: *in preparation.*

Acknowledgements

Many thanks to my doctoral supervisor Prof. Gerrit Lohmann for his academic support and his trust, which enabled me not to lose heart even during difficult times.

Special thanks also to Paul Gierz for his patient support with the models and the HPC infrastructure and to Gregor Knorr for his ever-listening ear and valuable scientific comments.

Many thanks to Thomas Rackow for helping with the iceberg model and to Stephan Krätschmer for tips and helpful feedback about the PhD thesis.

Furthermore, I would like to thank the ESM-tools developers for their great support that made it possible for me to run my simulations in the first place.

Many thanks also to the entire Paleoclimate Dynamics section for the great willingness to help, the nice chats, and the very pleasant working atmosphere.

And last but not least many thanks to my family and all my friends for their emotional support and their patience during the last three and a half years. Especially times during the Corona pandemic were challenging but I could always rely on people being there for me during personal crises. I would not have been able to write this thesis without all of this support.

Contents

List of Acronyms

AABW	Antarctic Bottom Water
ACC	Antarctic Circumpolar Currenet
AMOC	Atlantic Meridional Overturning Circulation
AWI	Alfred Wegener Institute
AWI-CM	AWI Climate Model
AWI-ESM	AWI Earth System Model
CMIP	Coupled Model Intercomparison Project
dEBM	diurnal Energy Balance Model
EMIC	Earth System Model of Intermediate Complexity
ESM	Earth System Model
FESOM	Finite Element Sea Ice Ocean Model Finite volumE Sea Ice Ocean Model
GHG	Greeenhouse Gas
GIS	Greenland Ice Sheet
IPCC	Intergovernmental Panel on Climate Change
ISM	Ice Sheet Model
ISMIP	Ice Sheet Model Intercomparison Project
LGI	Last Glacial Inception
LIG	Last Interglacial
LGM	Last Glacial Maximum
NADW	North Atlantic Deep Water
PDD	Positive Degree-Day

PI	Pre-Industrial
PICO	Potsdam Ice-shelf Cavity mOdel
PISM	Parallel Ice Sheet Model
PMIP	Paleoclimate Model Intercomparison Project
SST	Sea Surface Temperature
SSS	Sea Surface Salinity
THC	Thermohaline Circulation
WAIS	West Antarctic Ice Sheet

List of Figures

List of Tables

.

1. Introduction

1.1 Motivation

Interactions between ice sheets and other Earth system components play a crucial role in our planet's climate. Ice sheets repeatedly advance and retreat on time scales of several ten to hundred thousand years. For the last one million years, these glacial cycles have occurred with a periodicity of roughly 100 kyr. While it is commonly accepted that the large-scale variations in ice-sheet buildup and retreat are driven by changes in the orbital parameters, the processes involved are more complex. Several feedbacks between the climate system and the cryosphere play a role in the dynamic response of climate and ice sheets to changes in orbital parameters.

Improving the understanding of these processes is critical for assessing ice sheets' role in future climate change scenarios. Ice sheets affect Earth's climate in several ways. As significant sources and sinks of freshwater, they interact with the global hydrological cycle and hence affect global sea level. For instance, the giant ice sheets present over North America and Europe during the Last Glacial Maximum (LGM) bound vast amounts of water, which resulted in a global sea level decrease by over 120 m (Clark and Mix, 2002; Peltier, 2002) compared to the present day. Of all the Northern Hemisphere ice sheets present at the LGM, only the Greenland Ice Sheet (GIS) remains today. The freshwater amount stored in the Greenland and Antarctica Ice Sheets would result in a sea level rise by 7 m and 58 m, respectively, in case of complete melting.

While this process would take several millennia, the GIS and the West Antarctic Ice Sheet (WAIS) may already be close to tipping points (Armstrong McKay et al., 2022; Boers and Rypdal, 2021; Lenton et al., 2019; Pattyn and Morlighem, 2020; Rosier et al., 2021). Exceeding these tipping points might result in an irreversible ice mass loss and an increasing sea level rise over the next millennia. The risk of passing these tipping points increases with accelerating GIS and WAIS melt rates, as observed by Bamber et al. (2018) for the last decades.

Today we know that past climate model projections were too conservative regarding global sea level rise (Rahmstorf et al., 2012), and uncertainties are still high (IPCC, 2022). Hence, further model development and process understanding are necessary to improve future sea level rise projections.

Besides its implications for the global sea level, freshwater fluxes from land ice melting also affect ocean characteristics. In the Northern Hemisphere, freshwater fluxes from the GIS may affect the deep water formation and weaken the Atlantic Meridional Overturning Circulation (AMOC) (Rahmstorf et al., 2015). The AMOC is a crucial component of Earth's climate system that transports a significant amount of heat from low to high northern latitudes. An essential part of this overturning circulation is the deep water formation in the North Atlantic, a process that depends on density gradients. As seawater density is a function of salinity and temperature, it is affected by freshwater and temperature perturbations.

Observations and reconstructions of sea surface temperature (SST) suggest a weakening of the AMOC over the last century due to increasing atmospheric CO_2 concentrations and the associated global warming (Dima and Lohmann, 2010; Dima et al., 2021; Rahmstorf et al., 2015). This is consistent with findings by model studies that simulate an AMOC weakening in future global warming scenarios (Manabe and Stouffer, 1993; Stocker and Schmittner, 1997; Weaver et al., 2012). Next to increasing atmospheric and oceanic temperatures, the potential increase in GIS related meltwater release into the North Atlantic may have implications on deep water formation and AMOC stability (Bryan, 1986; Clark et al., 2002; Manabe and Stouffer, 1995; Rahmstorf, 2002). With future global warming, the increasing trend of mass loss from the GIS is assumed to continue (Masson-Delmotte et al., 2021). To assess the potential implications of an increased GIS meltwater runoff for future AMOC stability, several model studies have been performed (e.g. Gierz et al. (2015), Golledge et al. (2019), Manabe and Stouffer (1995), Mikolajewicz et al. (2007), and Swingedouw and Braconnot (2007)). While most studies show a weakening effect of increased GIS melt on the AMOC, uncertainties remain with respect to the amplitude of the future AMOC slowdown and the processes involved due to limitations in the model setup and model resolution.

In the Southern Hemisphere, freshwater fluxes from the Antarctic Ice Sheet (AIS) may weaken the formation of Antarctic Bottom Water (AABW) (Purkey and Johnson, 2013; Silvano et al., 2018; Williams et al., 2016). These water masses formed over the continental shelves of Antarctica are part of the AMOC

and constitute the densest water masses in the global ocean (Johnson, 2008; Orsi et al., 1999). By sinking along the shelves, they play an important role in carbon sequestration (De Lavergne et al., 2014; Marinov et al., 2006) and oxygen supply of the deep ocean (Gordon, 1966; Orsi et al., 1999). Furthermore, the Southern Ocean plays an important role in Earth's heat budget and the uptake of heat due to anthropogenic global warming (Frölicher et al., 2015; Manabe et al., 1990).

In contrast to Greenland, there are large ice shelves around Antarctica. Their disintegration leads to the calving of icebergs which act as a transport medium for fresh water and latent heat. For the Antarctic Ice Sheet, estimates for the discharge of icebergs range from around 50% (Depoorter et al., 2013) to about 75% (Jacobs et al., 1992) of its approximately 2,700 Gt yr^{-1} of freshwater input into the ocean. The other main contributor is basal melting at the base of ice shelves. In comparison, the mass balance of the GIS is dominated by the discharge of small outlet glaciers that accounts for approximately a third to one-half of freshwater discharge into the ocean (Benn et al., 2017) and the residual being surface melting and runoff.

Icebergs not only play a significant role in the ice sheet's mass balance but alter ocean conditions. In contrast to surface runoff and basal melting, the effects of iceberg discharge onto the ocean do not necessarily occur close to the ice sheet. By exporting ice from near-coastal regions, icebergs play an important role in the spatial redistribution of freshwater input in the Southern Ocean (Stern et al., 2016). This leads to enhanced salinity in regions of freshwater export and decreased salinity in regions of freshwater input by iceberg melting. Together with a local cooling effect due to the uptake of latent heat from the surrounding ocean, the melting of icebergs has implications for sea-ice formation as well as for the deep convection and the formation of AABW in the Southern Ocean. Furthermore, icebergs affect ocean dynamics by their shear dimension (Grosfeld et al., 2001; Stern et al., 2015) and are a source of iron input into the ocean, potentially fertilizing the ocean's biosphere (Raiswell et al., 2008).

As icebergs can travel long distances, these processes might act at locations far away from the ice sheet they originate from. For example, reconstructions of iceberg trajectories by Starr et al. (2021) suggest net freshwater import into the Atlantic by far-traveling icebergs originating from the Southern Ocean during past glacials, eventually resulting in an AMOC slowdown. Effects like this can only be modeled with explicit representation of interactive icebergs. However, icebergs are commonly not represented in a complex Earth System Model (ESM).

Their freshwater and heat fluxes are rather modeled in a simplified way by homogeneously distributing them near coastal regions.

But not only the ocean is affected by ice sheet dynamics. Also, atmospheric circulations are altered by topographic changes in the ice sheets. The ice-elevation feedback constitutes a positive feedback loop. As ice sheets grow, the atmospheric near-surface temperature drops with increasing elevation, fostering further ice sheet growth. During an ice sheet decline, it is the other way around. Near-surface temperatures decrease, accelerating ice sheet melting. Another climate-ice sheet interplay involves the surface albedo. Glaciated surfaces have a higher albedo than non-glaciated surface areas. Hence, an expanding ice sheet leads to a higher reflection of short-wave radiation and less heat uptake by the underlying soil. Again, the process is reversed when the ice sheet retreats: the newly unglaciated soil absorbs more heat and warms, leading to an even faster glacier retreat.

Despite their importance, ice sheets were not explicitly included in ESMs until one to two decades ago due to computational costs. Long-term responses of ice sheets to atmospheric and oceanic changes have been simulated in hindsight instead (Flato et al., 2014): ice sheet models were forced with climate model output, neglecting any feedback from the ice sheet to the atmosphere and ocean, respectively. Only recently, sophisticated coupled climate-ice sheet models have emerged that can simulate specific processes involved in the climate-ice sheet interactions. However, the climate component of these coupled climate ice sheet models is commonly an Earth System Model of Intermediate Complexity (EMIC) (Claussen et al., 2002) or is limited by a rather coarse resolution (e.g., Charbit et al. (2008), Driesschaert et al. (2007), Gierz et al. (2015), Huybrechts et al. (2011), and Vizcaíno et al. (2008)). Complex coupled climate-ice sheet models have been included in the Coupled Model Intercomparison Project (CMIP) and the associated Ice Sheet Model Intercomparison Project (ISMIP) for the first time in its sixth and fourth phases, respectively (Nowicki et al., 2016).

Also, for long-term paleoclimate simulations, most studies use an EMIC as the climate component (e.g., Bahadory et al. (2021), Calov et al. (2005a), Calov et al. (2005b), Ganopolski et al. (2010), and Ganopolski and Brovkin (2017) for simulations of the last inception or a full glacial cycle). While EMICs enable fast multi-ensemble simulations, they have a coarse resolution and simplified physics and hence miss an explicit representation of important feedbacks involved in ice-climate interactions. However, they may include processes of several Earth

system components by parameterization, like, for example, the effect of dust on ice albedo in Ganopolski et al. (2010) and Willeit and Ganopolski (2018). Studies using more complex models commonly simulate several time slices with the climate component and force the ice-sheet component in between (e.g., Herrington and Poulsen (2011) and Ridley et al. (2010)). However, these model studies lack an actual transient response of climate and ice sheets.

Only recently, the advances in computing power have allowed for transient simulations with complex coupled climate-ice sheet models spanning multi-centennial or multi-millennial time scales.

1.2 Objectives

The work presented in this thesis has been conducted within the scope of the PalMod project, which aims for an improved understanding of slow interactions within the Earth system. This enhanced understanding and the advancement of ESMs shall enable improved multi-millennial future climate projections. The second phase of the project (during which this thesis was written) aimed to complete model development and run transient simulations covering parts of the last glacial cycle. New model development, presented in this study, addresses the coupling of a complex ESM with an interactive Ice Sheet Model (ISM) that is applied to future scenarios and the Last Glacial Inception (LGI) (Chapters 4 and 5, respectively) as well as the implementation of an interactive iceberg model (Chapter 6). The focus of this work is the comprehensive modeling of interactions between the climate system and ice sheets and icebergs, respectively, as different cryosphere components, aiming for an improved process understanding.

Therefore, the following research questions are addressed:

1. **What is the effect of an interactive Greenland Ice Sheet on freshwater discharge in a complex coupled Earth system model?** (Chapter 4)
   Freshwater fluxes from ice sheet discharge are often parameterized, neglecting a realistic spatial distribution and internal ice sheet variability. This might induce systematic biases in future climate projections. Model studies show that a realistic spatial representation of melt-induced freshwater inflow into the ocean is crucial for an accurate assessment of its effect on the AMOC (Liu et al., 2018) and on deep water formation in the North Atlantic (Eden and Böning, 2002; Schmidt and Send, 2007; Wang

et al., 2018; Yang et al., 2016). Fully coupled climate-ice sheet models that have been used for modeling studies were limited with respect to resolution, the coupling, or the forcing applied (Driesschaert et al., 2007; Gierz et al., 2015; Golledge et al., 2019; Lenaerts et al., 2015; Mikolajewicz et al., 2007). Here, a newly developed Earth system model is used to assess the effects of an interactive ice sheet model, which covers the GIS domain, on freshwater discharge in future scenario runs.

2. **Is the model able to initiate large-scale glaciation in a coupled transient simulation?** (Chapter 5)
   Complementary to the future warming scenarios, the coupled climate ice sheet model shall be forced with orbital parameters and greenhouse gas concentrations of cooling climate conditions. With this transient simulation, it shall be tested whether the model can initiate large-scale glaciation. A suitable interval for this experiment is the LGI which occurred between 120 ka and 110 ka. However, the extent and exact timing of the glaciation is not well-constrained. Estimates for global sea level drop by 110 ka and the associated additional total land ice volume compared to today range from 10 m to 70 m (Hasenclever et al., 2017). North American ice sheets are assumed to have contributed significantly to this sea level drop. Furthermore, there are uncertainties about the processes involved in large-scale ice sheet buildup. Two hypotheses prevail about the characterization of large-scale inception of North America: 1) ice sheet buildup is caused by large-scale thickening of snowfields (Andrews and Mahaffy, 1976). Hence, surface mass balance changes induced by variations in surface temperature and precipitation are key for glaciation. And 2) small-scale high-elevation ice sheets act as nuclei (Weertman, 1964). Here, glaciation depends more on internal ice sheet dynamics. As the geological record of the LGI is vastly destroyed by subsequent glaciations, ESM's are an important tool for improving the understanding of processes involved in the LGI. Here, transient long-term simulations with the coupled climate-ice sheet model are used to assess the drivers of large-scale glaciation during the LGI.

3. **What are the effects of interactive icebergs on deep ocean water characteristics on long-time scales?** (Chapter 6)
   Despite their importance, icebergs are rarely represented in ESMs in detail, and if accounted for, their effects on ocean conditions are often only neglected or parameterized (Devilliers et al., 2021). Freshwater fluxes

from iceberg melting are distributed either homogeneously over a specific area or are treated as surface runoff, entering the ocean directly at coastal regions. Previous model studies focussed on the representation of single iceberg trajectories (Bigg et al., 1997; Rackow et al., 2017) or the effects of heat and freshwater fluxes on surface conditions (Stern et al., 2016; Jongma et al., 2009; Martin and Adcroft, 2010). However, in paleoclimate and future scenario simulations, the long-term effects of iceberg discharge might affect deep ocean water masses. In this chapter, these effects are assessed with a newly developed ESM including interactive icebergs. The model icebergs are seeded in the Southern Ocean, representing a present-day size-distribution. This chapter aims at a process understanding, and simulations are done with fixed pre-industrial climate conditions.

This thesis is structured as follows: Chapter 2 gives an overview of the climate system, its different components, and important processes. Chapter 3 gives an explanation of the model used and the coupling of its different components. Chapter 4 has been published in Ackermann et al. (2020) in *Geophysical Research Letters*. Chapter 5 shows the current status of the research and is in preparation (Ackermann et al., 2023a). Chapter 6 will be submitted to *Geoscientific Model Development* (Ackermann et al., 2023b).

2. Theory

2.1 The climate system

The Intergovernmental Panel on Climate Change (IPCC), an intergovernmental body of the United Nations, which regularly reviews and summarizes the state of the art of climate science, and informs the public and governments about it, defines climate as follows:

"Climate in a narrow sense is usually defined as the average weather, or more rigorously as the statistical description in terms of the mean and variability of relevant quantities over a period of time ranging from months to thousands or millions of years. The classical period for averaging these variables is 30 years, as defined by the World Meteorological Organization. The relevant quantities are most often surface variables such as temperature, precipitation and wind. Climate in a wider sense is the state, including a statistical description, of the climate system." (IPCC, 2018).

Furthermore, the IPCC divides the climate system into five components:

The **Atmosphere** is the gaseous skin of the Earth, which can be divided into four layers: the troposphere, the stratosphere, the mesosphere, and the thermosphere (Wallace and Hobbs, 2006). The lowest one, the troposphere, contains around 80% of the atmosphere's mass (Wallace and Hobbs, 2006) and is the layer in which cloud formation and weather phenomena occur (Kikstra et al., 2022). The atmosphere consists mainly of N_2 (78%), O_2 (21%), and Ar (0.9%). Other trace gases represent only a small share but play important roles in the hydrological cycle (e.g., H_2O), global carbon cycle (e.g., CH_4), and the greenhouse gas effect (e.g., H_2O, CO_2, N_2O, CH_4). Because of its low heat capacity and low density, atmospheric processes act on relatively short time scales of weeks to months.

The **Hydrosphere** is the sum of all bodies of liquid surface and subterranean water on Earth. It includes the oceans as saline water masses and all freshwater masses like lakes, rivers, and groundwater (Kikstra et al., 2022). The

largest share of Earth's water masses, namely roughly 97% (Gleick, 1993), is represented by the oceans. Their total mass is approximately 250 times as large as that of the atmosphere (Wallace and Hobbs, 2006). Hence, the oceans constitute an enormous sink for heat and anthropogenic carbon. Processes cover a wide range of temporal and spatial scales, from small-scale eddies to the so-called Thermohaline Circulation (THC), a system of currents and overturning circulations driven by salinity and temperature gradients as well as momentum exchange with the atmosphere. Exchange with the atmosphere and mixing of the upper ocean layer act on relatively short time scales up to months, while the exchange with the deep ocean occurs on millennial time scales.

The **Cryosphere** comprises all frozen water masses at and below the land and ocean surfaces, including snow, glaciers, ice sheets, ice shelves, icebergs, sea ice, and others. Frozen water constitutes around 2.2% (Shikazono and Shikazono, 2012) of Earth's water masses. The largest share is represented by the two ice sheets over the Antarctic continent and Greenland. Ice shelves are the floating parts of ice sheets that cover parts of the ocean surface. When ice breaks off from the ice shelf edge, it is called calving. The calved icebergs float with ocean currents and transport fresh water, heat, and nutrients from ice shelves into the open ocean. Due to their high reflectivity (*albedo*), ice masses have a huge effect on the heat uptake of land and ocean surfaces. While sea ice shows seasonal variability, ice sheet buildup and termination occur on multi-millennial time scales.

The **Lithosphere** is the upper layer of the solid Earth, including its crust and the mainly elastic uppermost part of its mantle (Kikstra et al., 2022). Earth's crust is broken up into continental and oceanic plates. These plates float upon the denser viscous mantle and move a few centimeters per year (Wallace and Hobbs, 2006). Collisions between plates may result in volcanic eruptions and the rise of mountain ranges, e.g., the Himalayas and the Rocky Mountains (Wallace and Hobbs, 2006). Hence, these plate tectonics shape Earth's topography and the sea floor. Furthermore, it affects the global sea level, and exchanges matter, energy and momentum with other Earth system components. The time scales for these processes are in the order of 10^7 to 10^8 years.

The **Biosphere** comprises all living organisms on Earth and their interactions with other Earth system components. Fundamental processes within the biosphere are photosynthesis, which produces biomass from CO_2 and water with energy input from the sun, and respiration, which is the reverse process that

gains energy by biomass depletion. Biomass that is prevented from being decomposed constitutes natural carbon sinks, e.g., coal and oil reservoirs but also peatlands. Hence, the biosphere plays an important role in exchanging carbon, water, and energy with the atmosphere and the ocean. Furthermore, it affects the Earth's albedo, its surface roughness and is a source of aerosols that have implications for the energy budget of the atmosphere. Time scales of biospheric processes range from hours to centuries.

2.2 Processes and feedbacks in the climate system

All of these components are strongly interlinked and exchange several physical and chemical quantities on a broad range of spatial and temporal time scales. Fundamental processes involved are the **Hydrological Cycle** and the **Carbon Cycle**. Figure 2.1 gives a simplified overview of the complex interactions of different Earth system components. No component can be analyzed isolated from the others. To gain a better understanding of Earth system processes, numerical computer models are employed.

Fundamentals for the interactions between the different Earth system components are the exchange of energy, momentum and matter, especially the exchange of water and carbon. In the following, the hydrological and the carbon cycle, respectively, are described.

Water is essential for life as we know it, but it also plays a fundamental role in climatic processes. As mentioned earlier, all liquid water on Earth is summarized in the hydrosphere, while all frozen water is considered as the cryosphere. Water evaporates from the ocean or freshwater bodies and is transported into the atmosphere as water vapor. Associated with the transport of water vapor is the transport of latent heat that is released by condensation in clouds. The condensed water precipitates as rain or snow, either on land where it may infiltrate the soil, is intercepted by vegetation, accumulates as snow and eventually as ice, or feeds surface runoff and eventually enters the ocean. Or it precipitates over the ocean directly, leading to a freshening, i.e., a reduced salinity, in the upper ocean layers. Water stored in land ice, e.g., ice sheets or glaciers, is temporarily removed from this circle, leading to a reduced global sea level. Whenever a body of land ice melts, the water finally becomes part of the hydrological cycle. Hence, processes in the hydrological cycle cover several time

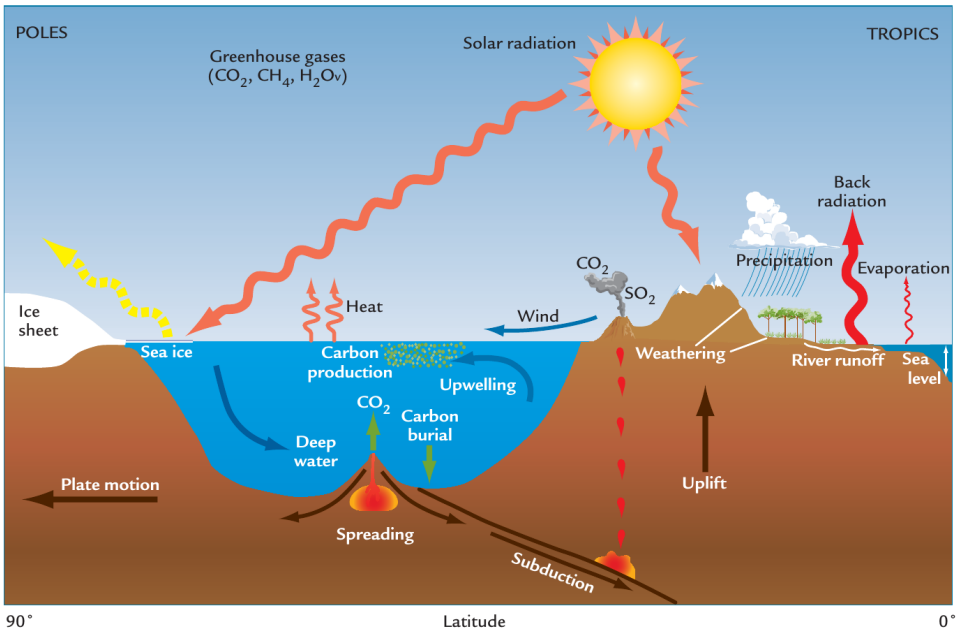

FIGURE 2.1: Simplified sketch of different Earth system components and their interactions. Shown are, for instance, solar radiation as an external forcing and the reflection on ice surfaces; deep water formation and upwelling; parts of the hydrological cycle like evaporation and precipitation; parts of the carbon cycle like outgassing of CO_2 by volcanos and the ocean's role as a carbon sink; and plate tectonics. [Figure taken from Ruddiman (2001)]

scales. An overview of the water masses of different hydrosphere and cryosphere components as well as the different time scales, is given in Table 2.1.

Next to water, carbon plays an extraordinary role in the climate system. Like water, it is exchanged between different Earth system components over several time scales. Carbon is an essential building block of biomass. As mentioned above, carbon dioxide (CO_2) is transformed into biomass by plants. With the chlorophyll in their leaves, they absorb sunlight of specific wavelengths and ultimately convert its energy into chemical energy that is stored in organic compounds. This process transfers carbon from the atmosphere into the biosphere. Respiration reverses this process and releases CO_2 into the atmosphere. If the consumption of biomass is inhibited, e.g., by an insufficient supply of oxygen, dead biomass accumulates over time, resulting in the formation of fossil resources like coal, oil, gas, and peat. Hence, it constitutes a natural carbon sink. Because of its chemical inertia, CO_2 is well mixed and homogeneously distributed within the atmosphere. Due to its absorption of specific longwave radiation, it contributes to the greenhouse effect besides other atmospheric trace

TABLE 2.1: Water masses averaged over Earth's surface and residence times of several components of the hydrosphere and the cryosphere. [Table adapted from Wallace and Hobbs (2006)]

Reservoir of water	Mass [10^3 kg m^{-2}]	Residence time
Atmosphere	0.01	days
Lakes and rivers	0.6	days to years
Groundwater	15	hundreds of years
Alpine glaciers	0.2	hundreds of years
Greenland ice sheet	5	10,000 years
Antarctic ice sheet	53	100,000 years
Oceans	2,700	-

gases like H_2O, N_2O, and CH_4. Methane (CH_4), the other important carbon-based greenhouse gas, has a relatively short lifetime due to its high reactivity. Despite its severe implications for the global climate, atmospheric carbon content constitutes only a marginal fraction of the total carbon within the Earth system. The vast majority of the total carbon is stored in the lithosphere. From here, it is released into the atmosphere and the ocean via weathering and volcanos. However, changes in atmospheric CO_2 due to weathering occur on very long time scales of hundreds of thousands of years (Colbourn et al., 2015). An overview of different carbon reservoirs is given in Table 2.2.

TABLE 2.2: Carbon masses averaged over Earth's surface and residence times of several components of the biosphere and lithosphere. [Table adapted from Wallace and Hobbs (2006)]
[a]) values for reservoir masses and outfluxes are taken from Canadell et al. (2021). Reservoir masses are divided by Earth's surface area of approximately $510 \cdot 10^6$ km^2; residence times are calculated as the ratio of the mass of the reservoir and the outfluxes.

Reservoir of carbon	Mass [10^3 kg m^{-2}]	Residence time
Atmospheric CO_2	1.6	10 years
Biosphere	1.4	days to centuries
Fossil fuels	10	-
Soils and sediments	3	decades to millennia
Sedimentary rocks	100,000	10^8 years
Surface ocean[a]	1.8	years
Intermediate and deep ocean[a]	73	centuries

As mentioned above, the ocean plays a fundamental role in the hydrological cycle but is also important for carbon sequestration and heat redistribution. Therefore, some fundamentals of ocean dynamics are given in the following. The ocean is a highly dynamic Earth system component. The AMOC transports vast amounts of heat from low latitudes to high Northern latitudes. Figure 2.2 gives a very simplified overview of the THC that includes the AMOC (the warm water surface flow indicated by red arrows and the cold water bottom flow indicated by blue arrows in the Atlantic basin). Once the heat is released into the atmosphere in the northern North Atlantic, the water masses cool down, and their density increases. The denser water masses sink down, forming North Atlantic Deep Water (NADW). This cold and relatively salty water flows southward in the deep ocean, constituting the upper cell of the AMOC together with the warm northward flow (Fig. 2.3). The upper cell is complemented by a lower cell. Part of it is the AABW, which originates in the Southern Ocean and flows northward along the abyssal ocean. AABW and NADW mix in the Southern Ocean to form Upper and Lower Circumpolar Deep Water (UCDW, LCDW). This water masses upwell across the Southern Ocean and split at the Antarctic Divergence Zone: one part flows back northward, and the other part flows further southward, carrying heat to the Antarctic ice shelves and contributing to ice shelf melting. Here, these water masses sink down and

become part of the AABW. Antarctic Bottom Water is the densest water mass in the global ocean and can be found at the deepest water levels. It forms above the continental shelves of Antarctica and sinks along the continental slope. Its high density is reached due to cooling and brine release by sea-ice formation (Fig. 2.3).

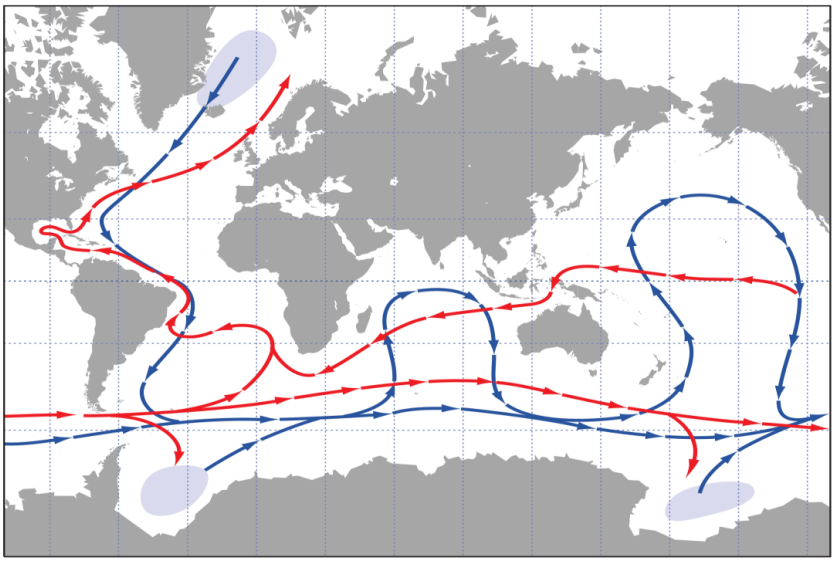

FIGURE 2.2: Simplified schematic of the thermohaline circulation. Blue arrows indicate flows of bottom water, red arrows indicate surface return flows, and shaded areas indicate regions of downwelling. [Figure taken from Ruddiman (2001), adapted from Schmitz Jr (1995)]

The most dominant current in the Southern Ocean is the Antarctic Circumpolar Currenet (ACC). It connects all ocean basins and is the largest ocean current in terms of pathway length as well as in terms of volume transport. At its narrowest position, the Drake Passage, volume transport is around 130 Sv (Cunningham et al., 2003). Due to the lack of topographic boundaries, the ACC flows around Antarctica continuously and constitutes an obstacle for southward flowing warm water masses. This facilitates the distinct and extremely cold climate conditions of the Antarctic continent and the Southern Ocean. The ACC is driven by the strong prevailing westerlies. Furthermore, the westerlies over the Southern Ocean lead to a strong northward Ekman transport, a transport mechanism that occurs in the upper few hundred meters of wind-driven flows due to Earth's rotation and friction. In the Southern Hemisphere, the *Coriolis* force deflects large-scale flows to the left relative to the direction of flow. Hence the prevailing westerlies (eastward flow) lead to a divergent northward Ekman transport. This divergent flow is balanced by large-scale upwelling across the Southern Ocean, so-called *Ekman suction*.

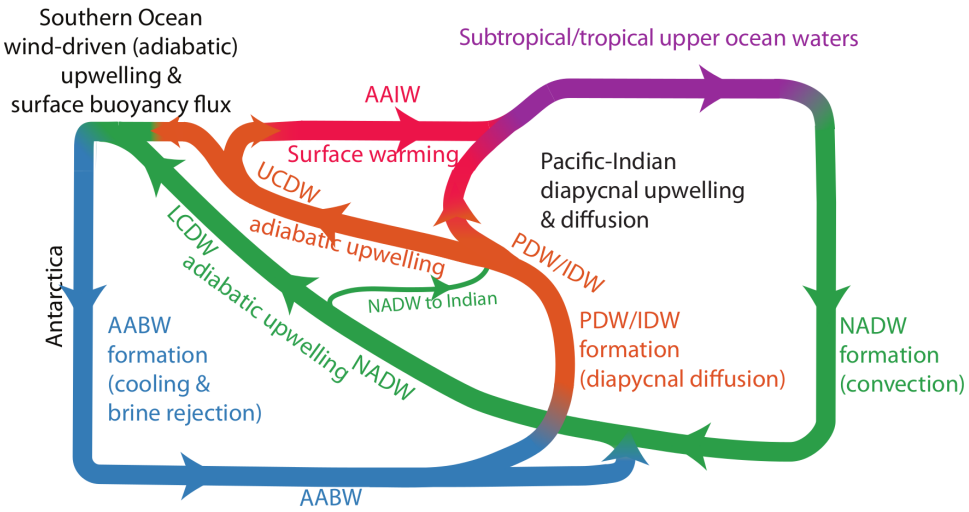

FIGURE 2.3: Simplified two-dimensional schematic of the thermohaline circulation. Depicted are the upper cell with the North Atlantic Deep Water (NADW), upwelling in the Southern Ocean of Lower and Upper Circum Polar Water (LCDW, UCDW) and the return flow of Antarctic Intermediate Water (AAIW); the lower cell with upwelling and the formation of Antarctic Bottom Water (AABW); and the Pacific-Indian Overturning with Pacific and Indian Deep Water (PDW, IDW). [Figure adapted from Talley (2013)]

2.3 Climate change on orbital time scales

An external force for the climate system constitutes the incoming solar radiation. On timescales of 10^4 to 10^5 years (orbital timescales), the incoming solar radiation changes due to variations of orbital parameter, first described by Milankovitch (1941). Earth's orbit around the sun is not entirely circular but rather elliptic. Because of this **eccentricity** (defined as the deviation from a perfectly spherical orbit), the distance between the sun and Earth varies during Earth's revolution around the sun. If the Earth is further away from the sun, the total incoming solar radiation is smaller than during periods of a smaller distance. However, due to Keplers Laws, Earth's velocity increases with increasing distance to the sun, i.e., periods of high insolation are shorter than those with little insolation. The eccentricity changes with a frequency of approximately 100 kyr (Fig. 2.4a). Another parameter, the **obliquity**, is the tilt of Earth's axis with respect to its orbital axis. It varies with a periodicity of around 41,000 years between values of 22.2° and 24.5° (Ruddiman, 2001) (Fig. 2.4b). Due to the tilt, the Northern and Southern Hemispheres of the Earth are exposed differently to the sun during the course of a year, resulting in the seasonal cycle. A stronger tilt results in more intense seasons with higher solar radiation during summer and less incoming radiation during winter. Hence, changes in obliquity mainly affect high latitudes, and implications get weaker towards low latitudes. The third orbital parameter is the direction of Earth's axis, the so-called **precession**. Due to the slow wobbling motion of the Earth, its direction varies over a period of roughly 25,700 years. An additional precessional cycle is the orientation of Earth's orbit. The effective cycle, which determines the date of the equinoxes (the day at which daytime and nighttime are of equal length), is the combined effect of these two cycles, which results in a frequency of about 22,000 years (Fig. 2.4c). As the distance between the sun and the Earth affects Earth's orbital speed, the intensity and duration of the seasons depend on all three orbital parameters.

As mentioned earlier, for the last one million years, ice sheets advanced and retreated with a periodicity of around 100 kyr (Fig. 2.4h). It is commonly accepted that the high Northern summer insolation is the main driver for these glacial-interglacial cycles. However, external forcing alone can not explain the slow buildup and the fast retreat. This indicates that internal climatic feedback amplifies or dampens the forcing signal. Two important climate-ice sheet feedbacks are the ice-elevation feedback and the ice-albedo feedback. The first one describes positive feedback between changes in ice sheet elevation and the

near-surface temperature above the ice sheet. Air temperature in the troposphere decreases with increasing elevation. Warm air that is heated from the ground rises due to its decreasing density and expands. By exapanding, the air cools down with a rate of 9.8 K km^{-1} (dry adiabtic lapse rate). If addtionally, latent heat fluxes by water evaporation and condensation are considered (saturated adiabatic lapse rate), values vary between 4 and 7 K km^{-1} (Wallace and Hobbs, 2006). Because of the lapse rate, an increase in ice sheet height leads to cooler conditions at the ice sheet surface, facilitating an even faster ice sheet growth. On the other hand, a decrease in ice sheet height (i.e., ice sheet melting) leads to warmer surface conditions, enhancing ice sheet melting even further. The second feedback describes a positive feedback between the changes in the reflectance of a surface, i.e., the albedo and ice sheet expansion. Ice has a higher albedo than bare ground, vegetation, or water. Hence, whenever an ice sheet expands laterally, more shortwave radiation is reflected from the newly glaciated surfaces, leading to cooler surface climate conditions and fostering ice sheet growth. However, ice albedo can be decreased by impurities due to the deposition of solid particular matter suspended in air, e.g., mineral dust or soot. Drier climate conditions facilitate dust emission and deposition due to decreased precipitation and the associated washout. As a cooler atmosphere contains less water than a warmer one, the change of ice albedo due to dust deposition constitutes a negative feedback, facilitating ice sheet melt during cold climate conditions.

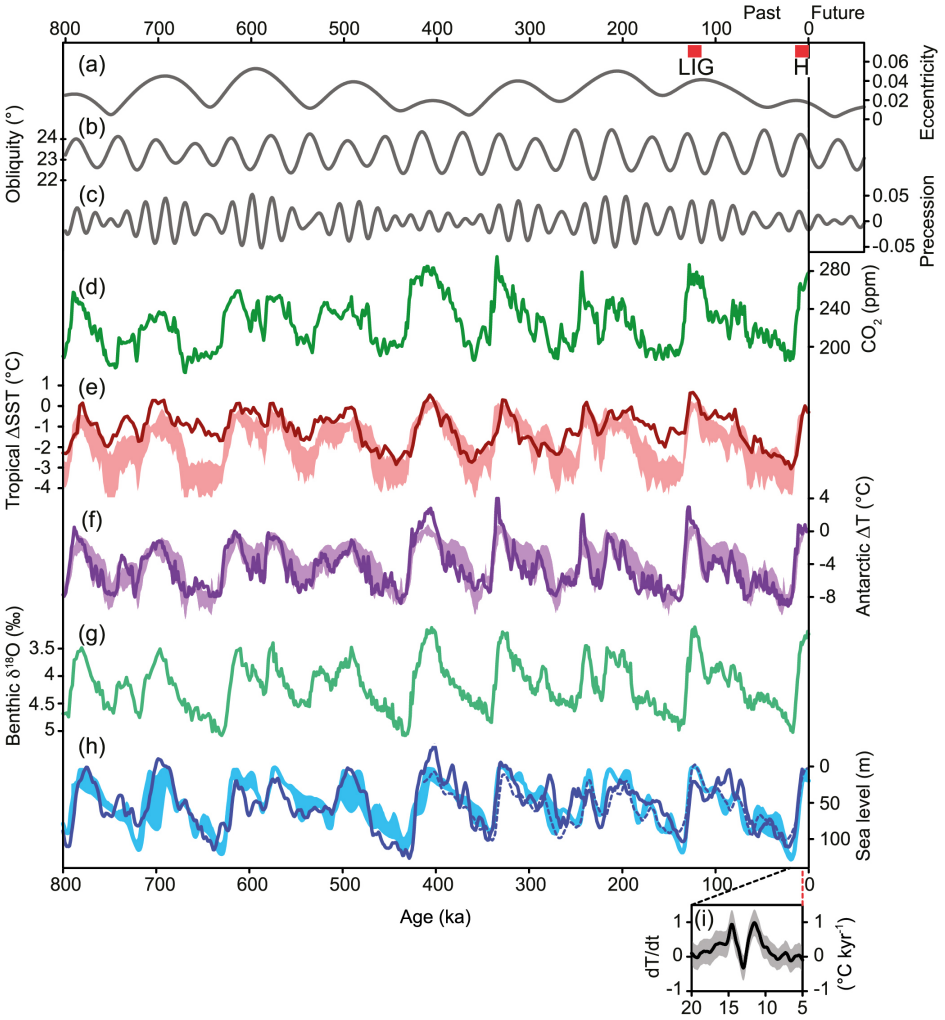

FIGURE 2.4: Time series of several climate forcings and temperature indices over the past 800,000 years from the 5th IPCC assessment report. a), b), and c) show the orbital parameters eccentricity, obliquity, and precession, respectively; d) shows atmospheric CO_2 concentration; e) and f) are reconstructions of tropical sea surface temperatures and Antarctic temperatures derived from several ice cores; benthic $\delta^{18}O$ reflects a proxy for global ice volume and deep-ocean temperature (g) and is therefore linked to global sea level (h). Solid lines represent orbital forcing and proxy records, respectively, while shaded areas are representative of climate model simulations. Marked is also the Last Interglacial (LIG). [Figure taken from Stocker (2014)]

3. The coupled climate-ice sheet model

In the following, the model used in this study is presented. As different versions of this model were used, all submodels and the coupling between submodels are explained in the following. A description of the specific model version and included submodels is given in the corresponding chapters (Chapters 4, 5, and 6)

The model used in this study is the AWI Earth System Model (AWI-ESM), which includes the AWI Climate Model (AWI-CM) that has been widely used for past, present, and future climate simulations, and participated in the sixth phase of the Coupled Model Intercomparison Project (CMIP6) (Semmler et al., 2020; Sidorenko et al., 2019; Sidorenko et al., 2015; Rackow et al., 2018; Shi and Lohmann, 2016). Besides representations of the atmosphere and the ocean, the model allows for dynamic vegetation and for interactive cryosphere components, like ice sheets and icebergs. Within the scope of this work, three different versions of AWI-ESM have been employed.

A simplified overview of the model is given in Fig. 3.1. In the following, the different model components are explained in more detail.

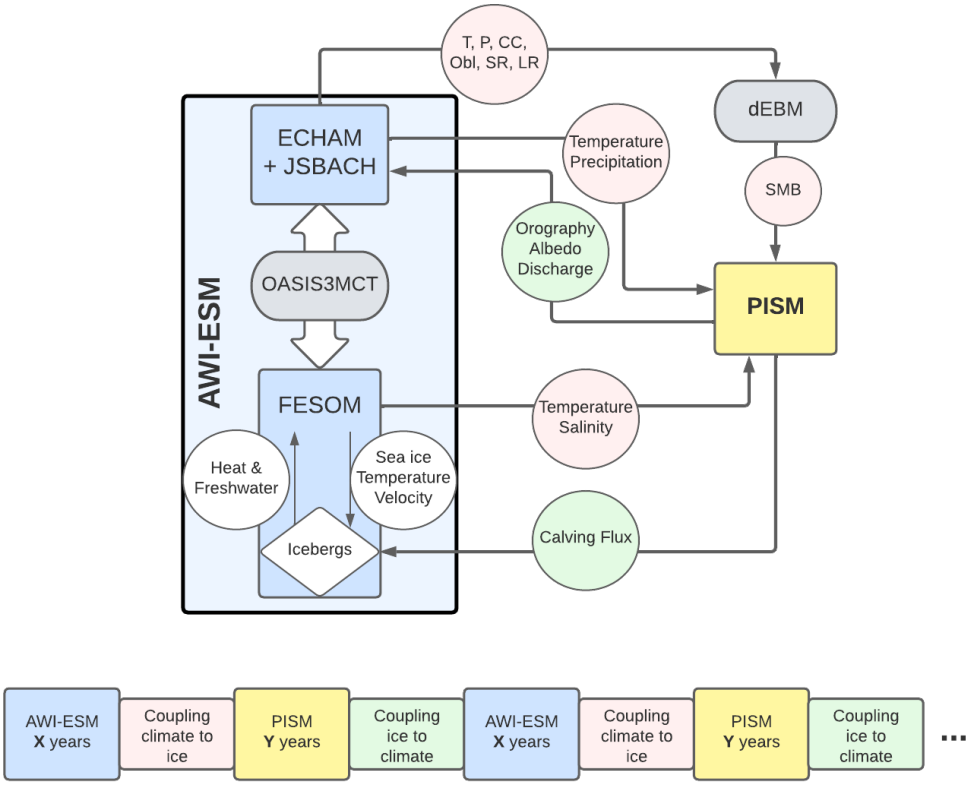

FIGURE 3.1: Top: Schematic of AWI-ESM (light blue) including the atmosphere model ECHAM6, the ocean-sea ice model FESOM with the optional iceberg submodel (white), the ice sheet model PISM (yellow), and several fields exchanged between the different climate and cryosphere components (light red for coupling from AWI-ESM to PISM and light green for coupling from PISM to AWI-CM). The coupling from ECHAM to the diurnal Energy Balance Model (dEBM) (Krebs-Kanzow et al., 2021) includes temperature (T), precipitation (P), obliquity (Obl), shortwave radiation (SW), and longwave radiation (LR). dEBM provides the surface mass balance (SMB) as output. Bottom: The asynchronous coupling procedure, in which AWI-ESM and PISM are run consecutively in so-called chunks for X and Y model years, respectively. Y does not need to equal X. The coupling is done between two chunks.

3.1 The atmosphere model ECHAM

ECHAM6 is an atmospheric general circulation model in its sixth version. Originally developed at the European Center for Medium-Range Weather Forecasts (ECMWF), it has been branched off and further developed at the Max Planck Institute for Meteorology (MPI-M) in Hamburg (Stevens et al., 2013). The name ECHAM stems from **EC**MWF and **Ham**burg. It consists of an adiabatic core that is based on the vorticity and divergence form of the primitive equations. Temperature and surface pressure are the thermodynamical coordinates. The model also includes a set of physical parameterizations to represent diabatic processes on a sub-grid scale. Furthermore, the land-surface model JSBACH is incorporated within ECHAM (Reick et al., 2013). It enables to account of surface processes like heat and water storage, dynamical vegetation, and changes in surface albedo. A hydrology model accounts for river discharge (Hagemann and Dümenil, 1997). The setup applied in this study is T63L47, which represents a horizontal resolution of approximately 1.9° and resolves the atmosphere vertically up to 0.01 hPa with 47 vertical levels.

3.2 The ocean-sea ice model FESOM

The Finite-VolumE sea ice-Ocean Model (FESOM2) is developed at the Alfred Wegener Institute (Danilov et al., 2017; Koldunov et al., 2019; Scholz et al., 2019; Scholz et al., 2022). It employs unstructured grids, which allow for spatially varying horizontal resolutions. Dynamically active regions, e.g., the North Atlantic, the equator, and coastal areas, can be modeled with a relatively high resolution while keeping the total amount of grid cells relatively small (Fig. 3.2). Unlike its predecessor, FESOM1.4 (Wang et al., 2014), FESOM2 is a finite-volume model. This enables storing three-dimensional variables in two-dimensional fields (one for the depth coordinate and one for the horizontal vertices). This gives a huge speed-up compared to the finite-element implementation of FESOM1.4, where all fields were stored in one-dimensional arrays. Performance-wise, this brings FESOM2 close to ocean models using structured grids (Danilov et al., 2017). It also enables z^* coordinates, allowing for variable layer thicknesses and a freely evolving surface.

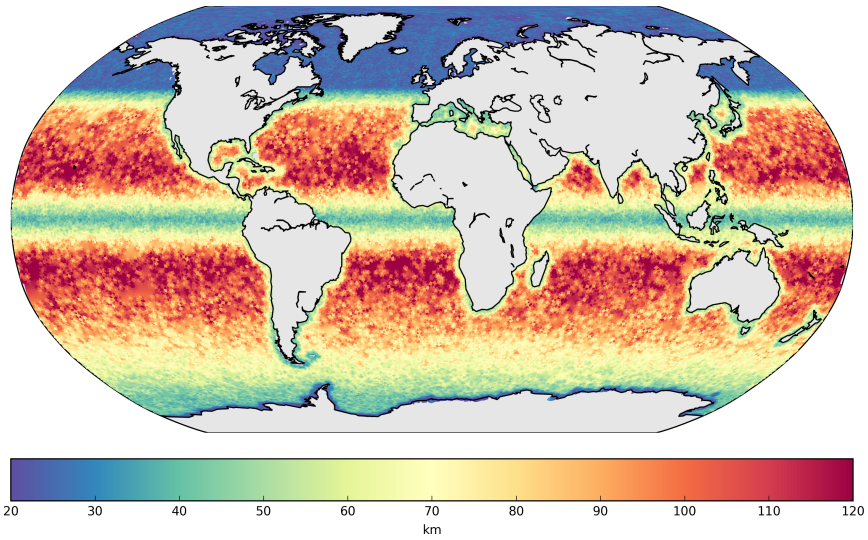

FIGURE 3.2: The horizontal resolution of the FESOM mesh used in this study (COREII). The triangular grid shows a higher resolution at the coasts, along the equator, and in the polar regions of up to 20 km while having a coarser resolution in the open ocean of up to 120 km. The resolution is defined as the square root of the area of the scalar control volume (Danilov et al., 2017). [Figure taken from FESOM (2023)]

3.2.1 Dynamics

The model solves the hydrostatic primitive equations with Boussinesq and traditional approximations. These include a hydrostatic approximation for the vertical component of the Navier-Stokes equations:

$$\partial_z p = -g\rho \tag{3.1}$$

The horizontal Navier-Stokes equation gives the momentum equation in the horizontal plane:

$$\partial_t \mathbf{u} = -f\mathbf{e}_z \times \mathbf{u} - (\mathbf{u} \cdot \nabla_h + w\partial_z)\mathbf{u} - \nabla_h \frac{p}{\rho_0} + D_h\mathbf{u} + \partial_z \nu_v \partial_z \mathbf{u} \tag{3.2}$$

Here, $\mathbf{u}$ is the horizontal velocity vector, f the Coriolis parameter, $\mathbf{e}_z$ the unit vector vertical to the horizontal plane, ρ_0 the reference density, p the pressure, D_h a horizontal viscosity operator and ν_v the vertical viscosity. The first term on the right-hand side expresses the inertial force due to the rotating frame of reference. The second term is the advective transport of momentum. The third term arises from the pressure gradient force. The last two terms introduce

frictional forces related to horizontal and vertical variations in the velocity field. With the Boussinesq approximation, variations in density are only considered in the gravitational term. Therefore, the flow is non-divergent, and the continuity equation simplifies to:

$$\partial_z w = -\nabla_h \cdot \mathbf{u} \tag{3.3}$$

3.2.2 Thermodynamics

The equations mentioned above are complemented by an equation of state, giving a functional relationship between density, pressure, temperature, and salinity. With the Boussinesq approximation, the pressure can be expressed as a linear function of ocean depth z, and the equation of state can be formulated as:

$$\rho = \rho(T, S, z) \tag{3.4}$$

This equation is solved following the EOS-80 seawater equations. Therefore, the potential temperature is used to estimate density. The advection of a tracer C is given by:

$$\partial_t C + \nabla_h \cdot (\mathbf{u}C) + \partial_z(wC) = \nabla \cdot \mathbf{K}\nabla C \tag{3.5}$$

Here, C can be temperature (T) or salinity (S), $\mathbf{K}$ is a diffusion tensor to parameterize mixing via sub-grid scale eddies. One common paraterization is the Gent-McWilliams (GM) parameterization after Gent and McWilliams (1990). In FESOM1.4 this parametrization is implemented according to Griffies (1998) and Griffies et al. (1998), where tracer mixing due to isoneutral diffusion (Redi, 1982) and adiabatic stirring (Gent and McWilliams, 1990) are combined to a skew flux. In FESOM2 however, GM is implemented following the algorithm by Ferrari et al. (2010) that provides an explicit eddy-induced streamfunction (Danilov et al., 2017).

3.2.3 Discretization and layer thickness

The Arbitrary Lagrangian-Eulerian (ALE) vertical coordinate framework is used in FESOM2. It allows level surfaces to move and is a hybrid approach of the two limiting cases with fixed *z-levels* and isopycnal surface levels. However, only slight deviations from *z-levels* are allowed at the moment. Each layer is formed by prisms prescribed by the surface mesh. The inter-layer communication takes place via the transport velocity w_{kv}. It is located on vertex v and

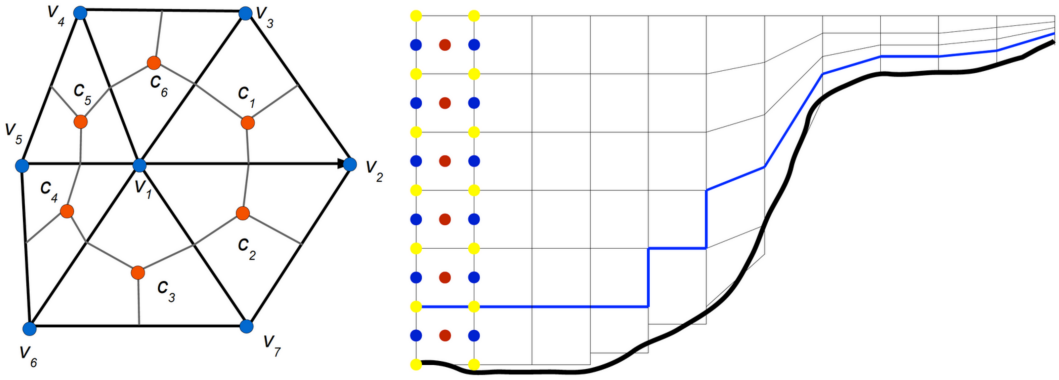

FIGURE 3.3: Schematic of cell-vertex discretization (left) and the vertical discretization (right). The horizontal velocities are located at cell centers (red circles), and scalar quantities are located at vertices (blue circles). Both horizontal velocities and scalar quantities are located at mid-depth, while the vertical velocity is located at vertices but at layer boundaries (yellow circle). Scalar control volumes are obtained by connecting the cell centers with the midpoints of the edges (left). The bottom cells can be full cells or partial cells, and mesh levels can be terrain-following (right). [Figure taken from (Danilov et al., 2017)]

layer-interface k (yellow dots in Fig. 3.3). The vertical transport velocity is defined as the difference between the physical velocity normal to the surface layer and the velocity of the layer interface itself. All other quantities are defined at mid-layers (Danilov et al., 2017). Scalar quantities are defined on cell vertices, whereas horizontal velocities are defined on the vertical prism faces.

The discretized continuity equation becomes an equation of layer thickness. Integrating it over all layers k gives the equation of elevation:

$$\partial_t \eta + \nabla_h \cdot \sum_k h_k \mathbf{u}_k + W = 0 \tag{3.6}$$

With the surface elevation η, the layer thickness h, the horizontal velocity $\mathbf{u}$ and the water flux at the ocean surface W.

3.2.4 Iceberg module

The iceberg component is a submodel of FESOM, and a detailed description can be found in Rackow (2011) and Rackow et al. (2017).

Studies using the interactive iceberg component were ocean-only simulations, in which the icebergs were treated as passive tracers that allowed diagnosing

a meltwater field (Rackow et al., 2017), but lacking freshwater and heat feedback to the ocean model. This work introduces the iceberg module as a fully coupled component within FESOM. Hence, freshwater and heat fluxes are bi-directionally coupled between icebergs and the ocean. Initial iceberg positions and dimensions are obtained via fields of calving discharge from the ice sheet.

In the following, a overview is given for the model as applied in Rackow et al. (2017). New model development, which has been implemented within the scope of this thesis, is explicitly mentioned.

The model is a Lagrangian iceberg model, i.e., all icebergs are represented by point particles. While these particles are zero-dimensional, each has a length, width, and height assigned to it. These physical quantities are altered during the simulation by thermodynamical processes. For reasons of simplification, each iceberg is assumed to have a quadratic base area, i. e. the width is equal to the length and to be of cuboidal shape.

The momentum equation of an iceberg is given by:

$$M\frac{d\mathbf{u}}{dt} = \mathbf{F}_c + \mathbf{F}_{sl} + \mathbf{F}_a + \mathbf{F}_o + \mathbf{F}_i \tag{3.7}$$

where $\mathbf{F}_c = -Mf \times \mathbf{u}$ is the Coriolis force (on the mass M), $\mathbf{F}_{sl} = -Mg\Delta\eta$ is the gravitational force along the surface slope $\Delta\eta$, and the remaining three terms are drag forces for the atmosphere, ocean, and sea ice of the general form:

$$\mathbf{F}_x = C_x|\mathbf{u}_x - \mathbf{u}|(\mathbf{u}_x - \mathbf{u}) \tag{3.8}$$

with x being o for the ocean drag, a for the atmosphere drag, and i for the sea ice drag. The ocean and the atmosphere drag forces act on the submerged sidewall and those above sea level, respectively. Ocean velocities are averaged over the depth of an iceberg. For sea ice, three cases are considered:

- Sea ice concentration is less than 15% and does not affect icebergs at all.
- Sea ice concentration is above 15% but below a critical threshold. Here, sea ice drag linearly increases with sea ice thickness.
- Sea ice concentration and strength exceed critical values, and icebergs are considered to be trapped in sea ice. Then iceberg velocities are set equal

to the sea ice velocity.

Interactions between icebergs are not modeled. However, a very simplified parametrization is used within the scope of this work to avoid the overloading of ocean cells: if an iceberg is about to change from one grid element to another, the total iceberg area contained in this grid element is calculated. If the new iceberg leads to a larger total iceberg area than the actual element area, it does not move but stays in its previous grid element.

Thermodynamics takes into account the erosion by surface waves, buoyant convection, and basal and lateral basal melting (Rackow et al., 2017), following work by Bigg et al. (1997), Gladstone et al. (2001), Jongma et al. (2009) and Martin and Adcroft (2010). The total mass balance for an iceberg is given by:

$$\rho \frac{dV}{dt} = -\rho(A_b M_b + A_{bv} M_{bv} + A_v M_v + A_e M_e) \tag{3.9}$$

where A and M are the faces on which melting occurs and the melt flux, respectively. The indices stand for bottom melting (b), melting at the submerged sides (bv), buoyant convection along the sides (v), and erosion on the sides (e). Erosion follows an empirical formula developed and further improved by Bigg et al. (1997), Gladstone et al. (2001), and Martin and Adcroft (2010). It acts on two side walls $A_e = 2LH$ and takes into account relative velocity between winds and the ocean, sea surface temperature, and the sea ice cover. Sea ice cover above 40% increasingly dampens wave erosion until it fully prevents wave erosion when a sea ice cover of 100% is reached. Buoyant convection also follows an empirical formula, dependent on a thermal driving temperature T_d, which is defined as the difference between ambient water temperature and the freezing point temperature (T_f) (Neshyba and Josberger, 1980). In contrast to other studies, which often implicitly assume $T_f = 0$, the model used in Rackow et al. (2017) follows more strictly the original work by Neshyba and Josberger (1980) and uses $T_d = \max(0, T_m - T_f)$, with T_f being the in situ freezing temperature at mid-depth and T_m being the average water temperature along the iceberg draft.

For the basal melting (b) and the melting along submerged sides (bv), the formulation for basal ice-shelf melting, introduced by Hellmer and Olbers (1989) and Holland and Jenkins (1999) is used (Rackow et al., 2017). The melt rate at the interface between iceberg and ocean is calculated by solving a system of equations, given far-field temperates and salinities. These equations are:

- the freezing point dependent on salinity and pressure:

$$T_B = a \cdot S_B + b + c \cdot p_B \tag{3.10}$$

  with S_B and p_B being the salinity and pressure, respectively, at the interface and the empirical constants a, b, and c.

- the energy conservation:

$$Q_I^T - Q_M^T = Q_{latent}^T \tag{3.11}$$

  with Q_I^T and Q_M^T being the conductive heat flux through the ice shelf and the diffusive heat transport in the boundary layer, balanced by the latent heat flux at the ice-ocean interface (Q_{latent}^T). The right-hand side is negative for ice melt and positive for ice freezing.

- the analogous salt conservation:

$$Q_{brine}^S = \rho_M \; w_B \; (S_I - S_B) \tag{3.12}$$

  with S_I and S_B being the bulk salinity of the ice shelf and the salinity of the boundary layer, respectively. Q_{brine}^S is the salt flux at the interface.

This approach also enables freezing, i.e., the growth of an iceberg at the bottom. To prevent unphysical growth at the base of grounded icebergs, negative melt rates are set to zero if an iceberg is grounded in the model version used here.

In order to speed up the iceberg module, different measures have been newly implemented into the model: the first of these is the implementation of a scaling approach, similar to Martin and Adcroft (2010). This approach reduces the number of simulated icebergs by dividing the icebergs into different size classes. For each class, a scaling factor is defined by which the number of simulated icebergs is reduced. Each simulated iceberg then represents multiple other icebergs. The calculated freshwater and heat fluxes are multiplied by the scaling factor to ensure mass and energy conservation. A second approach for speeding up the iceberg module is a variable coupling frequency between ocean and iceberg components. So far, the coupling and hence the simulation of icebergs took place every FESOM ocean time step. Due to the relatively slow movements of the icebergs, a coupling three or four times a simulated day seems to be sufficient.

As mentioned above, this work introduces the iceberg module as a fully coupled

component within FESOM. Freshwater and heat fluxes are added to the respective FESOM internal sea-ice fluxes. Hence, the iceberg feedback is applied to the ocean surface. Furthermore, it is distributed to all nodes that constitute the containing element. The freshwater fluxes from iceberg melting are not considered part of the Antarctic surface runoff anymore, i.e., the influx is allowed to occur on the open ocean instead of directly along the coast and shelf regions. However, the total salinity is balanced, so the iceberg setup has no net freshwater flux. This is done to account for discrepancies between the constant reduction of surface runoff and the variable freshwater flux from iceberg melting. In a coupled climate-ice sheet setup, the surface runoff would be reduced accordingly, so there would be no need for a salinity balancing. While the total salinity is balanced, oceans' total internal energy is not, and there is a negative net heat flux due to iceberg melting.

3.3 The parallel ice sheet model PISM

The Parallel Ice Sheet Model (PISM) (Bueler and Brown, 2009; Winkelmann et al., 2011) is a three-dimensional finite-difference model with thermodynamical coupling. Instead of solving the full-Stokes equations, it combines two approximations: the Shallow Ice Approximation (SIA) describes ice flow by vertical shear stress on a non-sliding base. This approximation is reasonable for most areas of land-ice sheets. However, for ice shelves and fast-flowing outlet glaciers and ice streams, this approximation cannot be used confidently anymore. Here, the Shallow Shelf Approximation (SSA) is used additionally. Besides its application for ice flow within ice shelves, it acts as a sliding law for sliding land ice. While the SSA and the SIA are dominant for grounded ice and ice shelves, respectively, a combination of both approximations is used for ice streams and basal sliding (Bueler and Brown, 2009; Winkelmann et al., 2011). A power law is used to account for the basal strength of the till beneath the ice sheet and allow for sliding of the ice sheets base next to plastic deformation (Bueler and Brown, 2009; Clarke, 2005):

$$\boldsymbol{\tau}_b = -\tau_c \frac{\mathbf{u}}{u_{threshold}^q |\mathbf{u}|^{1-q}} \tag{3.13}$$

$\boldsymbol{\tau}_b$ is the shear stress, τ_c is the yield stress representing the basal strength, $\mathbf{u}$ is the sliding velocity, and $u_{threshold}$ is a threshold velocity for when sliding occurs. The yield stress is determined by the Mohr-Coulomb law (Cuffey and Paterson, 2010):

$$\tau_c = c_0 + \tan(\Phi) N_{till} \tag{3.14}$$

where c_0 is the till cohesion (set to zero by default in PISM), Φ is the till friction angle, and N_{till} is the effective pressure of the till, dependent on the till-pore water amount, which is determined by a sub-glacial hydrology model.

3.3.1 Calving

Several calving laws are implemented within PISM. The eigen-calving is a physically-based calving parameterization. Here, the calving rate (c) is proportional to the spreading rates in both eigendirections of the flow ($\epsilon_+ \dot{\epsilon}_-$), i.e., the directions along and perpendicular to the flow field:

$$c = K \dot{\epsilon}_+ \dot{\epsilon}_- \tag{3.15}$$

Here, K is a constant representing the material properties of the frontal ice. The calving rates depend on the geometry and the boundary conditions along the ice shelf margin. While this parametrization cannot resolve single calving events, it gives reasonable calving fronts which agree well with observations of large Antarctic ice shelves. However, it is not well suited for narrow fjords (Levermann et al., 2012).

A simpler calving parametrization is thickness-calving, based on the observation of calving fronts being commonly thicker than 150-250 m. Any shelf ice undercutting this threshold calves off, however, with a maximum rate of one grid cell per timestep.

3.3.2 Surface mass balance

The surface mass balance can either be prescribed or internally calculated by the Positive Degree-Day (PDD) method (Reeh, 1991). It is an efficient method widely used for paleoclimate simulation (e.g. Charbit et al. (2002), Charbit et al. (2008), Tarasov and Peltier (2004), Niu et al. (2019b), and Niu et al. (2019a)). This semi-empirical method assumes a proportional relationship between the melt rates of ice and snow and the sum of days with positive surface air temperature over the year. Following Calov and Greve (2005), this PDD value is calculated by:

$$PDD = \int_0^A dt \left[\frac{\sigma}{\sqrt{2\pi}} \exp\left(-\frac{T_{mon}^2}{2\sigma^2} \right) + \frac{T_{mon}}{2} \mathrm{erfc}\left(-\frac{T_{mon}}{\sqrt{2}\sigma} \right) \right] \tag{3.16}$$

It requires only monthly surface temperature (T_{mon}) and precipitation fields as inputs. For temperatures below 0°C, precipitation is considered as snow, and for temperatures above 2°C, precipitation is considered as rain; for temperatures in between, the percentage of snow and rain is linearly interpolated. To account for daily variability, white noise is added to the monthly mean temperature. The standard deviation σ is 5 K.

Alternatively, the surface mass balance can be calculated externally by an energy balance model and prescribed to PISM. A model to fulfill this intermediate step is the diurnal Energy Balance Model (dEBM) (Krebs-Kanzow et al., 2021), which accounts for short and longwave radiation, cloud cover, obliquity, surface temperature, and precipitation. The surface mass balance (SMB) and the ice sheet's meltwater runoff (RO) are given as follows:

$$SMB = SF - ME + RZ \tag{3.17}$$

$$RO = ME + RF - RZ \tag{3.18}$$

Here, the snowfall (SF) and rainfall (RF) are functions of cloud cover and near-surface air temperature. Surface melting (ME) is only possible if near-surface temperatures exceed −6.5°C and depends, like the refreezing (RZ), on the surface energy balance, that takes into account incoming shortwave and outgoing longwave radiation as well as surface dependent albedo values.

3.3.3 Ice shelf dynamics

The PISM internal ocean model components provide sub-shelf temperature and sub-shelf mass flux to the ice dynamics core. Several options exist as to how PISM internally computes these necessary fields. Two of these are used within the scope of this work. The first one derives the abovementioned fields from the thermodynamics in the boundary layer between the ice shelf and the ocean by using the same set of equations mentioned in chapter 3.2.4. The two-dimensional fields for ocean temperature and salinity need to be provided, and equations 3.10, 3.11, and 3.12 are applied.

The other option is the Potsdam Ice-shelf Cavity mOdel (PICO) (Reese et al., 2018) that is based on the box model of Olbers and Hellmer (2010). It

parameterizes sub-shelf overturning and vertical mixing. This overturning is driven by melting at the ice shelf. Less dense freshwater rises along the base of the ice shelf. This water flow is balanced by a lateral flow of dense water at depth. By the implementation of consecutive boxes that follow the flow, this overturning mechanism is captured within the model. The boxes adjust to moving grounding lines. Besides input fields for temperature and salinity, basin masks need to be provided to the model (Fig. 3.4). These basins shall reflect regions with similar, large-scale ocean conditions. A detailed description is given in Reese et al. (2018).

3.4 Climate - ice sheet coupling

The coupling between AWI-ESM and Parallel Ice Sheet Model (PISM) is done iteratively. Each model runs for a certain amount of consecutive years, called a chunk. At the end of each chunk, a coupling procedure starts, processing all relevant fields and regridding them. Then the next model's chunk starts. In the case of the AWI-ESM - PISM coupling, AWI-ESM always runs first, followed by PISM. Both models can be run asynchronously in an accelerated manner, i.e., with different chunk lengths. This allows for the simulation of many ice sheet years while keeping the computational costs of the climate model relatively low. In this case, energy and freshwater volume are not conserved, but fluxes are. The coupled model setup has been used for paleoclimate studies in Niu et al. (2021). Figure 3.1 illustrates which fields are coupled between the two models.

3.4.1 Atmosphere - ice sheet coupling

The fields that need to be provided for the coupling from the atmosphere to the ice sheet depend on the surface mass balance scheme used. For the PDD scheme, these are only two-meter temperatures and precipitation. For dEBM, additionally included are cloud cover, obliquity, and short and long-wave radiation (Krebs-Kanzow et al., 2021). As the ice sheet domain has a higher resolution than the ECHAM grid, bilinear interpolation is used to downscale atmospheric quantities. At this step, a lapse rate correction of 0.05 K m^{-1} is applied. Changes in orography, vegetation, and albedo are coupled back from PISM to ECHAM. Freshwater fluxes via surface runoff, calving, and basal melting are fed into the ECHAM internal river routing scheme and considered as freshwater discharge. Hence, they enter the ocean at the surface in coastal regions as liquid water, regardless of the ice sheet's internal process, the fluxes

originate from. This methodology neglects the coupling of latent heat fluxes linked to ice melting and the potential transport of freshwater as ice via icebergs.

3.4.2 Ocean - ice sheet coupling

For the coupling from FESOM to PISM, there are two options. One is the prescription of two-dimensional temperature and salinity fields. These fields are averaged over the upper 450 m and over all model years covered by the respective chunk. The other option is the usage of the PISM submodel PICO that parameterizes sub-shelf circulation in pre-defined ocean basins. In setups without large ice shelves, the first coupling approach is sufficient. The coupling of freshwater discharge from PISM is done via the land-surface hydrology model. Other feedbacks to the ocean, like changes in grounding line position, are not implemented yet. However, within the scope of this work, a coupling routine has been implemented to derive discrete icebergs, as lagrangian point particles, from the continuous calving flux provided by PISM. These icebergs can be prescribed to the iceberg extended FESOM version with dimensions and an initial position assigned to each of them.

3.5 Iceberg seeding

Iceberg dynamics and thermodynamics are calculated in a Lagrangian framework, i.e., each iceberg is treated as a point particle. This implies that the initial conditions of each iceberg need to be provided, including the location, velocity, dimensions, and scaling factors. Apart from the velocities, which are set to zero initially, all other parameters are deduced from ice sheet model output. The model output provides a continuous calving field. To generate discrete icebergs from the continuous field, this calving flux is integrated over each basin (Fig. 3.4) to get the total amount of ice discharge. In the next step, this amount is divided by a reference iceberg height to get a total calving area, and the number of icebergs is deduced by division with a reference iceberg area. Initialized icebergs follow a prescribed size distribution. For Antarctica, this is a power law with a slope of -1.52, following observations by Tournadre et al. (2016). However, different size distributions can be applied to certain basins. The Potsdam Ice-shelf Cavity mOdel (PICO) basins are chosen as an integration area to capture some heterogeneity in spatial iceberg discharge but to have a sufficiently large area to allow for the calving of giant icebergs. Furthermore,

it makes the actual size distribution independent of model resolution. Icebergs are assumed to have a quadratic surface. The iceberg height is set to be equal to the length and width, respectively, but not larger than 250 m. In an iterative process, the dimensions are adjusted so that the total iceberg volume matches the integrated discharge. Similar to Martin and Adcroft (2010), scaling factors are applied to reduce the overall computation time. These factors are prescribed for different size classes. For each size class, a specific scaling value is set by which the amount of icebergs in this size class is reduced. The heat and freshwater fluxes released by this iceberg are then scaled up again accordingly. The icebergs are seeded into the nearest ocean grid cells along the coastline. These steps are done for each basin individually to ensure a consistent distribution along the coastline.

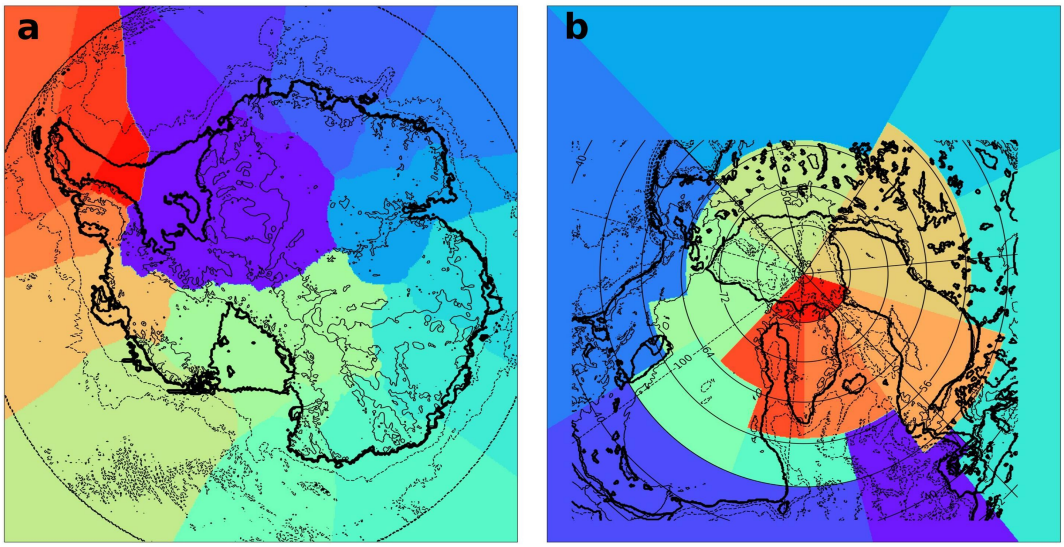

FIGURE 3.4: PICO basins for the Northern Hemisphere and Antarctica. The discharge flux is integrated over each basin and icebergs are seeded according to it.

4. Effect of an interactive ice sheet on Greenland's freshwater discharge in future scenarios

Future melting of the GIS might lead to the release of huge amounts of fresh water into the northern North Atlantic. These freshwater perturbations may affect deep water formation and the AMOC, a crucial component in Earth's climate system. Paleoclimate studies have found that its strength can be linked to abrupt climate changes in the past (Broecker et al., 1985; Keigwin et al., 1991). Examples of these changes are the so-called "Little Ice Age" (Bianchi and McCave, 1999; Broecker, 2000; Thibodeau et al., 2018) or the Last Termination and Heinrich Events (Barker et al., 2009; Barker et al., 2010; Knorr and Lohmann, 2007). With respect to global warming, several studies suggest a future slowdown (Gierz et al., 2015; Golledge et al., 2019; Stocker and Schmittner, 1997; Swingedouw and Braconnot, 2007; Weaver et al., 2012), and observations of SST, that can be used as a proxy for AMOC strength, already indicate a recent slowdown since the mid-twentieth century (Dima and Lohmann, 2010). However, the extent of the future weakening and the parts of different mechanisms affecting the AMOC are still unclear. One of these mechanisms is the potential future melting of the GIS. Studies by Latif et al. (2000) and Lohmann (2003) suggest a strong atmospheric freshwater export from the Atlantic as an AMOC stabilizing effect in warm climates and those with a weak AMOC, respectively.

Studies for phase five of the Climate Model Intercomparison Project (CMIP5) suggest a further future weakening of the AMOC for different IPCC scenarios. Weaver et al. (2012) analyzed 30 of these models and found an AMOC weakening of 23–30% for the Representative Concentration Pathway (RCP) scenario RCP4.5 and a weakening of 36–44% for the RCP8.5 scenario. While most CMIP5 models deploy land surface and hydraulic models and capture, for example, surface runoff and snow accumulation, they generally do not include

explicit Ice Sheet Models (ISM). Therefore, they lack important feedbacks, such as melt elevation feedbacks and inherent fluxes from ice through calving and basal melting. To compensate for these drawbacks, some studies use ad hoc water hosing without explicitly simulating the location of freshwater release (Hu et al., 2009; Hu et al., 2011; Jungclaus et al., 2006; Stammer et al., 2011).

Studies with coupled climate ice sheet models have been performed (Driesschaert et al., 2007; Gierz et al., 2015; Golledge et al., 2019; Lenaerts et al., 2015; Mikolajewicz et al., 2007) but with limitations regarding the resolution, the coupling, or the forcing applied. It has been suggested that the location of freshwater inflow is essential to accurately assess the effect of ice sheet melting on the AMOC (Liu et al., 2018). While freshwater fluxes from the GIS can affect deep water formation in the Labrador Sea (Yang et al., 2016) and AMOC (Weijer et al., 2012), other studies show only weak interactions between west of Greenland, the Labrador Current, and the Labrador Sea (Eden and Böning, 2002; Schmidt and Send, 2007; Wang et al., 2018). Böning et al. (2016) suggest that only small amounts of GIS meltwater reach the Labrador Sea with little effect on the AMOC. Danek et al. (2019) find that the resolution in the ocean circulation model matters for the Labrador Sea convection and that such areas can play an important role in realistically simulating the variability in AMOC. Additionally, the melting of ice sheets and the melting of sea ice might play a crucial role in a possible future AMOC slowdown (Liu et al., 2019).

Here, the aim of this study is to improve the understanding of the effects of GIS melting on the AMOC by identifying the main contributors to a possible future AMOC slowdown and addressing different feedback mechanisms. For that, a multiresolution atmosphere-ocean-ice sheet model with increased resolution in the northern North Atlantic is used to run different future scenarios.

4.1 Model setup for the warming case

Transient simulations are performed for the interval from 1850 to 2200 with AWI-ESM with and without the interactive ice sheet component. Control simulations are run for both model setups (CTRL, CTRL-ice). For those runs, greenhouse gas (GHG) forcing is fixed at an assumed pre-industrial level (Fig. 4.1a). Historical runs are performed, starting from the year 1850 (HIST, HIST-ice), that are forced with historical GHG concentrations, reconstructed from observations. Two different future scenarios, following the Representative Concentration Pathway (RCP), are investigated. These are the RCP4.5 (Clarke, 2007;

Wise et al., 2009) and the RCP8.5 (Riahi et al., 2007) scenarios, corresponding to atmospheric CO_2eq concentrations by the year 2100 of 581 and 1,231 ppm, respectively. These CO_2 concentrations represent a combined equivalent of all projected anthropogenic forcing, including land-use change and aerosol emissions. To be able to investigate the effects of global warming on the ice sheet, the simulations are prolonged to the year 2200, fixing the CO_2eq concentrations of the year 2100. Each scenario is simulated with (RCP4.5-ice, RCP8.5-ice) and without interactive GIS (RCP4.5, RCP8.5). The ice sheet domain covers the Greenland Ice Sheet with a horizontal resolution of 5 km. The COREII grid is used for the ocean, and the atmosphere is run with the T63L47 setup. The coupling between the climate and ice sheet components is done synchronously, i.e. no acceleration factor is applied, and takes place every three model years. The PDD scheme is used to calculate the ice sheets' surface mass balance. Temperature and precipitation fields are downscaled via bilinear interpolation.

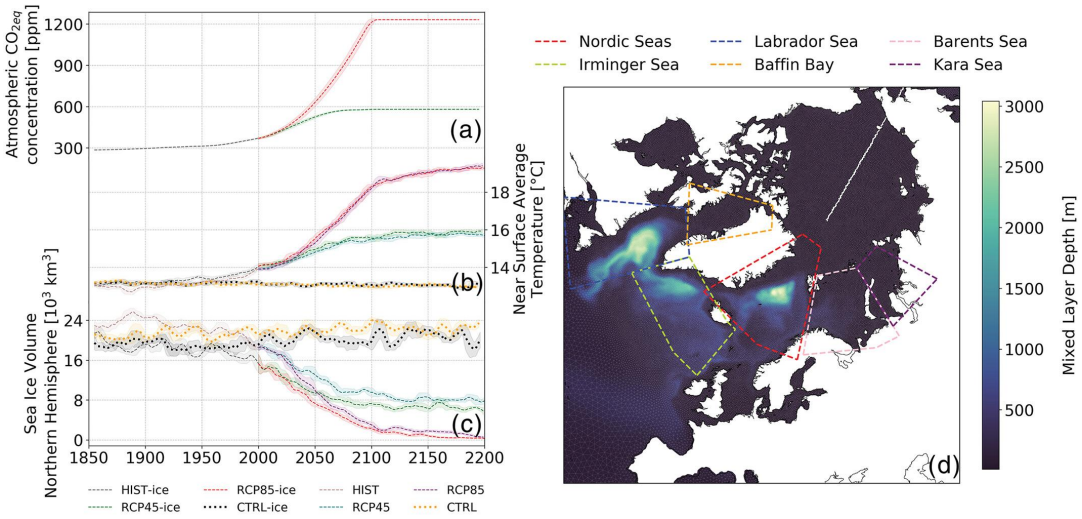

FIGURE 4.1: Time series of 11-year mean (a) CO_2 forcing as concentration of CO_2 equivalent in the atmosphere, (b) global near-surface average temperature, (c) sea ice volume in the Northern Hemisphere; shaded areas indicate one standard deviation; (d) North Atlantic mixed layer depth with Barents Sea, Baffin Bay, Kara Sea, Labrador Sea, Nordic Seas, Irminger Sea.

4.2 Climatic response to greenhouse gas forcing

The global surface average temperature increases from around 13°C to above 16°C in the RCP4.5 scenario and about 19.5°C in the RCP8.5 scenario (Fig. 4.1b). Around the year 2150, most of the sea ice in the Northern Hemisphere is gone in the RCP8.5 scenario and decreased to less than a half in the RCP4.5 scenario (Fig. 4.1c). There are no significant differences between the results, including the ice sheet and without.

Looking at changes in precipitation (P) and evaporation (E), a strong decrease in $P - E$ occurs over the Atlantic between 10°N and 40°N as well as 10°S and 4°S, reaching values of up to -1 m year^{-1} in the RCP8.5 scenario (Fig. 4.2). An increase in $P - E$ can be seen over Greenland and North Europe and also over the Labrador Sea and the Irminger Sea. This pattern is more distinctive in the RCP8.5 scenario, and the differences between the two model results are relatively weak. The pattern of $P-E < 0$ for the low latitudes and $P-E > 0$ for the high latitudes gets enhanced in both future scenarios, whereas no significant differences between the two model results can be seen.

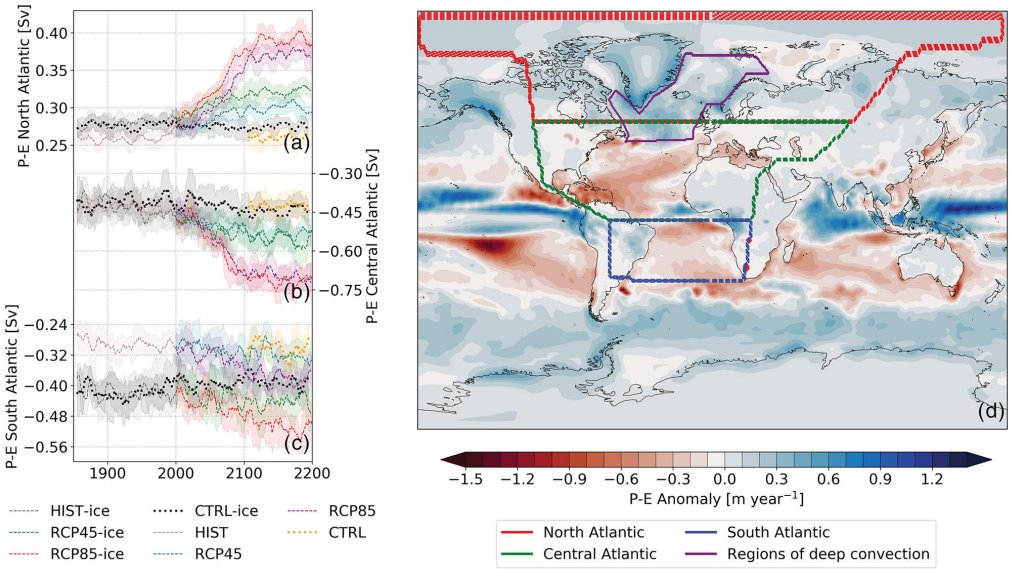

FIGURE 4.2: Time series of 11-year mean $P - E$ integrated over the catchment areas of (a) North Atlantic, (b) Central Atlantic, (c) South Atlantic for all scenarios; shaded areas indicate one standard deviation; for CTRL only the last 100 years are shown; (d) $P - E$ anomaly averaged for the years 2170-2199 for RCP8.5-ice with different areas of the Atlantic.

The AMOC, defined here as the maximum of the meridional streamfunction between a depth of 200 and 2,000 m and $30 - 60$°N, shows a slowdown in all experiments. The AMOC index in the coupled model simulations is around

1 Sv higher than in the uncoupled model runs (Fig. 4.3a). The minimum AMOC index is reached around the year 2075 for the RCP4.5 scenario and around the year 2110 for the RCP8.5 scenario. Afterward, the AMOC recovers again in all simulations.

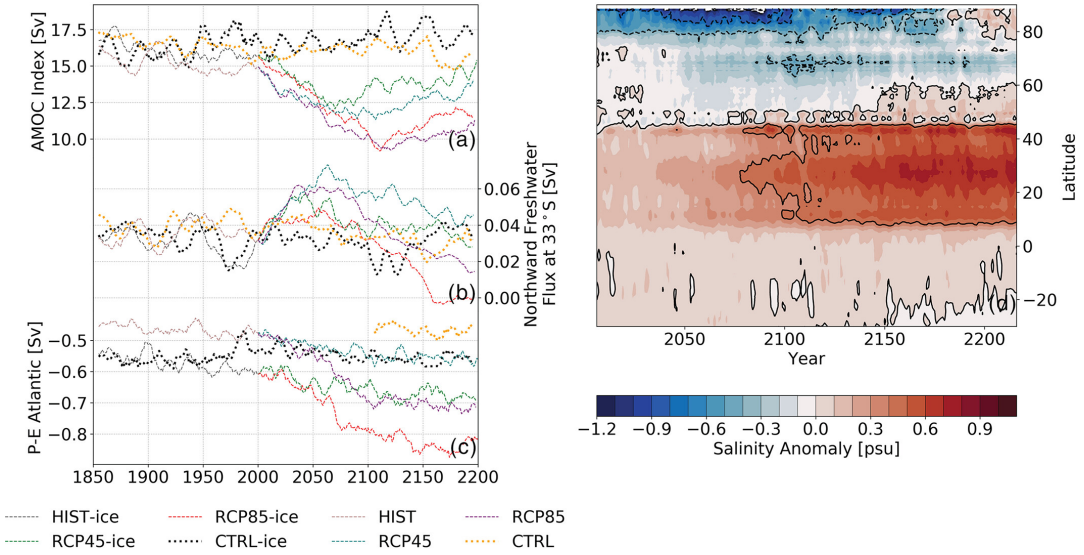

FIGURE 4.3: Time series of 11-year mean of (a) AMOC Index, defined as the streamfunction maximum between depths of 200 and 2,000 m and 30-60°N, (b) index for northward freshwater flux over 33°S, approximated after Vries and Weber (2005), (c) $P - E$ integrated over Atlantic catchment area (Fig. 4.2d); for CTRL only the last 100 years are shown for $P - E$ Atlantic; (d) temporal evolution of salinity anomalies averaged over the upper 1,000 m of the Atlantic basin (Fig. 4.2d) in RCP8.5-ice.

Atmospheric and oceanic freshwater transport rates are analyzed to assess possible mechanisms leading to the AMOC recovery. The net freshwater export via the atmosphere is significantly larger than that via the ocean, changing from about -0.45 Sv and -0.55 Sv in the control states to between -0.7 and -0.8 Sv for the RCP8.5 scenario in the uncoupled and coupled model setup, respectively (Fig. 4.3c). This change overcompensates the decrease of oceanic freshwater import into the Atlantic (Fig. 4.3b) and leads to an increase in ocean salinity, as also found by Lohmann (2003) and Latif et al. (2000). This result is supported by the fact that the highest increase in salinity can be seen at around 40°N, spreading northward (Fig. 4.3d). While the North Atlantic shows a net atmospheric freshwater import (Fig. 4.2a), this is overcompensated by the net loss over the Central and South Atlantic (Fig. 4.2b and c). Figure 4.3d shows an initial increase in salinity between 0°N and 40°N, as suggested by Fig. 4.2d. These are the areas with the highest $P - E$ decrease. While there is an initial freshening between 40°N and 80°N, it turns into a positive salinity anomaly

from the year 2100 onward. This corresponds well with the AMOC slowdown and the decline in sea ice (Fig. 4.1c), as there is no sea ice anymore that could act as a southward carrier of fresh water from the polar region.

4.3 Feedback of the Greenland Ice Sheet

Overall the GIS is losing mass due to the increasing atmospheric temperatures. The total ice mass expressed as sea level equivalent is decreasing from around 7.18 m to around 7.14 m in the RCP4.5 scenario and to around 7.06 m in the RCP8.5 scenario by the year 2200, leading to a global sea-level rise of 0.04 and 0.12 m, respectively (Fig. 4.4a). The discharge contributes around 0.025 Sv to the ice mass loss and stays at a constant level throughout all simulations (Fig. 4.4d). The surface runoff increases from less than 0.01 Sv in the control run to around 0.013 Sv in the RCP4.5-ice scenario and to over 0.03 Sv in the RCP8.5-ice scenario (Fig. 4.4b). In contrast to that, basal melting does contribute hardly anything to the ice mass loss (see Supplement A). These numbers add up to a total ablation of around 0.04 Sv for RCP4.5-ice and 0.06 Sv for RCP8.5-ice. The actual ice mass change shows a decadal variability up to 0.015 Sv for RCP8.5-ice and is smaller for RCP4.5-ice (Fig. 4.4e). The difference between total ablation and ice mass change is mainly due to local snow accumulation at the surface of the ice sheet (Fig. 4.4c). The main areas of ice sheet growth are the southern and eastern parts of Greenland, whereas the western part is the main area of freshwater release (Fig. 4.4i and 4.4j). The integrated surface accumulation increases from 0.032 to around 0.04 Sv in the RCP4.5-ice scenario and to around 0.05 Sv in the RCP8.5-ice scenario (Fig. 4.4c) due to enhanced precipitation over Greenland.

The additional precipitation that leads to local ice sheet growth in the model with ISM is released to the ocean immediately via river routing in the model without ISM. Thus, only the net ice mass change is added to the surface runoff of the land surface model. Due to the increased variability, there are intervals in which the coupled model runoff is smaller than the uncoupled one. However, the averaged land surface discharge into the North Atlantic by Greenland is around 0.01 Sv higher in RCP8.5-ice than in RCP8.5 and around the same for RCP4.5-ice and RCP4.5 (Fig. 4.4f).

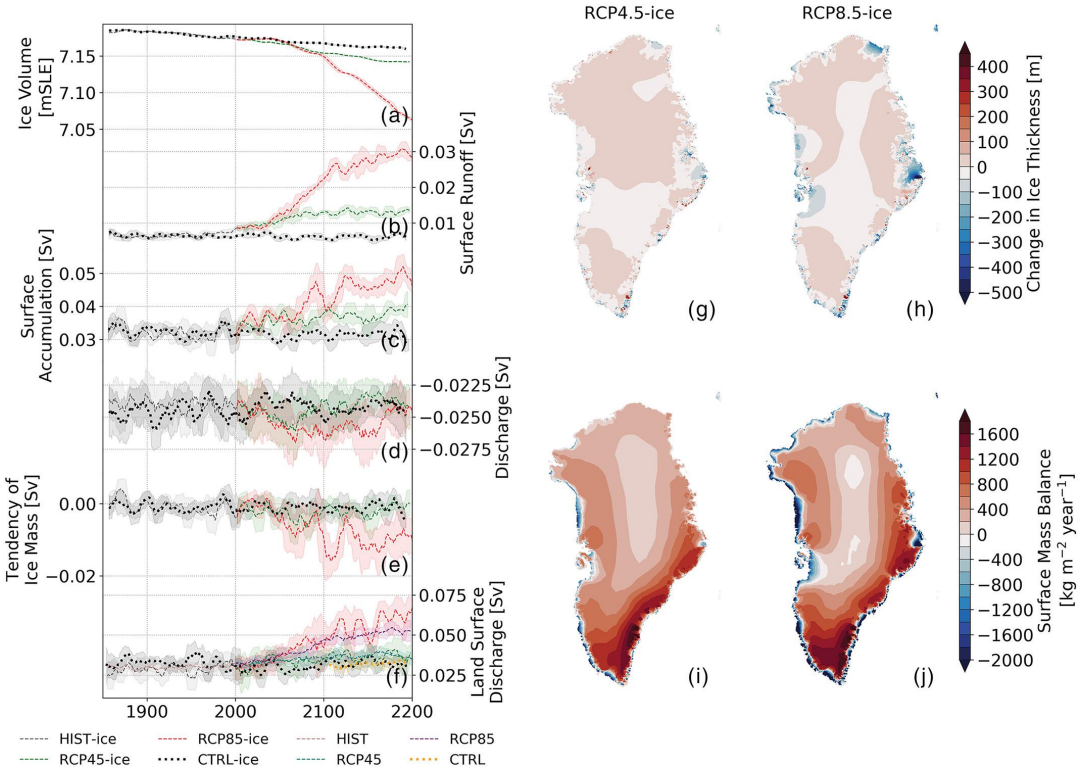

FIGURE 4.4: Time series of 11-year means and spatial changes of the GIS in the coupled simulations; shaded areas indicate 1 standard deviation. (a) The ice sheet's total volume expressed as sea-level rise potential, (b) surface runoff from the ISM, (c) surface accumulation, (d) discharge, (e) the ice sheet's total volume change, (f) surface runoff from the atmosphere model; for CTRL only the last 100 years are shown; (g and h) anomaly of the ice sheet's thickness for 2170–2199 for RCP4.5-ice and RCP8.5-ice, respectively; (i and j) the ice sheet's surface mass balance for 2170–2199 for RCP4.5-ice and RCP8.5-ice, respectively.

4.4 Discussion of the interactive ice sheet

The results show a net ice mass loss of the GIS in the future RCP8.5 scenario and, to a lesser extent, in the RCP4.5 scenario. While the land surface model captures the surface runoff, other mechanisms like the melt elevation feedback or basal melting and iceberg discharge are missing. The results show that the total ablation of the GIS is increased by around 0.01 Sv for the RCP8.5 scenario by including a dynamic ice sheet model in the climate model. However, this additional 0.01 Sv is rather small compared to around 0.025 Sv of discharge alone. Due to the coupling mechanism, the absolute freshwater release is balanced out to some extent by local snow accumulation. Therefore, the signals in the tendency of ice mass and the land surface discharge are opposite, meaning that the GIS surface mass balance is potentially buffering the bare surface

runoff of the land surface model. However, the strong decadal variability in the GIS mass balance is not seen for the AMOC. There is an interval between 2006 and around 2020, where the land surface discharge of RCP8.5-ice is lower than that of RCP8.5, corresponding to the positive GIS mass balance in this interval. However, the differences are relatively small and lay within the standard deviation of the time series. The amounts of freshwater released to the ocean of around 0.04 Sv in the RCP4.5-ice and around 0.06 Sv in the RCP8.5-ice (Fig. 4.4f) are in accordance with the results from Lenaerts et al. (2015). As the surface runoff, discharge, and basal melting are treated equally, and all accounted as surface runoff, all melt-induced freshwater is released into the ocean directly. Therefore, no effects of iceberg transport are captured.

While the AMOC is around 1 Sv stronger in the coupled results than in the uncoupled ones, this seems to be due to a different initial state caused by coupling the ice sheet into the model. The overall trends of the AMOC are similar for both models: a decrease throughout the 21st century by around 7.5 Sv and a recovery starting at the beginning of the 22nd century. The total freshwater release of around 0.06 Sv brought into the ocean by the GIS in the coupled model setup is not sufficient to keep the AMOC in a weak state. This result is in contrast to the findings of Vizcaíno et al. (2008) and Mikolajewicz et al. (2007), who found freshwater perturbations of 0.02-0.03 Sv to be sufficient for preventing a recovery. Studies by Golledge et al. (2019) found a recovery of the AMOC in a simulation run without ice sheet feedbacks for the RCP8.5 scenario. However, although these studies did include dynamic ice sheet models, they used coarser ocean grids, not able to depict North Atlantic ocean currents.

Different authors argue that a positive Atlantic freshwater import constitutes a negative feedback for the AMOC, leading to a recovery of the AMOC after an initial perturbation (Jackson, 2013; Liu et al., 2013; Rahmstorf, 1996). This is in accordance with the results (Fig. 4.3b). The changes in the Atlantic freshwater import are little compared to the changes in $P-E$ over the southern and central Atlantic (Fig. 4.2) which seem to be the main contributor to the Atlantic salinity increase. The positive salinity anomaly in the North Atlantic follows a trend observed since the 1950s (Stocker, 2014), which continues in the experiments conducted within the scope of this study. Studies by Lind et al. (2018) show that Barents Sea warming, observed since 1970, can be linked to a decrease in Arctic sea ice, resulting in enhanced evaporation and to an Atlantic-dominated regime. The negative anomalies in $P-E$ in the Baffin Bay, the Barents Sea, and the Kara Sea support this result (Fig. 4.2d). However, the strongest salinity

anomalies occur at around 40°N and seem to spread northward (Fig. 4.3d). The near-surface freshening may be the result of the AMOC weakening. The following positive salinity anomaly around 80°N may be the result of a reduction in sea ice transport from the polar region, as also seen in other studies by Liu et al. (2019).

In the newly developed coupled climate-ice sheet model AWI-ESM, climate warming scenarios are simulated, to assess the effects of melt-induced fresh water on AMOC. The oceanic multiscale model allows for resolving ocean boundary currents and regions of deep-water formation. The model shows an AMOC recovery for the RCP8.5 scenario (with fixed CO_2 forcing from 2100 onward) starting at the beginning of the 22nd century onward, for both versions with and without a dynamic ISM. The differences in the experiments are relatively minor. Also, the total freshwater release from the Greenland Ice Sheet is similar for both versions. However, the interactive ISM adds pronounced decadal variability to the surface runoff into the North Atlantic, resulting in intervals, where the surface accumulation overcompensates the ice sheet melting. This feature is not present in conventional climate models, as they lack ice sheet dynamics.

The results also suggest that the atmospheric freshwater transport by enhanced evaporation in the Atlantic realm plays a major role in an AMOC recovery. The net increase in evaporation over the central and southern Atlantic is stronger than the increase in precipitation in the North Atlantic.

5. The last inception with a coupled climate-ice sheet model

The late Pleistocene is characterized by the repeated advance and retreat of Northern Hemisphere ice sheets. These glacial cycles occur in intervals of ∼100 kyr. While it is commonly accepted that the large-scale variations in ice-sheet buildup and retreat are driven by changes in the orbital parameters, the processes involved are complex. Several feedbacks between the climate system and the cryosphere, like the ice-albedo feedback or the ice-elevation feedback, play a role in the dynamic response of climate and ice sheet to changes in orbital parameters. There are two hypotheses about the characterization of large-scale inception of North America: 1) ice sheet buildup occurs as a large-scale thickening of snowfields (Andrews and Mahaffy, 1976). Hence, surface mass balance changes induced by variations in surface temperature and precipitation are key for glaciation, and 2) small-scale high-elevation ice sheets act as nuclei (Weertman, 1964). Here, glaciation depends more on internal ice sheet dynamics.

The last glacial inception occurred between 120 ka and 110 ka, following the Eemian warm period. However, there are large uncertainties about the exact timing and the magnitude of glaciation. Estimates for global sea-level drop by 110 ka range from 10 m to 70 m (Hasenclever et al., 2017). It is commonly assumed that North American ice sheets significantly contributed to this sea-level drop. However, the evolution of individual ice sheets during the LGI is not well constrained, as the geological record of the Last Glacial Inception (LGI) has been destroyed by the subsequent advance and retreat of Northern Hemisphere ice sheets. Hence, ESMs are an important tool for gaining a better understanding of the processes involved in the ice-sheet buildup. However, due to the high computation costs and the long time scales that need to be covered by climate model simulations, there are only a few studies employing complex coupled climate-ice sheet models. Most studies use simplified model setups.

One approach is the usage of a coupled climate-ice sheet model that employs an EMIC as the climate component (Calov et al., 2005a; Calov et al., 2005b;

Bahadory et al., 2021; Ganopolski et al., 2010; Ganopolski and Brovkin, 2017). Due to their limited resolution, these models need to parameterize several processes and might lack important processes involved in ice-climate feedbacks. More facilitated climate models can be employed in a coupled transient fashion when the climate component is updated infrequently, but the ice sheet model runs continuously, e.g., in Herrington and Poulsen (2011) and Ridley et al. (2010). These experiments lack an actual transient response and might show abrupt changes in climate and ice sheet dynamics.

Using an EMIC with interactive ice sheets, Kageyama et al. (2004) simulated glaciation over large parts of North America by 110 ka, and stressed the importance of albedo and vegetation feedbacks. With their model successor CLIMBER-2, Ganopolski et al. (2010) were able to simulate a full glacial cycle. They prescribed aeolian dust fields and employed a correction of atmospheric temperature biases. The important role of dust deposition on ice albedo was supported by follow-up studies (Ganopolski and Brovkin, 2017; Willeit and Ganopolski, 2018). Also, using CLIMER-2, Calov et al. (2005a) found the snow-albedo feedback to be the main driver of glacial inception, which started at 117 ka in their simulations and reached a total volume of around 90 mSLE by 110 ka. They discuss the glacial inception to be a bifurcation transition in the climate system from an interglacial to a glacial state, which depends on a threshold of the high-latitudinal summer insolation. Furthermore, they state that for present-day climate, a glacial as well as an interglacial equilibrium state exists. In a follow-up study, Calov et al. (2005b) found the orbital forcing sufficient for triggering the glacial inception, while changes in GHG concentration are of minor importance. Using another coupled EMIC, Bahadory et al. (2021) performed an ensemble of transient simulations of the LGI and found the peak of ice volume at 111 ka of nearly 40 mSLE. Their simulations show a large Fenno-Scandian ice sheet and a merged Cordilleran and Laurentide ice sheet. They found the inception started from high-latitudinal ice nuclei.

Here, for the first time, a comprehensive complex coupled climate ice sheet model with dynamic vegetation and a horizontal resolution of up to $1/3^\circ$ in the North Atlantic is employed to run transient simulations of the Last Glacial Inception (LGI) between 125 ka and 110 ka. The climate and ice sheet models are coupled asynchronously, allowing for efficient computational costs while including essential physical feedback processes, like ice-albedo and ice-elevation feedback. This study aims to improve the understanding of processes involved in the LGI and addresses the question of whether snowfield thickening or the

spreading of ice nuclei is the dominant mechanism of large-scale glaciation.

5.1 Model setup for the cooling case

A climate-only spinup has been run for 560 years with fixed 125 ka orbital and GHG forcing. The equilibrated climate spinup has been coupled to a pre-industrial ice sheet state and run with transient orbital (Berger, 1978) and GHG (Köhler et al., 2017) forcing from 125 ka to 115 ka (125^{PI}). The coupled model is run asynchronously with an acceleration factor of ten. The lengths of the climate and ice sheet model chunks are two and twenty, respectively. Due to the asynchronicity, this corresponds to 10,000 ice sheet model years and 1,000 climate model years. Another experiment is run from 125 ka to 110 ka with the same and prolonged forcing and configuration used as in 125^{PI} but with an anomaly coupling applied with respect to near-surface temperature and precipitation in between ECHAM and dEBM ($125^{\mathrm{PI}}_{\mathrm{anom}}$). The monthly anomaly applied is derived from a coupled historical experiment and calculated against the NCEP reanalysis (Kalnay et al., 1996; Kistler et al., 2001; Saha et al., 2010) for the period 1948 to 2010 (Fig. 5.6). A third experiment is run with the same forcing and configuration applied as the experiments above, also using an anomaly coupling, but with a different initial ice sheet ($125^{\mathrm{PI}}_{\mathrm{125ka}}$). For this experiment, an additional spinup has been run with the coupled climate-ice sheet setup under fixed 125 ka orbital and greenhouse gas forcing ($\mathrm{spinup}_{\mathrm{125ka}}$) to account for a lower bound of initial ice sheet volume. This spinup has been run asynchronously with an acceleration factor of 50 for 140 climate, respectively, 7,000 ice sheet years. Furthermore, a control run with fixed pre-industrial forcing has been run for 1,000 climate and 10,000 ice sheet model years ($\mathrm{PI}_{\mathrm{anom}}$), respectively. All experiments are summarized in Table 5.1.

5.2 Change in solar radiation

In the following, the development and the temporal evolution of Northern Hemisphere ice sheets are examined. This is done for the coupled climate ice simulation with fixed 125 ka forcing and for the transient runs with and without anomaly coupling. As ice sheets form independently at different locations, five regions of ice sheet development are examined. These are Greenland (GIS), Quebec (Qb), Baffin Island and the Arctic Archipelago (Bf), the Cordilleran Mountains (CIS), and Scandinavia (Sc) (Fig. 5.2). Figure 5.1 summarizes the

TABLE 5.1: Experiments run within the scope of this chapter. *EXP. ID* indicates the name used for this experiment throughout this chapter; *anom cpl.* indicates whether an anomaly coupling is applied; *init ice sheet* indicates whether a pre-industrial ice sheet configuration or a reduced ice sheet from the 125 ka spinup is used; *run length clim.* and *run length ice* indicates the length of the simulation in climate model years and ice sheet model years, respectively.

EXP. ID	anom cpl.	init ice sheet	run length clim.	run length ice
$\text{spinup}_{\text{clim}}$	-	-	700	-
125^{PI}	no	PI	1,000	10,000
$125^{\text{PI}}_{\text{anom}}$	yes	PI	1,000	10,000
$\text{spinup}_{125\text{ka}}$	yes	PI	100	5,000
$125^{125\text{ka}}_{\text{anom}}$	yes	125ka	1,000	10,000
PI_{anom}	yes	PI	1,000	10,000

orbital (a) and greenhouse gas (b) forcings applied, as well as the top incoming solar radiation and the yearly mean near-surface temperatures over North America (c). Furthermore, individual ice sheet volumes of the ice sheets mentioned above are expressed in meter sea level equivalent (mSLE) for all transient experiments 125^{PI}, $125^{\text{PI}}_{\text{anom}}$, and 125^{125}_{anom}.

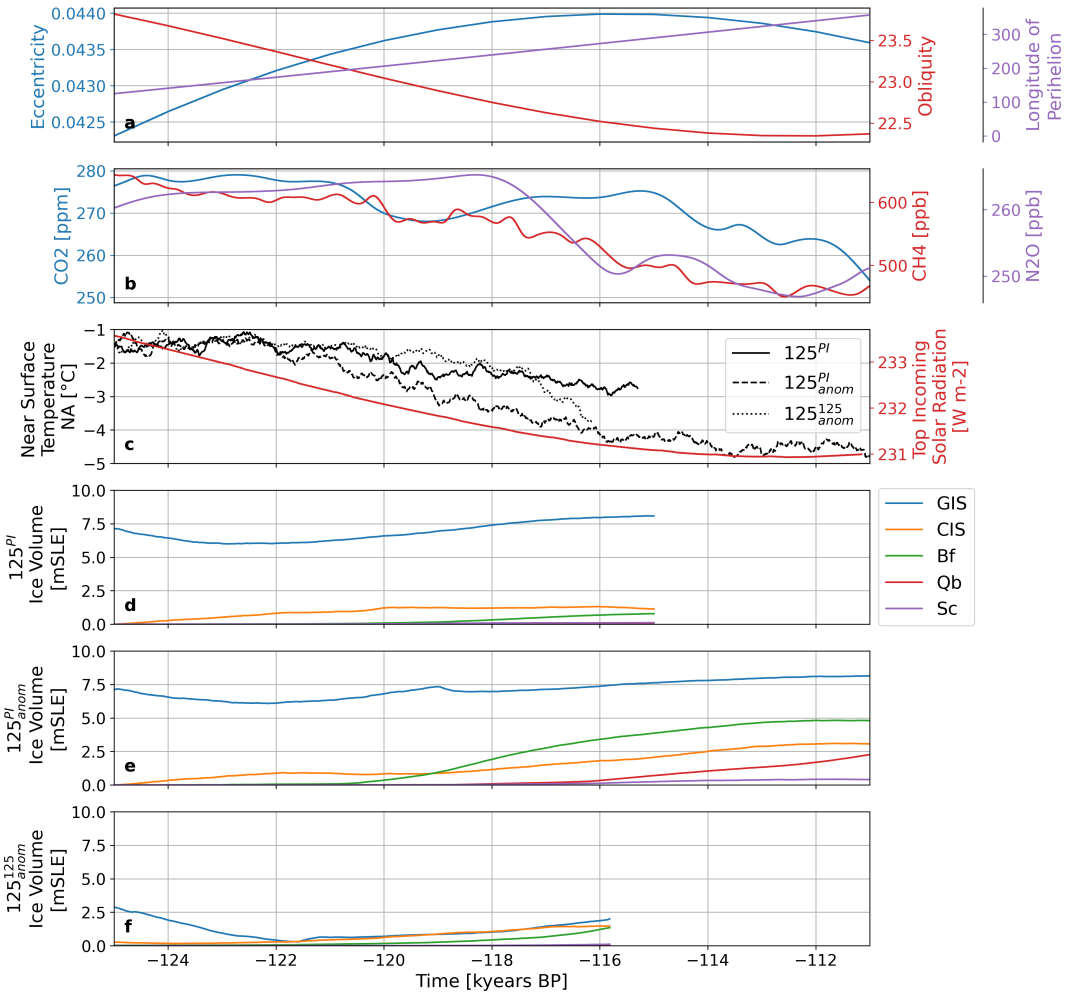

FIGURE 5.1: Timeseries over the interval from 125 ka to 111 ka of the orbital parameters eccentricity, obliquity, and longitude of perihelion from Berger (1978) (a); concentrations of the greenhouse gases CO_2, CH_4, and N_2O Köhler et al. (2017) (b); top incoming solar radiation at 60°N, and 30-year rolling mean of near-surface air temperature (c); volumes of different Northern Hemisphere ice sheets expressed as sea level equivalent (d), (e) and (f).

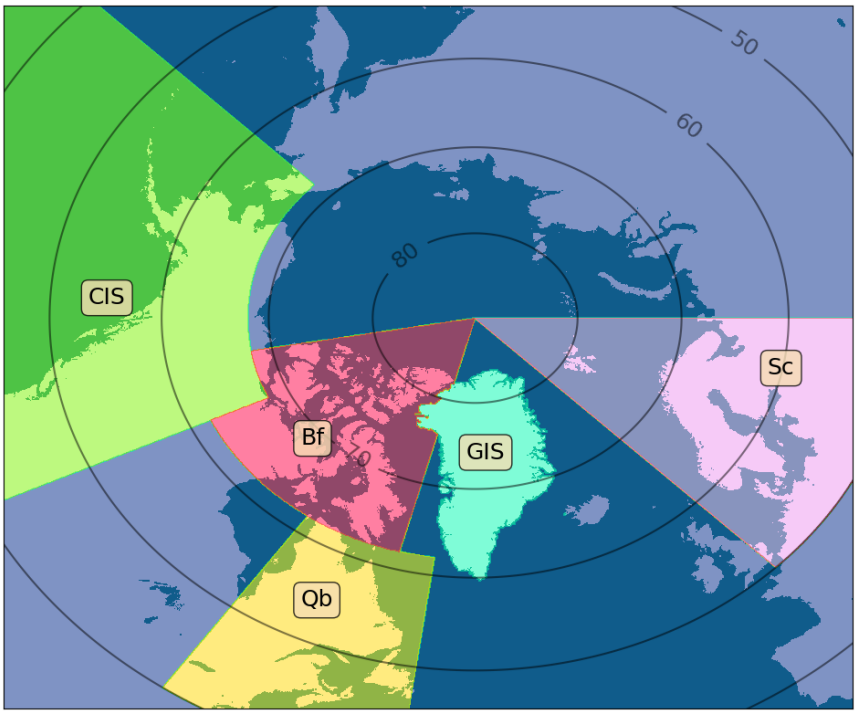

FIGURE 5.2: Regions of ice sheet development: Greenland (GIS), Quebec (Qb), Baffin Island and the Arctic Archipelago (Bf), the Cordilleran Mountains (CIS), and Scandinavia (Sc).

Figure 5.3 shows the top incoming solar radiation for different time slices with respect to the pre-industrial radiation. During the Eemian (125 ka), it is increased by around 60 Wm^{-2} in the summer season (JJA) and reduced by 50 Wm^{-2} during autumn (SON) in the Northern Hemisphere. However, obliquity already peaked before, and insolation maxima are becoming less pronounced until around 119 ka, where a negative insolation anomaly during spring and summer can be seen. The total incoming solar radiation at 60° reaches a minimum at around 113 ka (Fig. 5.1c) and mainly follows the obliquity (Fig. 5.1a). The yearly mean near-surface air temperature over North America lags behind the incoming solar radiation signal by a few millennia. It starts to decrease by 122 ka from around -1.5°C to around -4.5° by 114 ka (Fig. 5.1c).

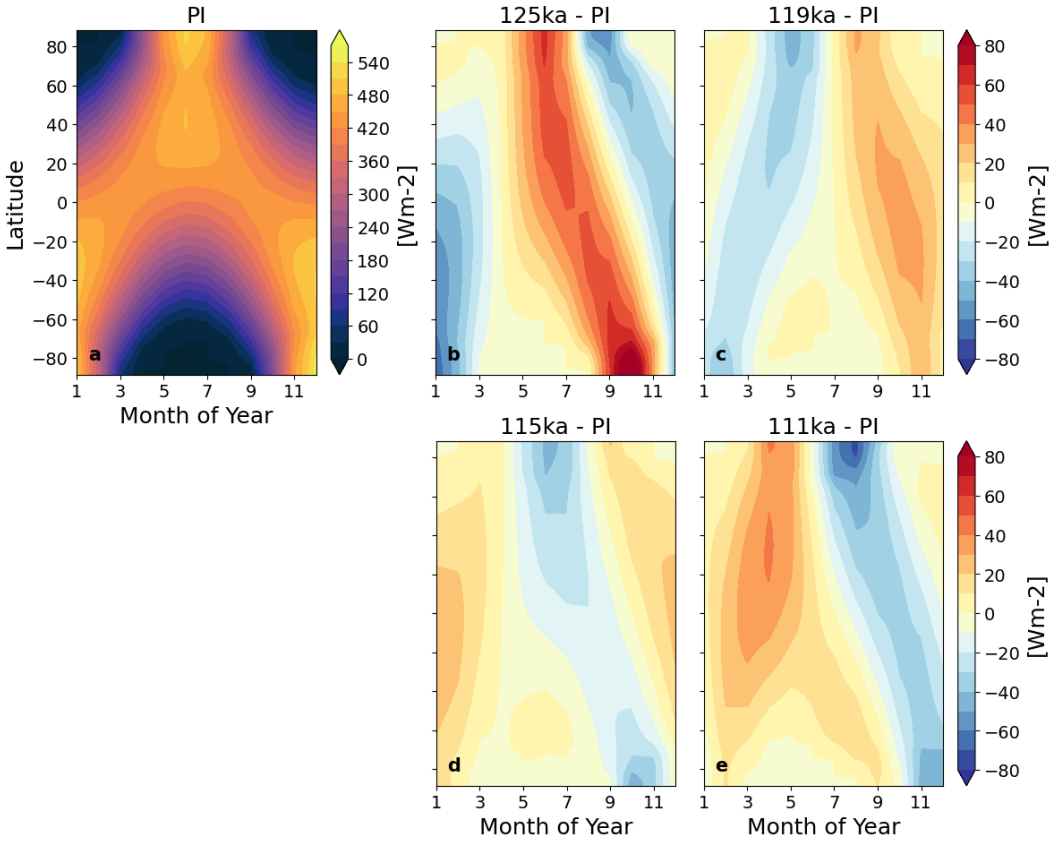

FIGURE 5.3: Top incoming solar radiation for the pre-industrial time and anomalies for time slices 125 ka, 119 ka, 115 ka, and 111 ka.

5.3 Transient simulation 125 ka - 115 ka

The experiment 125^{PI} shows a decline of the GIS from around 7.2 mSLE to roughly 6 mSLE from 125 ka to 122 ka (Fig. 5.1d). This result indicates a potential contribution of the GIS to global sea-level rise during the Eemian of up to 1.2 m. A value at the lower limit of other model studies (Calov et al., 2015; Goelzer et al., 2016; Quiquet et al., 2013; Robinson et al., 2011; Stone et al., 2013; Plach et al., 2018). However, a Cordellerian Ice Sheet starts to develop instantaneously, compensating around 1 mSLE of GIS melting by 122 ka. From 122 ka, the GIS recovers and grows to a total volume of 8 mSLE by 115 ka. The CIS grows to around 1.2 mSLE by 120 ka and stays at a rather constant volume from that on. A small ice sheet develops on Baffin Island (Bf), reaching a volume of 0.8 mSLE by 115 ka. No ice sheets develop in the Quebec region. Figure 5.4 shows the ice sheet thickness for 125^{PI} at different time slices. It can be seen that during the GIS minimum at 122 ka, parts of North and East Greenland are ice-free (Fig. 5.4a). Two domes develop, one covering central Greenland and the other one in South Greenland, with a gap between them where ice thickness drops to around 1,000 m. Over the Cordilleran Mountains, two ice sheets develop that start to merge by 115 ka (Fig. 5.4c). The ice sheet over Baffin Island is limited to the north-western margin and grows mainly in height, not in spatial extent (Fig. 5.4b and c). The mean summer temperatures are above 0°C over large parts of Baffin Island and above 5°C over large parts of the northern North American mainland (Fig. 5.4), preventing a perennial snow cover in these regions. This is also recognizable in the climatic surface mass balance (Fig. 5.4 d-f). It is positive over the GIS and the CIS, most pronounced over the south-eastern part of the GIS with values up to 2,000 kg m^{-2} yr^{-1} and small areas of Baffin Island from 117 ka on. The strong positive climatic mass balance over South-East Greenland is compensated by a divergent ice flow from this region toward the ice sheet margin. Southern parts of Baffin Island and the northern parts of Quebec show a reduced negative climatic mass balance at 117 ka (Fig. 5.4 e). However, the climatic mass balance does not become positive in these regions. Hence, the climatic conditions are not sufficient to facilitate the development of ice sheet nuclei in the Quebec region and the large-scale glaciation of Baffin Island. Regarding the climatic trends, the results show a cooling trend in the high latitudes, especially in the Arctic, of up to 1 K ky^{-1}, and a warming trend in the Tropics, especially pronounced in the Sahel region of around 0.5 K ky^{-1} (Fig. 5.5).

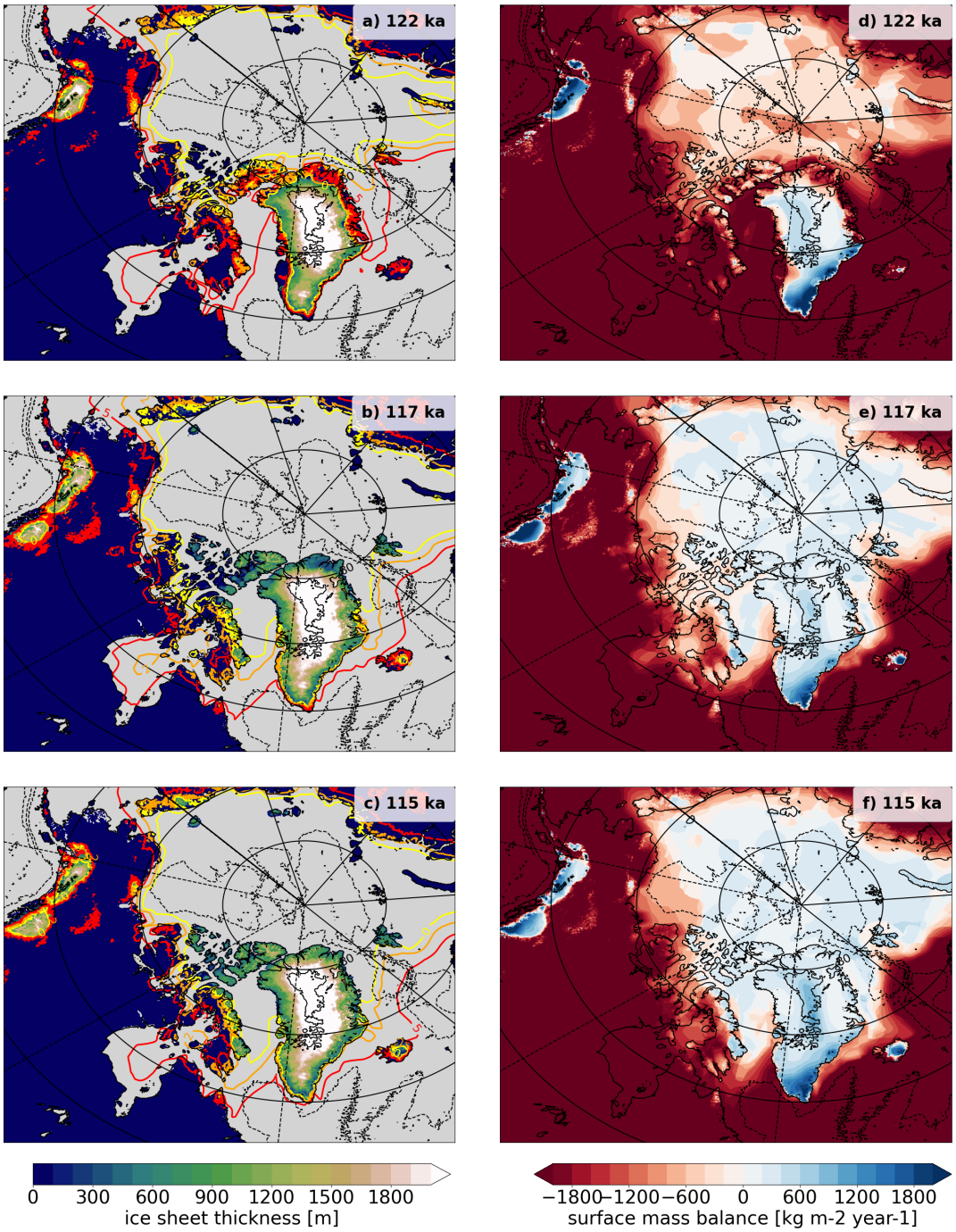

FIGURE 5.4: a-c) Ice sheet thickness for time slices 122 ka, 117 ka, and 111 ka for 125^{PI}. The contour lines indicate 0°C, 5°C, and 10°C of JJA mean near-surface temperature; d-f) like a-c) but for climatic surface mass balance.

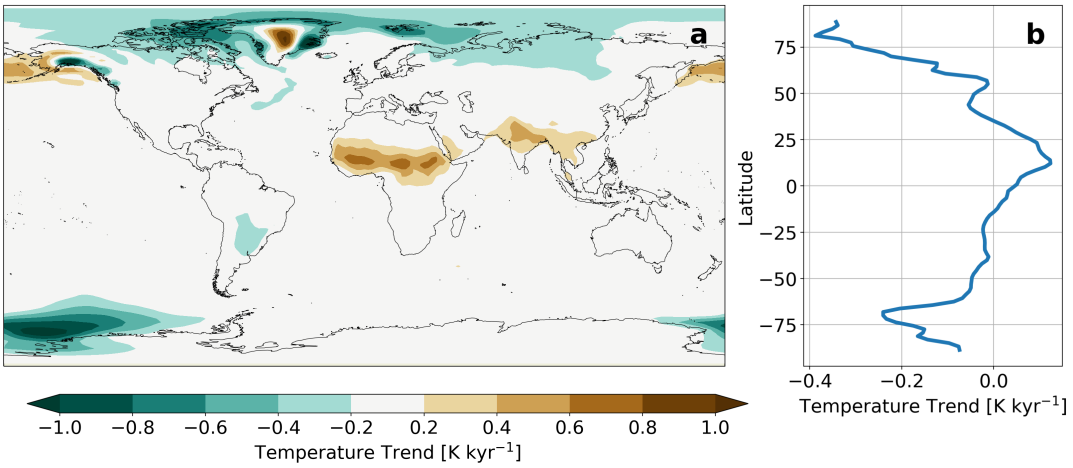

FIGURE 5.5: Trend in near-surface air temperature for 125^{PI} from 125 ka to 115 ka and zonal averages.

The warming over Greenland is associated with reduced ice sheet height over central Greenland compared to the initial ice sheet, for which a pre-industrial configuration was chosen. Furthermore, the strong cooling over the Cordilleran Mountains also stems from the elevation ice feedback due to the growth of a relatively high ice sheet in this region. On zonal average, a cooling of more than 0.3 K ky^{-1} at 75°N and further north and a warming of over 0.1 K ky^{-1} in the northern Tropics can be seen (Fig. 5.5b). The general trend matches the results by Bakker et al. (2014). However, the cooling over North America is less pronounced in the results, and the cooling in the high northern latitudes is not captured when compared to proxy data (see Fig. 6 in Bakker et al. (2014)).

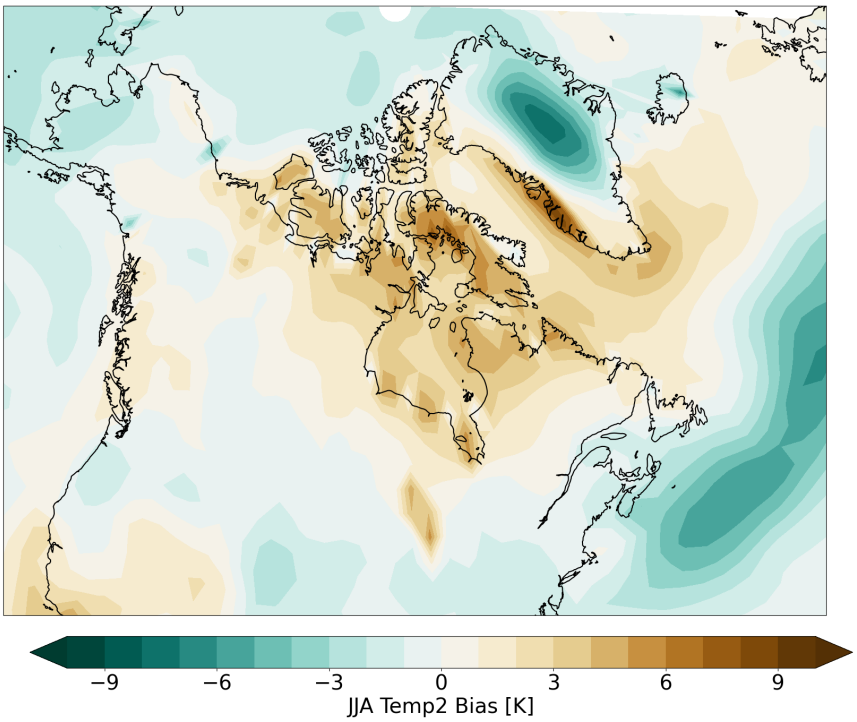

FIGURE 5.6: Near-surface summer air temperature bias. The bias is calculated as the difference in the multi-annual monthly mean from 1948 to 2010 between a historical simulation and the NCEP (Kalnay et al., 1996; Kistler et al., 2001; Saha et al., 2010) reanalysis dataset.

5.4 Transient simulation 125 ka - 115 ka with anomaly coupling

To facilitate ice sheet development and overcome anomalous high air temperatures, an anomaly coupling has been applied. Figure 5.6 shows the model bias in summer 2 m-temperature for the standard model setup without anomaly coupling. The model shows too high temperatures, especially around Hudson Bay and over Baffin Island and Quebec region, of up to 5 K. In order to account for this model bias, a transient simulation with the same forcing as 125^{PI} has been run but with anomaly coupling ($125^{\mathrm{PI}}_{\mathrm{anom}}$). Figure 5.7 shows the ice thickness for different time slices. The evolution of the Greenland Ice Sheet is similar to 125^{PI}. Also, the Cordelleriean Ice Sheet develops early. However, already by 119 ka, Baffin Island is glaciated by a larger extent than in 125^{PI}, and by 117 ka, it is fully glaciated (Fig. 5.7d). The faster and more excessive growth of ice over Baffin Island can also be seen in Fig. 5.1e, where the total volume reaches around 0.8 mSLE by 119 ka, exceeding the total volume of CIS.

Furthermore, ice nuclei develop along the coast in Quebec and Keewatin (Fig.

5.7d). The northernmost parts of North America show mean summer temperatures below 0°C, and the 5°C and 10°C isolines of mean summer temperature lie further south than in 125^{PI} (Fig. 5.7 and 5.4). The CIS continues to grow, and an ice cap forms over Scandinavia. In 115 ka, the glaciated areas over Quebec merge and reach heights up to 2,000 m. Similarly, the ice sheet over Keewatin continues to grow. The Scandinavian ice sheet grows mainly in extent and covers large parts of Norway, and small ice caps form in Siberia. Total ice volume reaches around 17 mSLE (Fig. 5.1e). By 111 ka, ice shelves have developed in the Quebec region and the Arctic Archipelago. By 113 ka, the two small ice sheets over the Quebec area have merged into a large one, and by 111 ka the crest of the Quebec ice sheet exceeds a height of 2,200 m (Fig. 5.7f). From all ice sheets examined, QbIS is the only one continuing to grow in 111 ka (Fig. 5.1e). Total ice volume reaches 18.5 mSLE, a value within the uncertainty range of different reconstructions (Hasenclever et al., 2017).

The climatic mass balance shows a shallow gradient over the Quebec area in 117 ka, eventually resulting in a positive mass balance over this region (Fig. 5.8). In 111 ka, this gradient has become steep, and there is an abrupt transition from negative to positive values along the ice sheet margin. Hence, the Quebec ice sheet continues to grow only in height and not in spatial extent, as also indicated by the steep gradient in mean summer temperature in Fig. 5.7f. In the early stage of the ice sheet development, the spatial expansion is mainly driven by the surface mass balance. Internal ice sheet dynamics contribute only little (see SupplementB and C). Furthermore, the surface mass balance is affected by the latitudinal shift of maximum near-surface temperature. This results in a reduced surface mass balance at the southern margin of the Quebec ice sheet in 111 ka (Fig. 5.8c), the region that is exposed to positive near-surface temperatures over summer (Fig. 5.7f).

The temperature trend is similar to 125^{PI} but with more pronounced cooling over North America (Fig. 5.9). This enhanced cooling stems from the large-scale glaciation and the associated decrease in albedo. Regarding the trend in precipitation, a decrease of around 0.12 m y^{-1} kyr^{-1} in the Sahel region, Himalayan Mountains, and the Indian Ocean, and an increase in precipitation of up to 0.12 m y^{-1} kyr^{-1} in the southern Tropics and the Amazonas region (Fig. 5.9a) can be seen. However, changes in precipitation patterns in the high latitudes are small but can be seen over North America, indicating a minor role of precipitation changes for glacial inception.

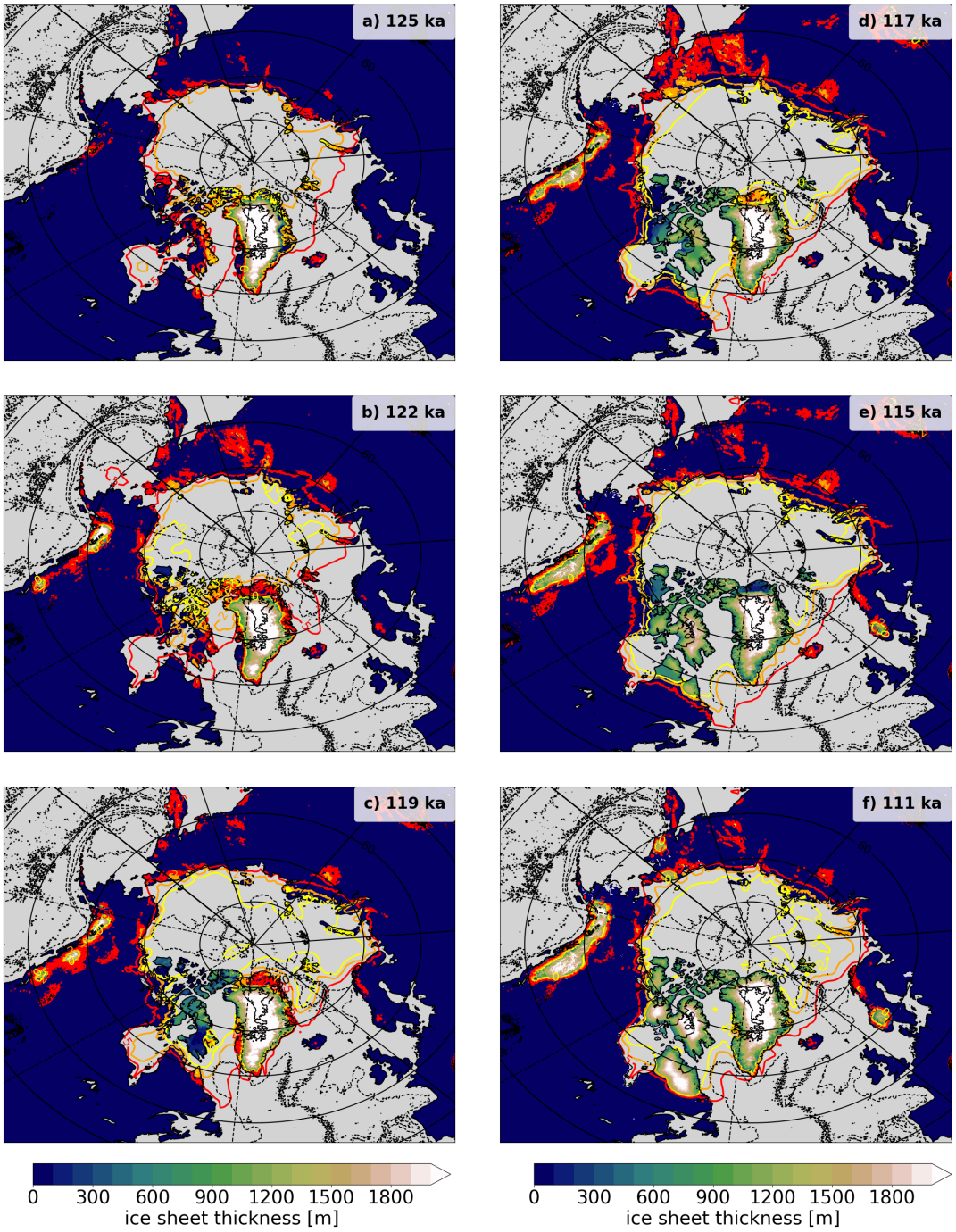

FIGURE 5.7: Ice sheet thickness for time slices 125 ka, 122 ka, 119 ka, 117 ka, 115k ka, and 111 ka for $125^{\mathrm{PI}}_{\mathrm{anom}}$. The red contour indicates the zero line of the yearly maximum near-surface temperature.

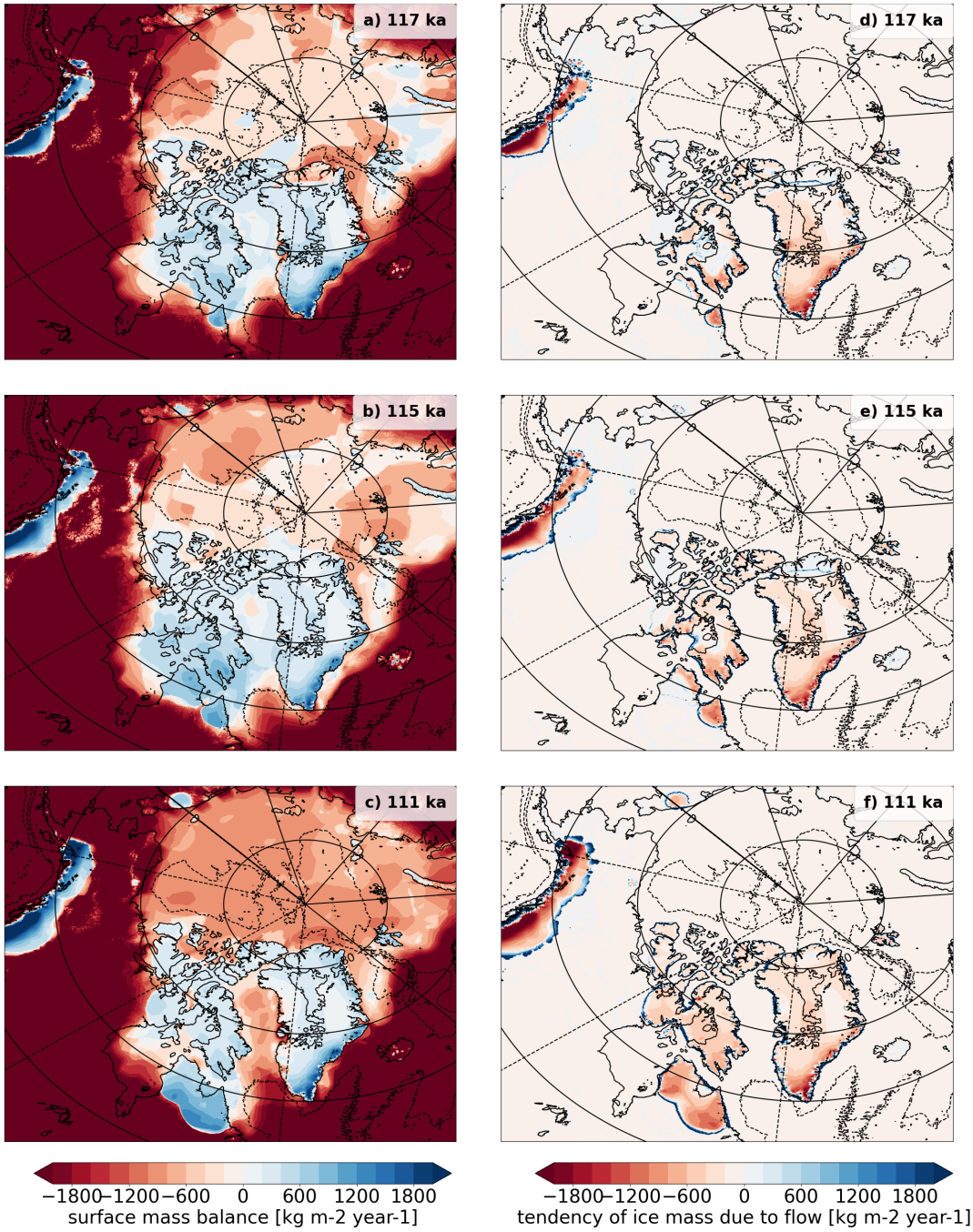

FIGURE 5.8: a-c) Climatic mass balance for time slices 117 ka, 115k ka, and 111 ka for $125^{\mathrm{PI}}_{\mathrm{anom}}$; d-f) like a-c) but for tendency of ice mass due to flow.

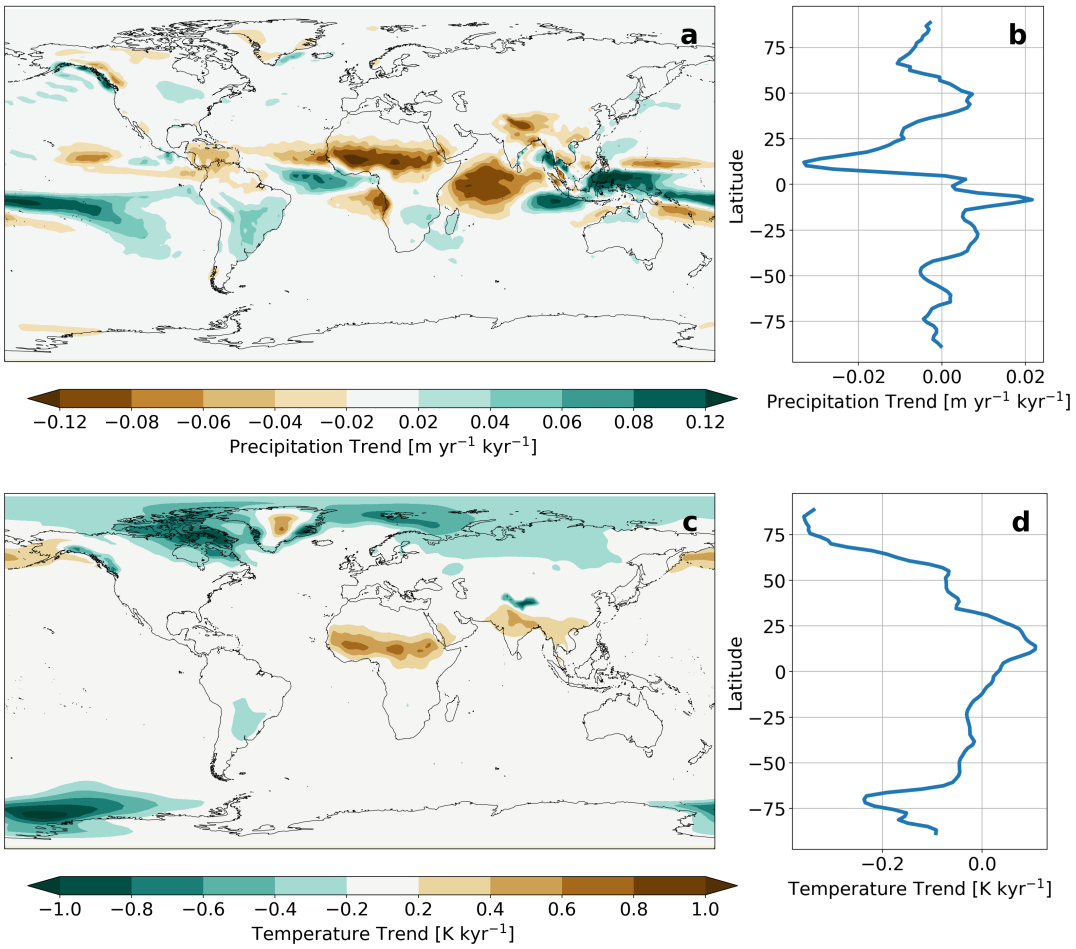

FIGURE 5.9: Trends in precipitation (a) and near-surface temperature (c) from 125 ka to 115 ka and zonal averages (b) and (d), respectively.

5.5 Simulation with anomaly coupling and reduced ice sheet

The implementation of an anomaly coupling is sufficient to facilitate large-scale glaciation over North America when the ice is initialized with a pre-industrial GIS. This constitutes an upper bound for the initial ice sheet volume when looking at the phase space of the initial and final ice sheet volume. However, the GIS is assumed to have been smaller during the Eemian than during pre-industrial times. To assess a lower bound, the transient experiment with anomaly coupling is repeated but with another initial ice sheet configuration. To obtain this initial ice sheet state, a coupled spinup has been run.

5.5.1 Coupled 125 ka spinup

The simulation with constant 125 ka forcing ($\text{spinup}_{125\text{ka}}$) shows a rapid decline in ice sheet volume from around 7 m to 3 m sSLE (Fig. 5.10) within 100 model years of the climate component which translates into 5,000 model years of the ice sheet component (please be aware that the acceleration factor is 50 for this experiment, Tab. 5.1). Large parts of Greenland become ice-free, and only two domes remain, a large one in central Greenland and a smaller one in south Greenland, respectively (Fig. 5.10). The Greenland Ice Sheet continues to decline and eventually vanishes nearly completely (not shown), indicating Eemian climate conditions are too warm to sustain even a small GIS when brought into equilibrium. However, GIS extent increases partly to the east, and a Corderllerian Ice Sheet develops, which peaks after around 2,000 model years (Fig. 5.10d). After 5,000 years, the ice sheet configuration depicted in Fig. 5.10c is taken as initial condition for $125^{125\text{ka}}_{\text{anom}}$. Collateral to the ice sheet decline, the global average near-surface temperature increases from around 13.6°C to 14°C (Fig. 5.10e) when the climate and ice sheet components are coupled together. This global warming can be mainly attributed to the warming of Greenland due to the ice-elevation feedback.

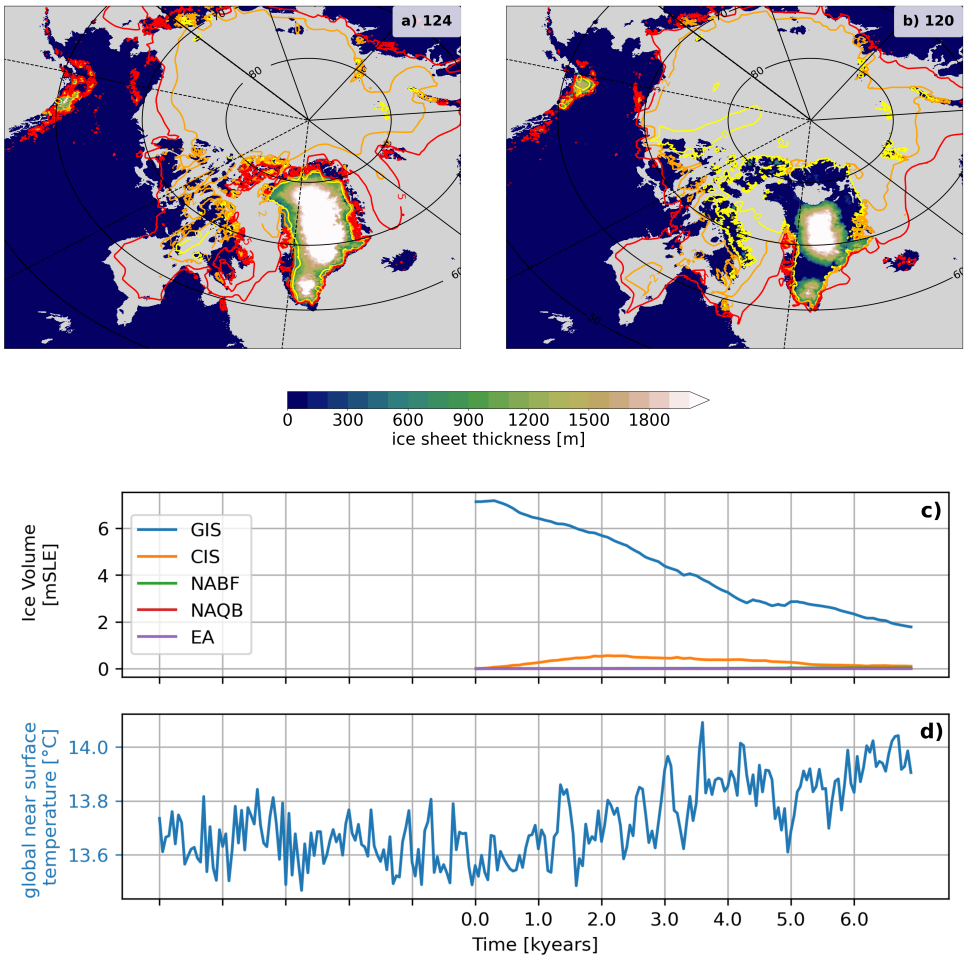

FIGURE 5.10: Ice sheet thickness of the coupled climate ice-sheet experiment with fixed 125 ka climate forcing (spinup$^{125\text{ka}}$) after a) 1,000 model years and b) 5,000 model years; and c) ice sheet volumes according to Fig. 5.2, as well as d) global average temperature. The x-axis indicates ice sheet model years for the coupled experiment, i.e., values in the left half of d) show the average global temperature for the climate-only spinup. The red contour in a) and b) indicates the zero line of the yearly maximum near-surface temperature.

5.5.2 Transient simulation 125 ka - 115 ka with anomaly coupling and reduced ice sheet

Figure 5.1f shows a continued decrease in GIS volume until 122 ka. This matches the temporal evolution from the experiments 125^{PI} and $125^{\mathrm{PI}}_{\mathrm{anom}}$ and shows that the date of GIS minimum volume is independent of the initial state. However, a CIS develops, and parts of Baffin Island glaciate, similar to 125^{PI}. Figure 5.11 shows the ice sheet thickness for time slices 122 ka, 120 ka, and 116 ka. By 122 ka, GIS is nearly entirely ice-free except for some ice caps in central, east, and south Greenland (Fig. 5.11a). By 120 ka, the central Greenland Ice Sheet has recovered to a large extent (Fig. 5.11b), while by 116 ka, the central GIS has gone again mostly, but a larger ice sheet is centered more in the southeast of Greenland (Fig. 5.11c). By 116 ka, Baffin Island is entirely glaciated, and an ice cap is forming in the Quebec area (Fig. 5.11c).

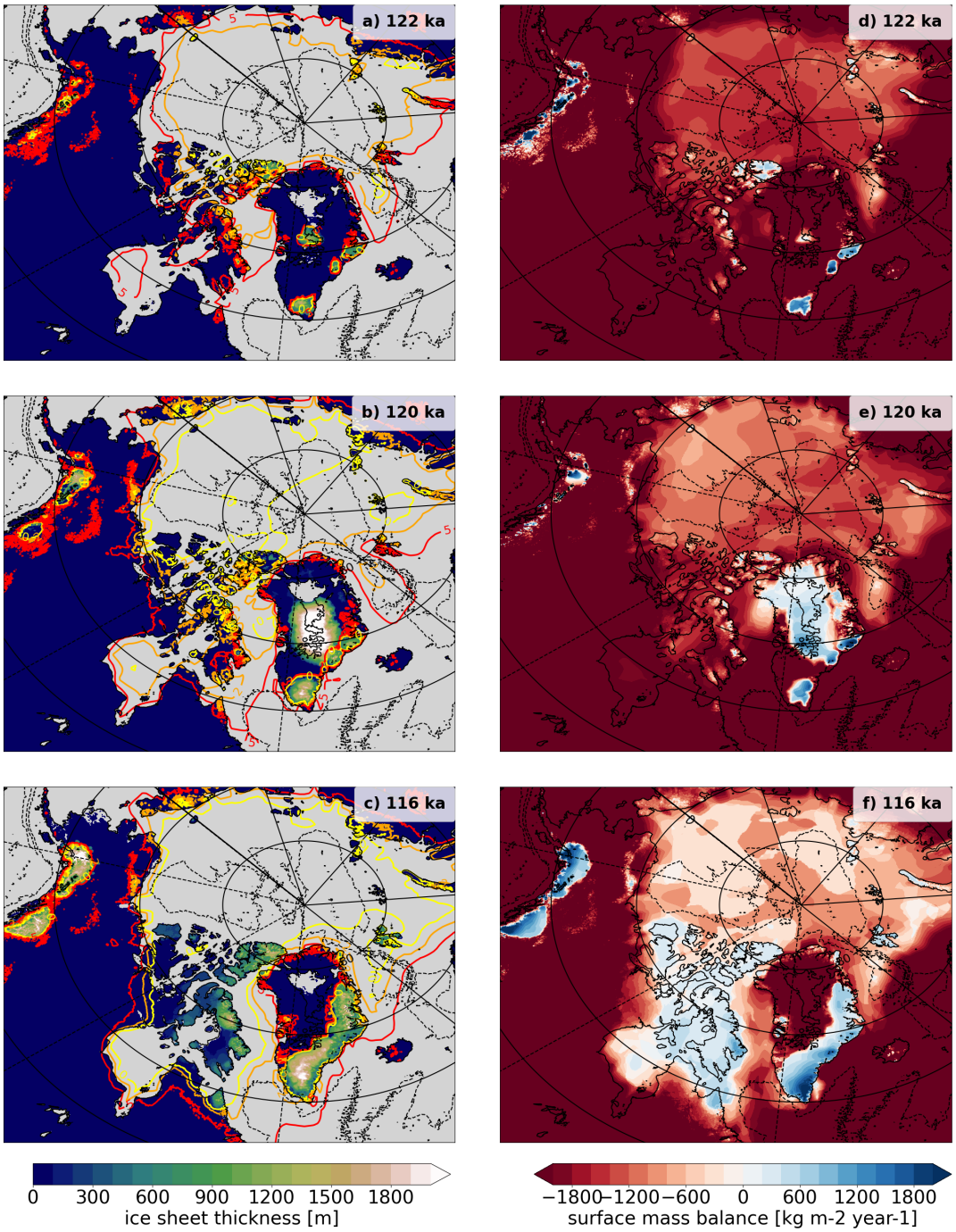

FIGURE 5.11: a-c) Ice sheet thickness for time slices 122 ka, 120 ka, and 116 ka for $125^{125\text{ka}}_{\text{anom}}$. The contour lines indicate 0°C, 5°C, and 10°C of JJA mean near-surface temperature; d-f) like a-c) but for climatic surface mass balance.

5.5.3 Pre-industrial control simulation

Additionally to the transient simulations, a pre-industrial control simulation (PI_{anom}) has been performed with fixed orbital and greenhouse gas forcing. The same initial ice sheet as in 125^{PI}_{anom} is used and the anomaly coupling is applied. Figure 5.12a shows the mean yearly near-surface air temperature with a minimum of -2°C after 4,000 model years (Please note that the x-axis shows ice sheet model years. As the acceleration factor of the coupled setup is set to ten, this corresponds to 400 climate model years). Afterward, the temperature levels off at around -1.5°. A Cordilleran ice sheet develops and grows to around 1.5 mSLE after 3,000 model years but nearly completely vanishes again afterward. An ice sheet over Baffin Island reaches its peak of around 1.5 mSLE after around 5,000 model years and decreases slowly afterward. The maximum CIS extent, as well as the glaciation of Baffin Island, can be seen in Fig 5.13b. Furthermore, the GIS shows a maximum extent after 3,000 model years and loses ice afterward in the west. Although Baffin Island is glaciated to a large extent, it is not fully covered by ice like in 125^{PI}_{anom} (Fig. 5.7). An ice nucleus develops in the Quebec region (Fig. 5.13c), and a reduced negative surface mass balance can be seen initially along the northern coastline (Fig. 5.13d and e). However, the climatic conditions are not sufficient for the buildup of a large ice sheet.

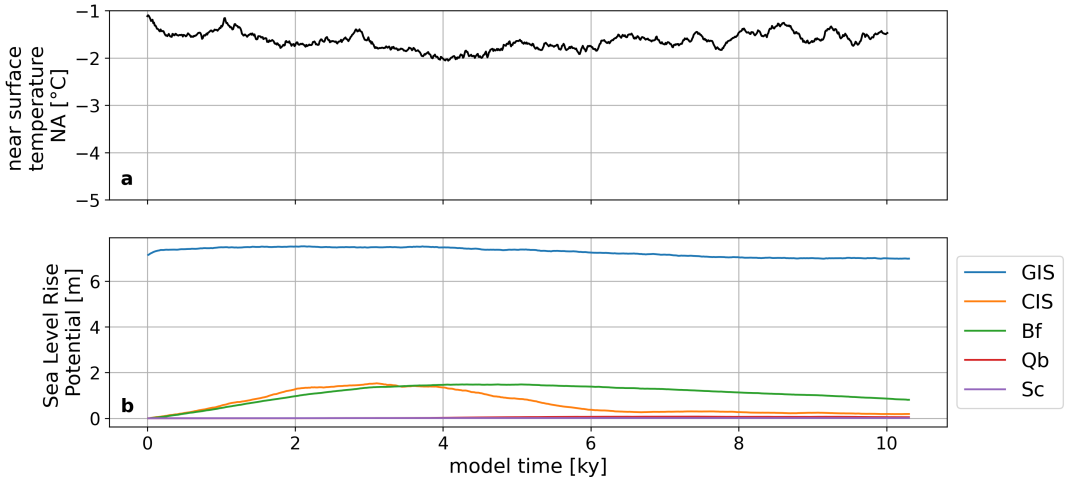

FIGURE 5.12: Time series for the PI_{anom} experiment a) near-surface summer temperature over North America; b) ice sheet volume for different regions defined in 5.2 expressed in sea level equivalent.

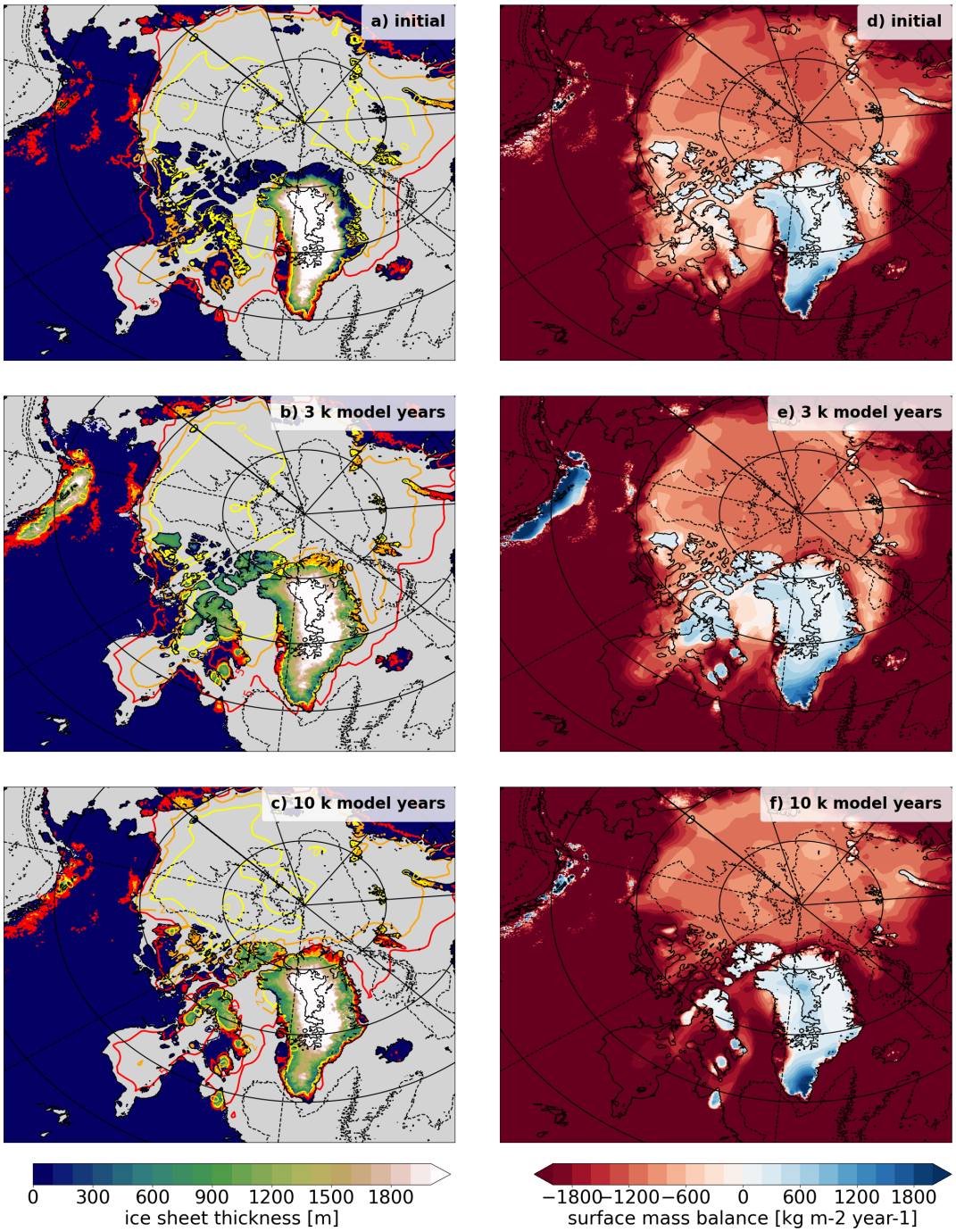

FIGURE 5.13: a-c) Ice sheet thickness for the initial ice sheet and after model years 3 ka and 10 ka for PI_{anom}. The contour lines indicate 0°C, 5°C, and 10°C of JJA mean near-surface temperature; d-f) like a-c) but for climatic surface mass balance. Model time is expressed in ice sheet model years.

5.6 Discussion of the glacial inception

In this study, long-term transient simulations with a comprehensive Earth system model have been performed, including interactive ice sheets for the last glacial inception from 125 ka to 110 ka. The results show a high sensitivity of the coupled model setup toward the climatic base state. With respect to the NCEP reanalysis dataset, the atmosphere shows strong warm biases of up to 5 K for JJA mean temperatures over North America, especially pronounced around Hudson Bay (Fig. 5.6). This matches with warm biases of sea surface temperature in the current generation of Earth system models (Zhang et al., 2023). While the obliquity seems to be the main driver, there is no automatism for inception in the model with changing orbital forcing. Additionally, due to uncertainties with respect to model biases, the initial ice sheet at 125 ka is not well constrained by reconstructions. Global sea level estimates range from 6 to 9 m sea level rise compared to pre-industrial times (Dutton et al., 2015; Rachmayani et al., 2017). It is assumed that Greenland contributed significantly to this relative sea level rise with estimates ranging from 0.6 mSLE to over 6 mSLE (Calov et al., 2015; Cuffey and Marshall, 2000; Robinson et al., 2011; Stone et al., 2013; Tarasov and Peltier, 2003; Yau et al., 2016). To which extent, however, remains unclear. To assess a lower bound in the phase space of the initial and final ice sheet volume of the experimental setups, a coupled experiment has been run with applied bias correction and an initial GIS representing around 3 mSLE, i.e., less than half the size of the pre-industrial GIS.

While large-scale glaciation occurred with the initial pre-industrial GIS, no inception occurred with the smaller initial GIS, indicating an important role of the initial ice sheet configuration. However, the question remains of how to initialize an ice sheet for a coupled model setup. A common method is to run the ice sheet into equilibrium. In contrast to the atmosphere, ice sheets are not in equilibrium in the real world due to their long response times.

Long response times might also play a role in the ocean dynamics under changing climate conditions in an accelerated couple setup like ours. Due to limitations in computing power, an acceleration of ten seems to be a reasonable choice. But ocean response times can be in the order of up to millennia. Hence, one can expect a lag in ocean response in the coupled model with respect to the faster-adapting atmosphere. Another drawback of the accelerated coupling is the neglection of mass conservation with respect to the freshwater stored in land-ice. In the setup, either correct freshwater fluxes are coupled or freshwater mass is conserved. Mass conservation would mean discharging all meltwater

from ten years of ice sheet melt into the ocean in only one year, producing ten times larger freshwater fluxes than meant to be. In the case of inception, it is the other way around, and the ocean loses only a tenth of the freshwater it would lose in a synchronous coupling. Hence, the effects of ice sheet growth on the ocean are underestimated due to 1) the high response times of the ocean that are not captured and 2) the underestimation of the total freshwater volume that enters or leaves the ocean. Furthermore, the ice sheet has less time to adapt to climatic changes than it would have in a one-on-one coupling, and hence ice mass loss during the GIS minimum at 122 ka might be larger when run synchronously. The timing of this minimum, however, seems to be robust, independent of the initial ice sheet state. The main driver seems to be the change in solar radiation by varying obliquity, as CO_2 concentrations do not decrease substantially before 115 ka.

The two mechanisms of gaining land ice are the positive climatic surface mass balance and lateral ice flow. The results of this chapter support the hypothesis that thickening snowfields are the starting point of inception as discussed by Andrews and Mahaffy (1976). Figures 5.8a and 5.8b show a transition from negative to positive surface mass balance over the Quebec region east of Hudson Bay. This relatively large area is fully glaciated by 115 ka. Ice flow, on the other hand, does contribute only little. However, the very first ice nuclei develop in high-elevation areas on Baffin Island and the Quebecian coast, but this initial ice nuclei formation is not sufficient for further large-scale glaciation as shown in the experiments 125^{PI} and $125^{125\mathrm{ka}}_{\mathrm{anom}}$.

This study includes an approach for the correction of atmospheric temperatures only. However, as mentioned above, sea surface temperatures commonly show warm biases in the North Atlantic region with implications for sea-ice cover and the regional climate. A correction of SST biases might therefore enhance the glaciation over North America and the development of ice shelves in Hudson Bay and Baffin Bay.

6. Interactive icebergs – closing a gap in ice sheet-ocean coupling

Icebergs play a crucial role in Earth's climate system. Their calving from Greenland and the Antarctic continent contributes significantly to the mass balances of the two ice sheets. For Greenland, approximately 550 Gt year^{-1}, representing a third to half of its freshwater release, is due to discharge (Enderlin et al., 2018). For Antarctica, values for iceberg discharge range from over 2,000 Gt year^{-1} (Jacobs et al., 1992) to more recent estimates of approximately 1,300 Gt year^{-1} (Depoorter et al., 2013). Icebergs transport large amounts of fresh water, alter ocean salinity and temperature, and hence affect deep-water and sea ice formation (Grosfeld et al., 2001; Stern et al., 2015). In regions of iceberg melting, the freshwater release leads to a freshening of the upper ocean, increasing the oceans' freezing temperature and enhancing stratification. Another direct effect is the cooling of the upper ocean layers by sensible and latent heat fluxes, increasing its density, and thus potentially decreasing stratification of the water column, which could counteract the effect of added freshwater. Despite their importance, icebergs are rarely represented in ESMs in detail, and, if accounted for, their effects on ocean conditions are often only parameterized (Devilliers et al., 2021). Freshwater fluxes from iceberg melting are distributed either homogeneously over a specific area or are treated as surface runoff, entering the ocean directly at coastal regions. The drawbacks of both methods are 1) the neglection of ocean dynamical effects on the icebergs and hence an unrealistic spatial distribution of freshwater release, 2) missing sensible and latent heat feedback from icebergs to the ocean and vice versa, and 3) neglecting iceberg size-dependent dynamics and impacts on the northward extent of the freshwater release and the associated cooling by giant icebergs (Rackow et al., 2017).

Early studies using global ocean models with implemented Lagrangian iceberg models showed a good representation of iceberg trajectories (Bigg et al., 1997; Gladstone et al., 2001). Later studies included interactive icebergs with heat

and freshwater feedback into fully coupled ESMs of varying complexity. Jongma et al. (2009) used an EMIC in a simulation with interactive icebergs. They found a decrease in sea ice concentration and associated warming in the Weddell Sea compared to a control run with freshwater homogeneously distributed over the Southern Ocean. Simulations using more advanced models with somewhat higher resolutions of 1° for the ocean component were done e.g. by Martin and Adcroft (2010) and Stern et al. (2016). In comparison to a simulation with iceberg freshwater fluxes parameterized as surface runoff, Martin and Adcroft (2010) found a freshwater export via icebergs from coastal regions resulting in positive salinity anomalies and enhanced deep convection. They also found a decreased sea ice cover. Using a more realistic size distribution, including larger km-scale icebergs, Stern et al. (2016) found a total decrease in sea ice concentration but cooling and freshening of the Weddell Sea. They argue to focus on large icebergs as these have the most significant effect on temperature and salinity changes. Rackow et al. (2017) add to this point by showing how the inclusion of even larger, giant icebergs impacts the meridional distribution of the iceberg meltwater input in their model simulations. Model simulations with even higher horizontal resolutions of about 0.25° were employed in ocean-only models (Marsh et al., 2015; Merino et al., 2016). They show the importance of icebergs for a realistic representation of Southern Ocean sea ice and its freshwater balance. However, heat fluxes from iceberg fusion were neglected.

So far, most studies have focused on surface conditions in the Southern Ocean. However, the effect of interactive icebergs on deep ocean water masses' characteristics has received less attention. This question seems especially important concerning the known deep ocean warm biases in models participating in CMIP (Rackow et al., 2019), which could affect long-term future and paleoclimate simulations e.g., by their ability to store heat in the abyssal ocean. Warm deep-ocean biases are common among complex Earth system models as found for FESOM by Streffing et al. (2022) and Sidorenko et al. (2019), and other climate models (Delworth et al., 2006; Delworth et al., 2012; Jungclaus et al., 2013; Sterl et al., 2012).

In this chapter, the contributions of iceberg freshwater and heat fluxes on deep ocean characteristics in a complex model are investigated for the first time. A fully coupled ESM with interactive icebergs is employed, using a resolution as high as approximately 1/3° in Southern Ocean coastal areas, with a size distribution representing present-day iceberg observations in the Southern Ocean.

The model used is the latest version of the AWI-ESM with an interactive Lagrangian iceberg model. The iceberg component runs as a submodel of the ocean–sea ice model FESOM2. In contrast to a previous version of this model introduced by Rackow et al. (2017), freshwater and heat fluxes are now interactive, providing a new level of coupled feedbacks. The initial position, number, and proportions of icebergs are derived from an ice-sheet model (ISM) output, allowing future applications in a coupled climate-ice sheet setup. The iceberg size distribution follows a -3/2 power law, derived from satellite observations for both open-ocean and near-coastal areas (Tournadre et al., 2016). The results are shown of multi-centennial simulations under pre-industrial forcing with the multi-resolution COREII ocean mesh.

6.1 Iceberg initialization and model setup

Icebergs are initialized from PISM output according to chapter 3. The PISM output provides a continuous calving and discharge field (Fig. 6.1) with the highest calving rates of up to 100 Gt year^{-1} along the Filchner-Ronne and the Ross ice shelves as well as in the Amundsen Sea, which corresponds well with observations (Depoorter et al., 2013). The icebergs are initialized according to chapter 3.5 with a quadratic surface and a height, being as large as the side length but 250 m at maximum. Following Tournadre et al. (2016), individual iceberg areas are drawn from a power-law distribution with a slope of -1.52. The initial size distribution is shown in Fig. 6.1b, with the vast majority of icebergs being rather small (0.1-1 km^2) and only a few being larger than 100 km^2. A maximum iceberg area of 400 km^2 is assumed in order to avoid iceberg areas being larger than an ocean grid cell. Scaling factors are applied according to Supplement D. The total calving flux of roughly 1,731 Gt year^{-1} is subtracted from the surface runoff to ensure a closed water balance (Fig. 6.1c). To spin up the iceberg model, an equilibrated pre-industrial run has been continued with icebergs but with freshwater and heat feedback turned off ($\mathrm{ICB_{spinup}}$). This spinup has been run for 100 years, after which the total iceberg melt flux balances the calving flux (Fig. 6.1c). Several experiments were branched off from this spinup, a fully coupled run with icebergs (ICB), two partially coupled iceberg runs, one without latent heat fluxes from iceberg fusion ($\mathrm{ICB_{FW}}$), and one without iceberg meltwater feedback ($\mathrm{ICB_{HF}}$), respectively. The same iceberg setup has been used for these runs. Additionally, a control run without icebergs (CTL) has been run. Table 6.1 summarizes all experiments.

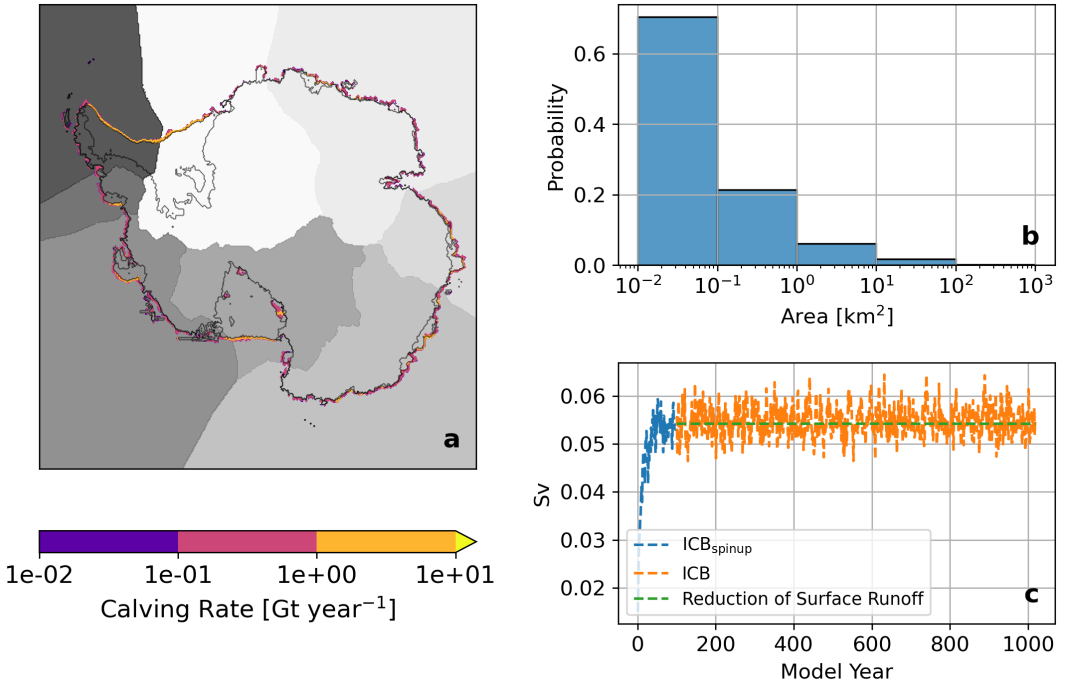

FIGURE 6.1: a) Calving flux from a PISM standalone simulation. The grey-shaded areas depict different basins where the calving rate is integrated to generate icebergs; b) size distribution of seeded icebergs; c) iceberg-related freshwater flux for spinup and ICB, and the reduction of Antarctica's surface runoff.

6.2 Iceberg trajectories

Figure 6.2a illustrates iceberg trajectories for the fully coupled iceberg run ICB. Two main pathways can be recognized: one branching off the Antarctic peninsula, where small and large icebergs follow the Antarctic Circumpolar Current, and one pathway in the Ross Sea with medium-sized icebergs. Large icebergs tend to stay along the coast, following the Antarctic Coastal Current. The general patterns resemble satellite observations for giant icebergs by Budge and Long (2018) and Stuart and Long (2011) (Fig. 6.2d). However, model icebergs travel further north compared to observations. In the Ross Sea, their pathways are confined by the Antarctic Convergence Zone (indicated as the zone between the 2°C and 5°C SSTisotherms). The spatial patterns of freshwater and heat fluxes (Fig. 6.2b and c) match the trajectories and show melting hot spots near the coast, inside the Weddell Sea, and at the tip of the Antarctic peninsula where, very locally, freshwater and heat fluxes of over 10 m year^{-1} and 10 Wm^{-2}, respectively, are reached.

TABLE 6.1: Experiments run within the scope of this study. *EXP. ID* indicates the name used for this experiment throughout this chapter; *icb cpl.* indicates whether icebergs are not coupled, only partially coupled (either heat fluxes or freshwater fluxes) or fully coupled (heat fluxes plus freshwater fluxes) or are turned off; *cpl. frequency* indicates the coupling frequency (see ch. 3); *run length* indicate the length of the simulation.

EXP. ID	icb cpl.	scaling	cpl. frequency	run length
ICB_{spinup}	not coupled	yes	8	100
CTL	no	-	-	700
ICB	fully coupled	yes	8	700
ICB_{FW}	only fresh water	yes	8	700
ICB_{HF}	only heat flux	yes	8	700

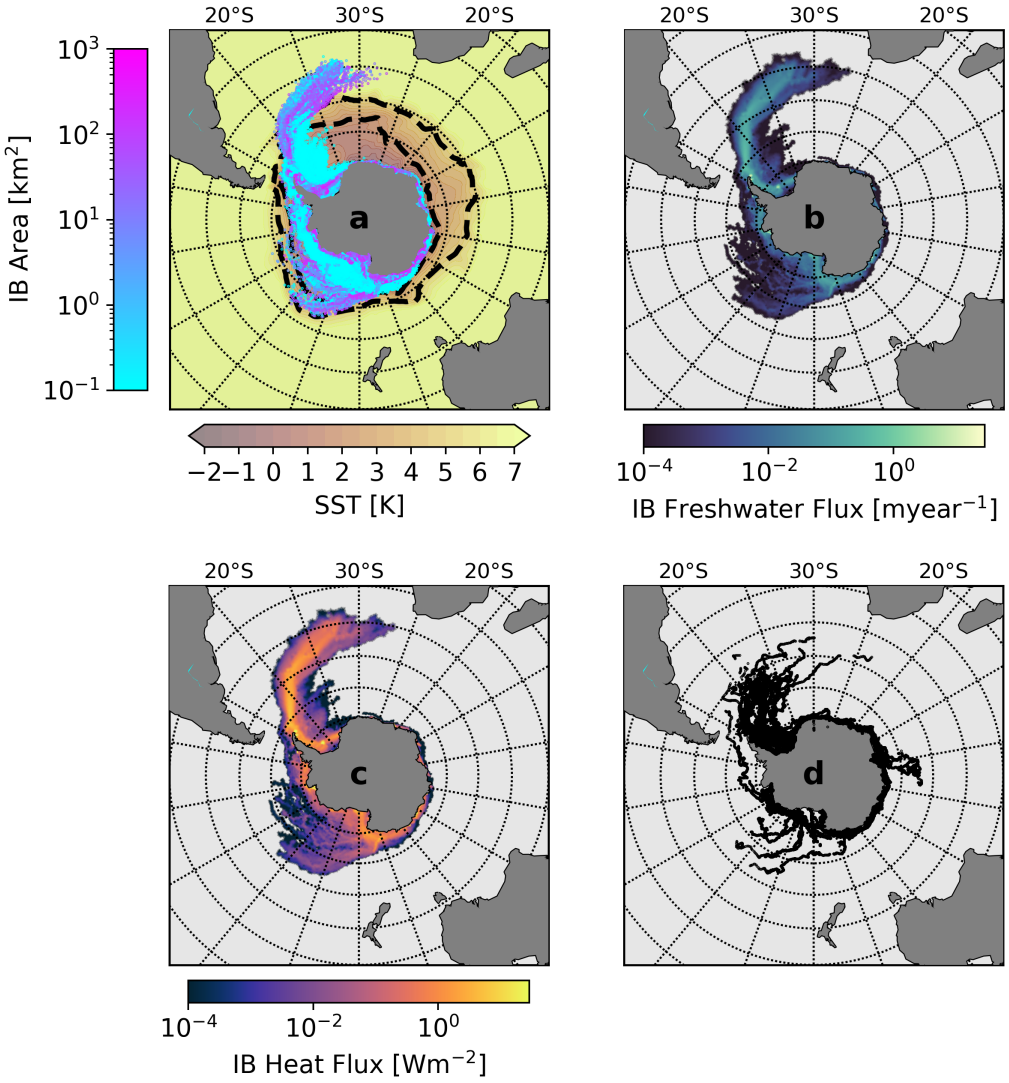

FIGURE 6.2: a) Sea Surface Temperature overlaid by iceberg trajectories with iceberg surface area shown on a logarithmic colorbar. The black dashed contour lines indicate the Antarctic Convergence Zone where SST falls from 5°C to 2°C; b) freshwater flux due to iceberg melting; c) heat flux due to iceberg melting; d) satellite observations from the QuikSCAT portion of the Antarctic Iceberg Tracking Database (Budge and Long, 2018; Stuart and Long, 2011) over the period from 1991 to 2022. All model results are averaged over model years 600-700.

6.3 Surface conditions

The anomalies for sea surface salinity (SSS), sea surface temperature (SST), and sea ice height are shown in Fig. 6.3 for ICB, ICB_{HF}, ICB_{FW}, and CTL with respect to the spinup. ICB, ICB_{HF}, and ICB_{FW} show pronounced positive salinity anomalies in the shelf regions of the Weddell Sea (Fig. 6.3a and g). A similar salinity anomaly is detected in the Ross Sea sector in ICB_{HF}. However, the underlying dynamics are fundamentally different. In ICB and ICB_{FW}, the surface runoff is most reduced compared to CTL, in areas that correspond to the coastal regions with the highest calving rates. In these areas, freshwater by iceberg calving is parameterized via the river routing scheme and eventually treated as river discharge in CTL and ICB_{HF}. As the icebergs do not melt entirely in their regions of origin but rather further north off the coast, the model experiences a relative freshwater export from near-coast shelf regions, which results in pronounced positive salinity anomalies in the shelf regions of the Weddell Sea in ICB and ICB_{FW}. In contrast, in ICB_{HF} (in which the surface runoff is not altered compared to CTL), enhanced sea ice formation (Fig. 6.3i) leads to increased brine rejection. This can be recognized in the Weddell Sea shelf region and the Ross Sea. These regions of positive salinity anomaly match well to the pattern of increased sea ice height for ICB_{HF} (Fig. 6.3g and i). In contrast, no systematic increase in sea ice height can be recognized in this region in ICB and ICB_{FW} (Fig. 6.3c and f). Here, the increased salinity due to reduced near-coastal freshwater surface runoff inhibits additional sea ice growth. But sea ice growth is fostered in coastal regions of the Amundsen and Bellinghausen Seas, along the Antarctic Peninsula, and along the Wilkes Land coast (Fig. 6.3c). Here, freshwater and heat fluxes from iceberg melting are very high (Fig. 6.2b and c). Cooling patterns can be seen in the Weddell Sea and the Indian sector of the Southern Ocean (Fig. 6.3b and h), while warming is detected in the Amundsen and Bellinghausen Seas, as well as in the Ross Sea, leading to a dipole of warm/cold anomalies across the Antarctic Peninsula. The warming in the Amundsen and Bellinghausen Seas is linked to an increase in surface salinity that leads to enhanced vertical mixing and upward mixing of heat. In contrast to the similar cooling patterns in ICB and ICB_{HF}, a warming in the Weddell Sea can be recognized in ICB_{FW} (Fig. 6.3e). In this experiment, an increase in salinity also leads to enhanced vertical mixing and convective mixing of heat as in ICB and ICB_{HF}, but latent cooling from iceberg melting is missing to compensate for this surface warming. In general, the resulting responses for SST, SSS as well as sea ice height are dominated by the effects

of heat and freshwater fluxes in ICB, revealing minor importance of synergetic effects on long time scales.

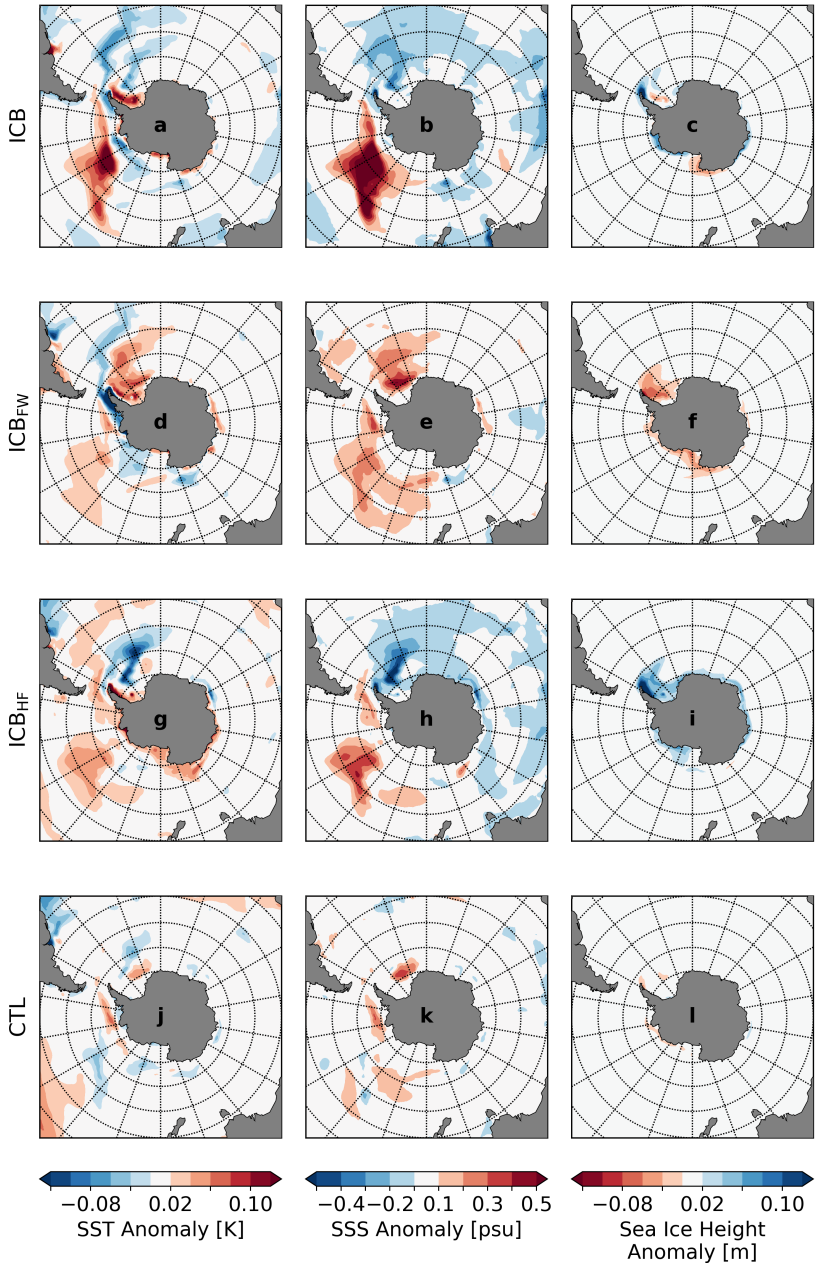

FIGURE 6.3: Anomalies of SSS, SST, and sea ice height for the experiments ICB (a-c), ICB$_{FW}$ (d-f), ICB$_{HF}$ (g-i), and CTL (j-l). All results are averaged over model years 600-700 and anomalies are calculated with respect to the spinup.

6.4 Deep ocean conditions

Changes in deep ocean temperature for the Atlantic, Pacific, and Indian Ocean basins are illustrated in Fig. 6.4. After 700 model years, a cooling in all three basins can be seen for ICB and ICB_{HF} with respect to the spinup run. The cooling of up to -0.2 K is most pronounced in the Pacific (Fig. 6.4b and h). While no cooling is recognizable in ICB_{FW}, the patterns of ICB and ICB_{HF} look very similar. The cooling signal extends from the surface layers of the Southern Ocean's Atlantic section (Fig. 6.4a and g) to the deep southern mid-latitudes. A cold cell can be seen in the North Atlantic at around 1,000 m depth. The deep North Atlantic as well as the Arctic Ocean, show a warming trend. However, this is partly due to a general background trend and internal model variability as it is also visible for the control run (Fig. 6.4j). In contrast to the Atlantic basin, the cooling in the Pacific and Indian Oceans extends over the whole basins (Fig. 6.4b, c, h and i). Most pronounced in the Southern Ocean, it spreads more northward with depth. However, the upper ocean layers show a warming in the high latitudinal Pacific section of the Southern Ocean, corresponding to the warming of the Ross Sea (Fig. 6.3a, d, g). This effect is also visible in ICB_{FW}. Also here, CTL shows a slight warming (Fig. 6.4k), but to a much smaller magnitude than the other simulations.

A strong increase in salinity can be seen in ICB and ICB_{HF} in the Atlantic and Pacific sectors from the surface to a depth of around 500 m (Fig. 6.5a,b and g,h). These salinity anomalies are mainly detected in the shelf regions of the Weddell and Ross Seas, indicating a link to the surface conditions (SSS anomalies in Fig. 6.3). However, ICB_{FW} also shows positive SSS anomalies, especially in the Weddell Sea but the vertical extension is limited to mixed layer depths (Fig. 6.5d). The main driver for the positive salinity anomalies reaching deeper levels is therefore attributed to the latent heat flux from iceberg melting. The effect of altered spatial freshwater distribution, on the other hand, plays a minor role.

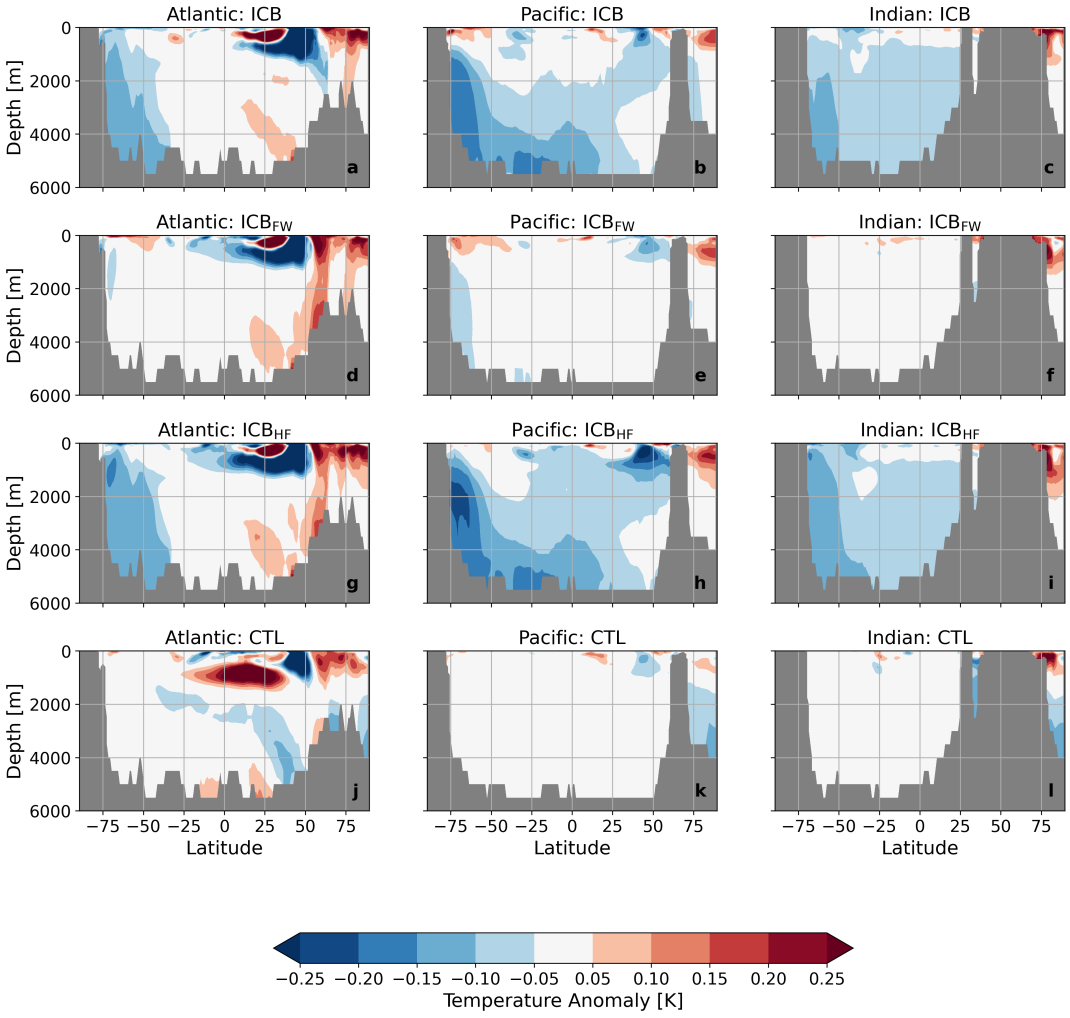

FIGURE 6.4: a-c: Temperature anomalies for the Atlantic, Pacific, and Indian Ocean, respectively for ICB; d-f: Temperature anomalies for ICB_{FW}; g-i: Temperature anomalies for ICB_{HF}; j-l: Temperature anomalies for CTL. All results are averaged over model years 600-700 and anomalies are calculated with respect to the spinup.

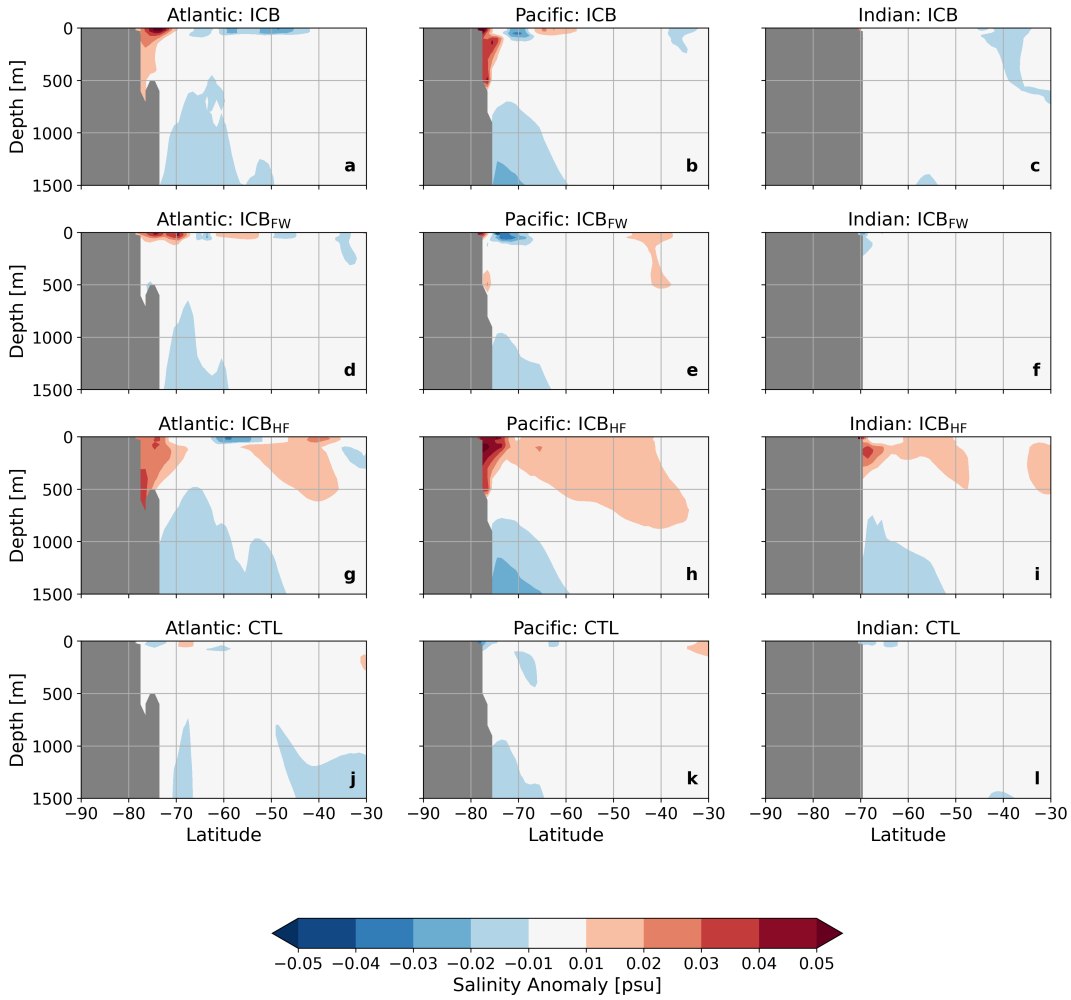

FIGURE 6.5: a-c: Salinity anomalies for the upper 1,500 m of the Atlantic, Pacific, and Indian Ocean sections of the Southern Ocean for ICB; d-f: Salinity anomalies for ICB_{FW}; g-i: Salinity anomalies for ICB_{HF}; j-l: Salinity anomalies for CTL. All results are averaged over model years 600-700 and anomalies are calculated with respect to the spinup.

6.5 Impact on adjustment time-scales

The effect of temperature changes on seawater density is small compared to the effects of salinity in the experiments. The salinity increase leads to a positive density anomaly, and hence to a weakening of vertical stratification. This weakening is especially pronounced over the continental shelf in the Ross Sea in ICB and ICB_{HF}, and additionally along the coast of Wilkes Land in ICB_{HF} (Fig. 6.6). ICB_{FW} shows a strengthening of stratification around Antarctica except for the Weddell Sea. This weakened vertical stratification in the Southern Ocean results in enhanced deep convection over continental shelves and enhanced formation of AABW (Fig. 6.7). The AABW in the Indo-Pacific sector (AABW-IP) is increased by up to 10 % in ICB and ICB_{HF}. The AABW-IP strengthening occurs within the first 200 model years and stays at a rather constant level afterward. ICB_{FW} and CTL show a weak trend. As changes in AABW formation in the Atlantic sector only represent a minor contribution, global AABW mainly follows the AABW-IP signature originating in the Ross Sea self-region as the main area, which is affected by destabilized stratification due to iceberg heat fluxes. The global ocean temperature decreases by approximately 0.01 K per century over the first 400 years in ICB and ICB_{HF}. This corresponds with a rough calculation considering the enthalpy of fusion for a discharge flux of around 1,700 Gt per year. After 400 years, the cooling trend in ICB flattens while it continues to decrease in ICB_{HF}. The altered freshwater distribution via iceberg transport hence buffers the cooling. No cooling trend is recognizable in CTL and ICB_{FW}.

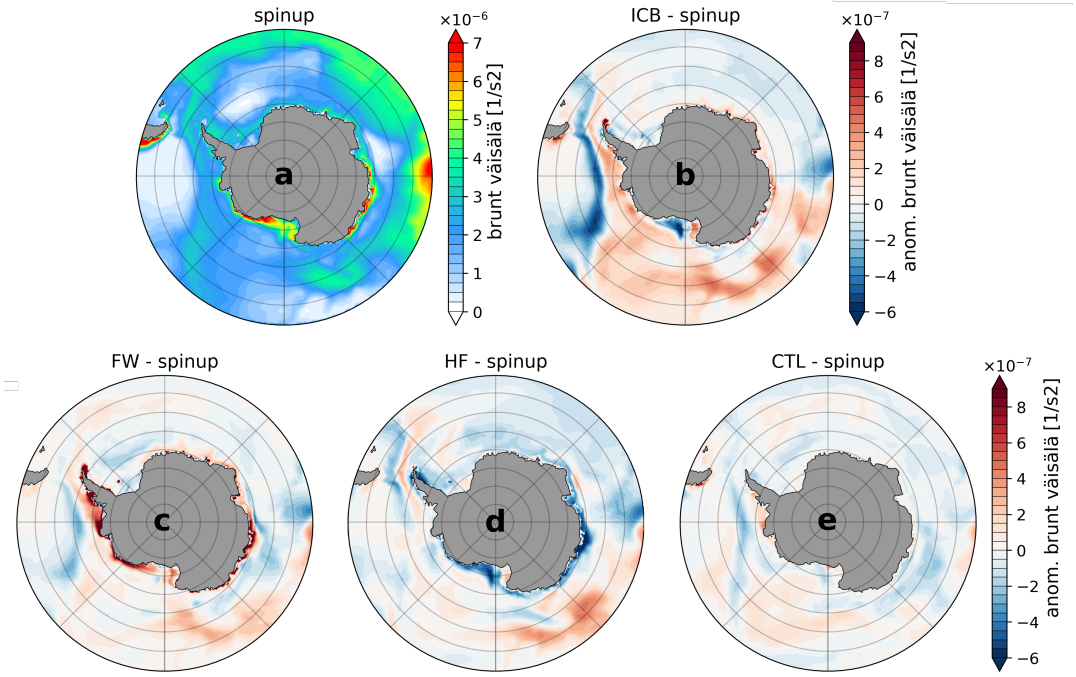

FIGURE 6.6: Brunt Väisälä frequency for spinup (a) and anomalies for ICB (b), ICB_{HF} (c), ICB_{FW} (d), and CTL (d) with respect to spinup, averaged over the upper 250 m and for the model years 600-700.

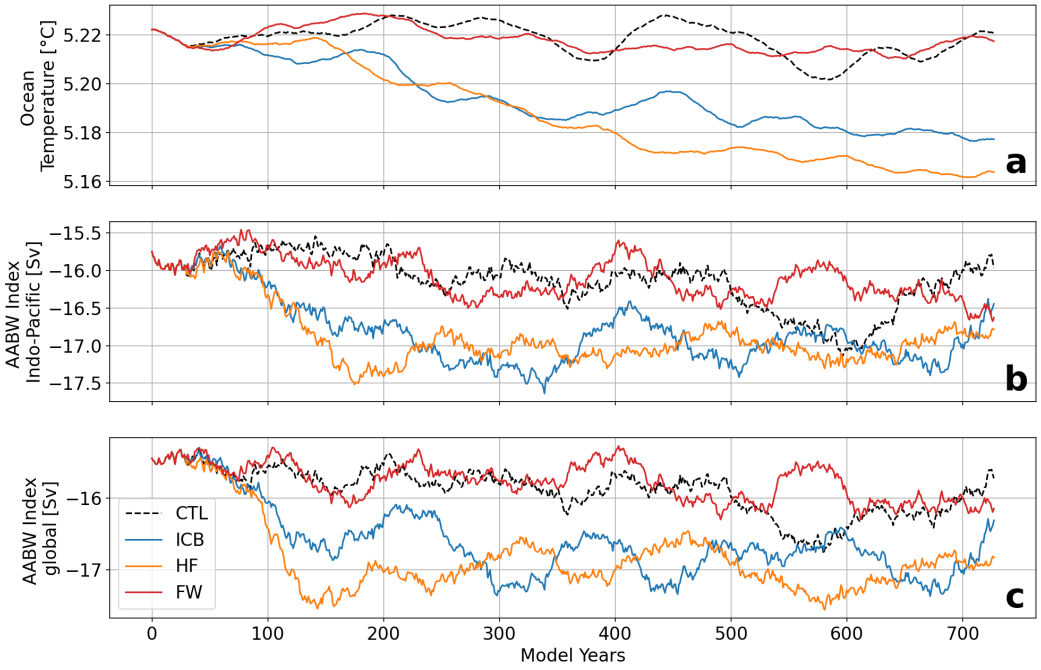

FIGURE 6.7: Time series for global ocean mean temperature (a), AABW in the Indo-Pacific basin (b), and globally (c) as the 50 year rolling mean of the maximum stream function value at 30°S.

6.6 Discussion of the interactive icebergs

Multi-centennial simulations with a complex fully-coupled ESM, including interactive icebergs, have been run. While the iceberg trajectories show generally good agreement with observations, there are also some discrepancies. No icebergs are branching off near the Kerguelen Plateau in the simulations as seen in observations (Fig. 6.2) or as found by Rackow et al. (2017) in their ocean-only simulations with prescribed atmospheric forcing. This might be due to the coarse resolution of the atmosphere and land surface. Steep orographic gradients are smoothed out, which hinders the formation of katabatic winds. Instead, icebergs are mainly affected by polar easterlies and hence pushed onshore due to geostrophic balance. In general, large model icebergs tend to be too confined to coastal regions. This was already found by Rackow et al. (2017), and other studies (Merino et al., 2016). When being able to leave the coast, the icebergs show a drift further north in the simulations than in observations but do not travel as long distances as in Rackow et al. (2017). However, the observational data used here only covers icebergs larger than ∼5-6 km (Stuart and Long, 2011) and hence can miss substantial parts of the end of giant icebergs' trajectories.

Although giant icebergs up to a side length of 20 km are included in this study, a suitable break-up parametrization is missing, as well as physical feedbacks besides freshwater and heat fluxes. These feedbacks may include effects on surface albedo, surface wind stress, and sea surface height. As the dynamics of small and large icebergs differ (Rackow et al., 2017), a break-up parametrization would affect trajectories and melt patterns (England et al., 2020). Furthermore, a uniform calving size distribution for all ocean basins has been employed. However, size distributions vary at different locations, and giant icebergs calve very rarely. Hence, they should be treated as statistically rare events similar to volcanic eruptions, for example, by calving them stochastically in ensemble simulations or by prescribing their time-mean effects via pre-computed melt climatologies (Rackow et al., 2017; Stern et al., 2016).

The effects on sea surface conditions support the findings of previous studies. Martin and Adcroft (2010) and Stern et al. (2016) also found warming in the Amundsen and Bellingshausen Seas as well as in the Ross Sea. This warming is explained by increased upward heat transport due to a destabilization of the upper ocean layer's stratification. This weakened stratification stems from increased salinity due to northward freshwater export.

In the ICB and ICB_{FW} experiments, the surface runoff is reduced by the amount of iceberg discharge. Together with the brine rejection by increased sea ice formation, this leads to a salinity increase, particularly in the Weddell Sea shelf region. The westward drift of near-coastal icebergs and the associated freshwater export by the Antarctic Coastal Current plays an additional role in the Ross Sea.

However, the simulation ICB_{HF} also shows a strong increase in salinity despite unaltered surface runoff. Hence, increased sea ice formation and duration also play an important role in Ross Sea's freshwater budget. The latent heat fluxes associated with iceberg melt even seem to play a dominant role in salinity changes up to intermediate depths and the formation of deep water (Fig. 6.5). Furthermore, they lead to surface cooling in the Weddell Sea (Fig. 6.3b and h), which is also found by Stern et al. (2016). The altered spatial freshwater distribution alone leads to a warming of large areas of the Southern Ocean's surface and subsurface waters (Fig. 6.3d) and thus buffers the cooling effect of iceberg melt. The iceberg-related heat fluxes are necessary to compensate for the surface warming and sustain the anomalous vertical heat transport.

A strengthening of AABW by up to 10% agrees well with findings by Jongma et al. (2009) and Martin and Adcroft (2010). ICB and ICB_{HF} show similar strengthening of AABW-IP, and the most pronounced weakening of stratification in the Ross Shelf region, indicating the importance of the latent heat effect. Deep water formation along continental shelves is a process commonly underestimated in CMIP6 models, whereas open-water deep convection is highly overestimated (Heuzé, 2021). Though a realistic representation of AABW formation along continental shelves is not feasible in the model setup, the results aid to tackle this issue and emphasize the added value of a realistic representation of iceberg-related heat and freshwater fluxes in the Southern Ocean.

The results show a cooling of deep water masses in model runs with interactive icebergs. A pronounced cooling of the global deep ocean is recognized after around 200 years. The experiment that only considers heat fluxes from iceberg melting while using the default parameterized freshwater fluxes shows similar results as the fully coupled one, including the iceberg-related meltwater. This result is not surprising as the same heat flux is applied to both simulations, leading to monotonous cooling. This cooling may aid in reducing deep-ocean temperature biases (see supplement E) as found for FESOM2 (Streffing et al., 2022; Sidorenko et al., 2019), and other climate models (e.g. Delworth et al.

(2006), Delworth et al. (2012), Jungclaus et al. (2013), Rackow et al. (2019), and Sterl et al. (2012)).

In this chapter, the effect of interactive icebergs on the surface and in particular deep ocean water mass changes were investigated. For this, a fully coupled ESM has been used with higher resolution (up to $\sim 1/3°$) at continental shelf regions around Antarctica together with an interactive Lagrangian iceberg model (Rackow et al., 2017). Deep ocean temperatures are reduced in all ocean basins. Originating in the upper layers of the Southern Ocean, the cooling effect propagates northward. The results suggest that the latent heat flux from iceberg melting is the main driver for this large-scale cooling. Furthermore, the results show an increased salinity on the continental shelves around Antarctica due to northward freshwater export by northward-drifting icebergs. This results in enhanced deep water formation along continental shelves, which is a process commonly underestimated by CMIP6 models that do not include a sophisticated treatment of iceberg-related meltwater and heat fluxes. Hence these results emphasize the importance of realistically representing iceberg-related heat and freshwater fluxes in the high southern latitudes.

7. Final considerations

7.1 Conclusions

In this study, which has been conducted within the scope of the second phase of the PalMod project, climate-cryosphere interactions are investigated with the comprehensive Earth system model AWI-ESM. Study periods cover future warming scenarios, the pre-industrial time, and the cooling interval of the LGI. The transient future and inception runs were performed with an interactive ice sheet model coupled with the climate components. The pre-industrial time slice experiment employs an interactive iceberg model, and while there is no interactive ice sheet, icebergs are seeded from a previously run ice sheet model simulation. Different aspects of the climate-cryosphere interactions were examined, and concise answers to the research questions that were addressed in the chapters 4, 5, and 6 are given in the following.

1. **What is the effect of an interactive Greenland Ice Sheet on freshwater discharge in a complex coupled Earth system model?** (Chapter 4) The interactive ice sheet model adds a strong decadal variability to the surface runoff compared to simulations without an interactive ice sheet, which is in accordance with reconstructions (King et al., 2018; Trusel et al., 2018). The implemented ice sheet model allows for a highly-resolved spatial freshwater distribution. The discharge maxima in West Greenland are in accordance with reconstructions and satellite measurements of past decades (Team, 2020; Mouginot et al., 2019). Furthermore, the ice sheet model adds a buffer effect that potentially decreases surface runoff during times of ice sheet growth. However, the effect on AMOC slowdown and recovery is little compared to the effect of the forcing applied. The AMOC slows down throughout the 21st century in the performed future warming scenario simulations but eventually starts to recover. The main driver for this recovery is enhanced atmospheric freshwater transport. Another potential reason for the weak climatic response to the interactive ice sheet is the GIS related freshwater input not reaching

the regions of deep-water formation.

2. **Is the model able to initiate large-scale glaciation in a coupled transient simulation?** (Chapter 5)
   In a transient simulation with an asynchronously coupled interactive ice sheet model covering the Northern Hemisphere, large-scale glaciation of the North American continent occurred. The timing as well as the spatial extent of ice sheet development fit in the range of uncertainty of reconstructions by proxy data. A pre-industrial ice sheet state has been coupled to an equilibrated climate state for the 125 ka time slice. This provides an upper bound for the initial ice sheet volume as reconstructions suggest reduced GIS at this time compared to the pre-industrial. The main driving force in the simulation is the solar radiation at high northern latitudes that is primarily modulated by obliquity. However, the climate model shows a warm bias of several degrees Celsius in the area around Hudson Bay. Only when this bias is accounted for and is corrected by an anomaly coupling ice-sheet buildup occurred in the coupled model setup. Initial ice sheet nuclei developed in all simulations (with and without anomaly coupling) at high-elevation regions on the Quebecian coast and on Baffing Island. This development can also be seen in the control simulation with pre-industrial climate. However, only the bias-corrected simulation with transient cooling grows ice to an extent that fully covers Baffin Island and larger areas of Quebec. This spatially extended inception in the simulation was driven by snowfield thickening, while internal ice sheet dynamics played only a minor role. Therefore, the development of ice nuclei seems not sufficient for further ice sheet growth. This emphasizes the importance of a realistic climatic base state.

3. **What are the effects of interactive icebergs on deep ocean water characteristics on long-time scales?** (Chapter 6) Time slice experiments under pre-industrial climate forcing with interactive icebergs show enhanced AABW formation and deep-ocean cooling on multi-centennial time scales.

   A common method to account for iceberg discharge in Earth system models is to distribute the freshwater fluxes either along the coastline via river discharge or to distribute it homogeneously over a specific area. This leads to freshwater biases over the continental shelf regions of Antarctica. Furthermore, latent heat fluxes due to iceberg melting are often neglected.

   The simulations presented here show two-fold effects of interactive icebergs: the spatial redistribution of freshwater input leads to more saline water conditions at the Ross Sea's and Weddel Sea's shelf regions. This effect, however, is limited to the upper mixed layer. The more dominant effect is the cooling due to the latent heat of iceberg melting at the surface. This cooling can be seen over large parts of the Southern Ocean except for the Amundsen-Bellinghausen Seas. The cooling facilitates sea-ice formation and increased brine rejection, eventually weakening the oceans' stratification of Antarcticas continental shelf regions. This leads to enhanced deep water formation along continental shelves, which is a process commonly underestimated by CMIP6 models. This effect is most pronounced in the Ross Sea. Consequently, the increase in global AABW formation can be mainly attributed to the Pacific sector. The deep-ocean cooling originates in the upper layers of the Southern Ocean. It propagates northward in all ocean basins, most pronounced in the Pacific basin and limited to higher southern latitudes in the Atlantic basin. As current climate models commonly show too warm deep ocean conditions, the implementation of interactive icebergs is a promising step towards a comprehensive, less biased Earth system model. The more realistic representation of Southern Oceans' freshwater, heat, and sea ice conditions can have implications for the stability of ice shelves and ice sheets. Therefore, the newly enhanced model is a good candidate for future sea level projections and for paleoclimate simulations covering time slices with high ice sheet dynamics.

7.2 Outlook

The different cryosphere components examined in this study, ice sheets and icebergs, will be brought together in a next model version. The coupling routine presented in chapter 3 for deriving distinct icebergs from ice sheet model output is already implemented within the ESM-tools (Barbi et al., 2021) and can be run in a fully coupled climate-ice sheet model setup. In this way, the total iceberg discharge volume can be adapted to the transient ice sheet output. This implementation would be a logical next step towards a fully comprehensive Earth system model. Such a model would allow for a more realistic representation of periods with highly dynamic cryosphere components like Heinrich events or future warming scenarios. Although not presented in this study, the iceberg model allows for a dual-hemisphere setup already. For the coupled climate-ice sheet model, a dual-hemisphere setup has been developed recently. This model setup allows for the investigation of inter-hemispheric teleconnections with respect to climate-cryosphere dynamics. For instance, variations in AMOC strength during the Pleistocene can be linked to Southern Ocean surface conditions (Knorr and Lohmann, 2003). It is thought that the transport of buoyancy anomalies from the Indian Ocean to the South Atlantic via the Agulhas Leakage plays an important role in this teleconnection (Caley et al., 2012; Marino et al., 2013). One potential source of these buoyancy anomalies is the perturbation of the freshwater balance, e.g. by icebergs. Records of ice-rafted debris (IRD) suggest the occurrence of far-traveling icebergs of Southern Ocean origin at the Agulhas Plateau during Pleistocene glacial conditions. Their melt-induced freshwater release affects the Atlantic freshwater import with implications for the AMOC. Peaks in the IRD were found to precede AMOC slowdowns on a millennial time scale (Starr et al., 2021). In the Northern Hemisphere, on the other hand, IRD suggests the discharge of vast amounts of icebergs during late Pleistocene glacials (Bond et al., 1992; Broecker et al., 1992; Heinrich, 1988). Heinrich events can be linked to abrupt climate shifts and associated changes in AMOC strength (McManus et al., 2004). Studies of sediment data (Barker et al., 2015; Marcott et al., 2011) and model studies (Alvarez-Solas et al., 2013; Shaffer et al., 2004) indicate that iceberg discharge did not trigger AMOC slowdown but occurred rather as a consequence of North Atlantic subsurface warming. These warmings occurred during phases of a weak AMOC, which may have been further enhanced by iceberg discharge.

Furthermore, the third phase of the PalMod project is dedicated to the production of multi-millennial future simulations. These simulations shall be performed with different greenhouse gas forcing scenarios to assess the long-term changes of ice sheets and their implications on global sea level. Concurrently, model development shall continue with the aim to develop an ESM that includes climate and cryosphere components as well as an interactive carbon cycle to avoid the necessity of prescribing greenhouse gas concentrations as external forcing. An interactive carbon cycle would allow to assess the effects of anthropogenic carbon emissions on multi-millennial time scales.

A. Basal melting Greenland Ice Sheet

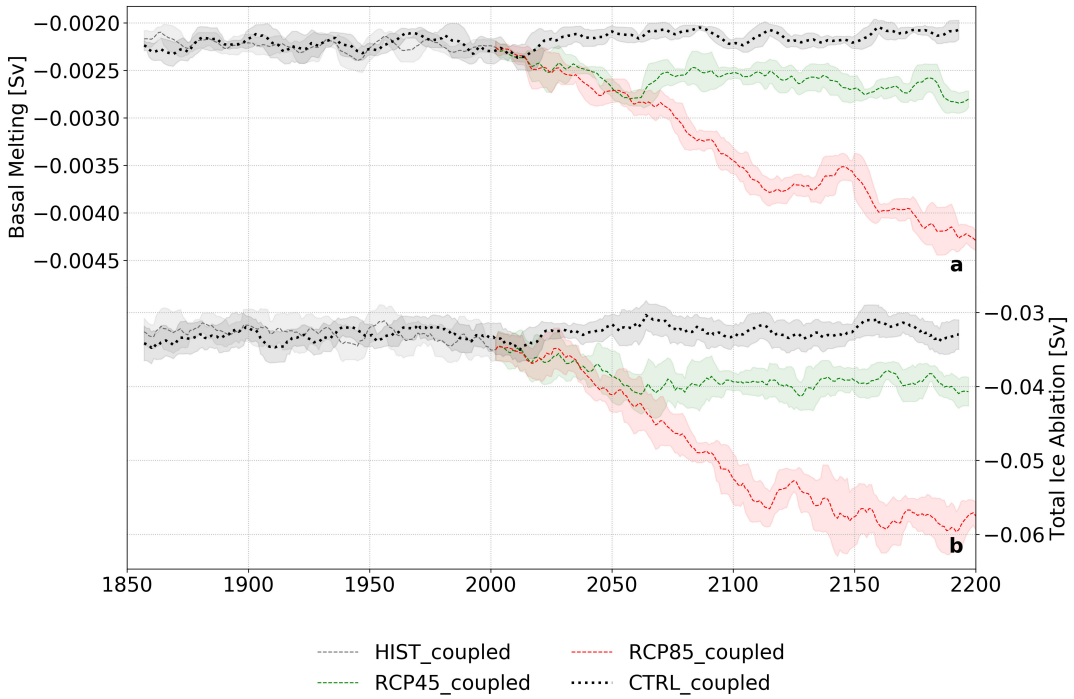

FIGURE A.1: Timeseries of 11-year mean for a) basal melting, b) total ablation as sum of runoff and discharge for the Greenland Ice Sheet for different future warming scenarios run with AWI-ESM.

B. Tendency of ice mass due to flow

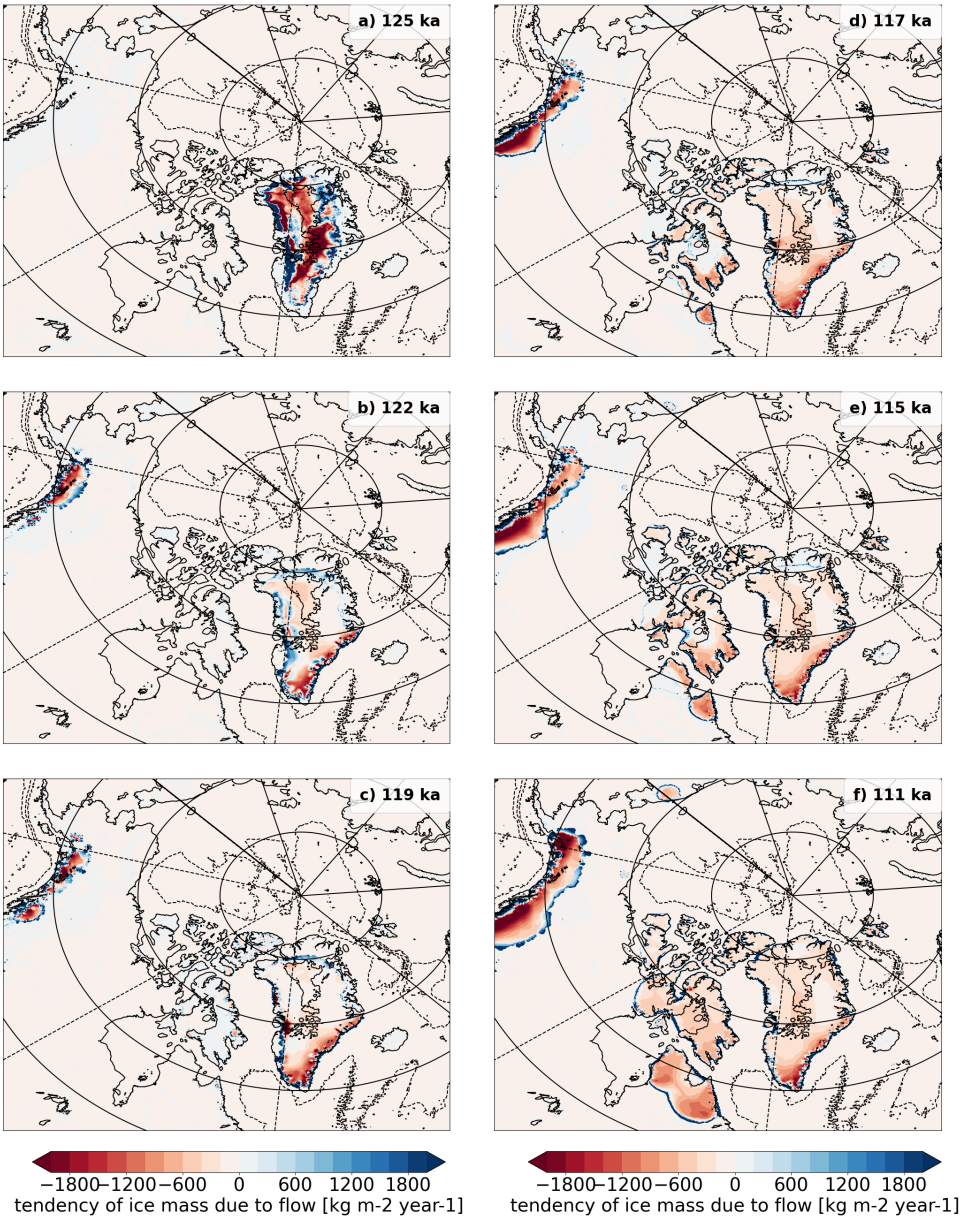

FIGURE B.1: Tendency of ice amount due to flow for time slices 125 ka, 122 ka, 119 ka, 117 ka, 115k ka, and 111 ka for $125^{\mathrm{PI}}_{\mathrm{anom}}$.

C. Tendency of ice mass

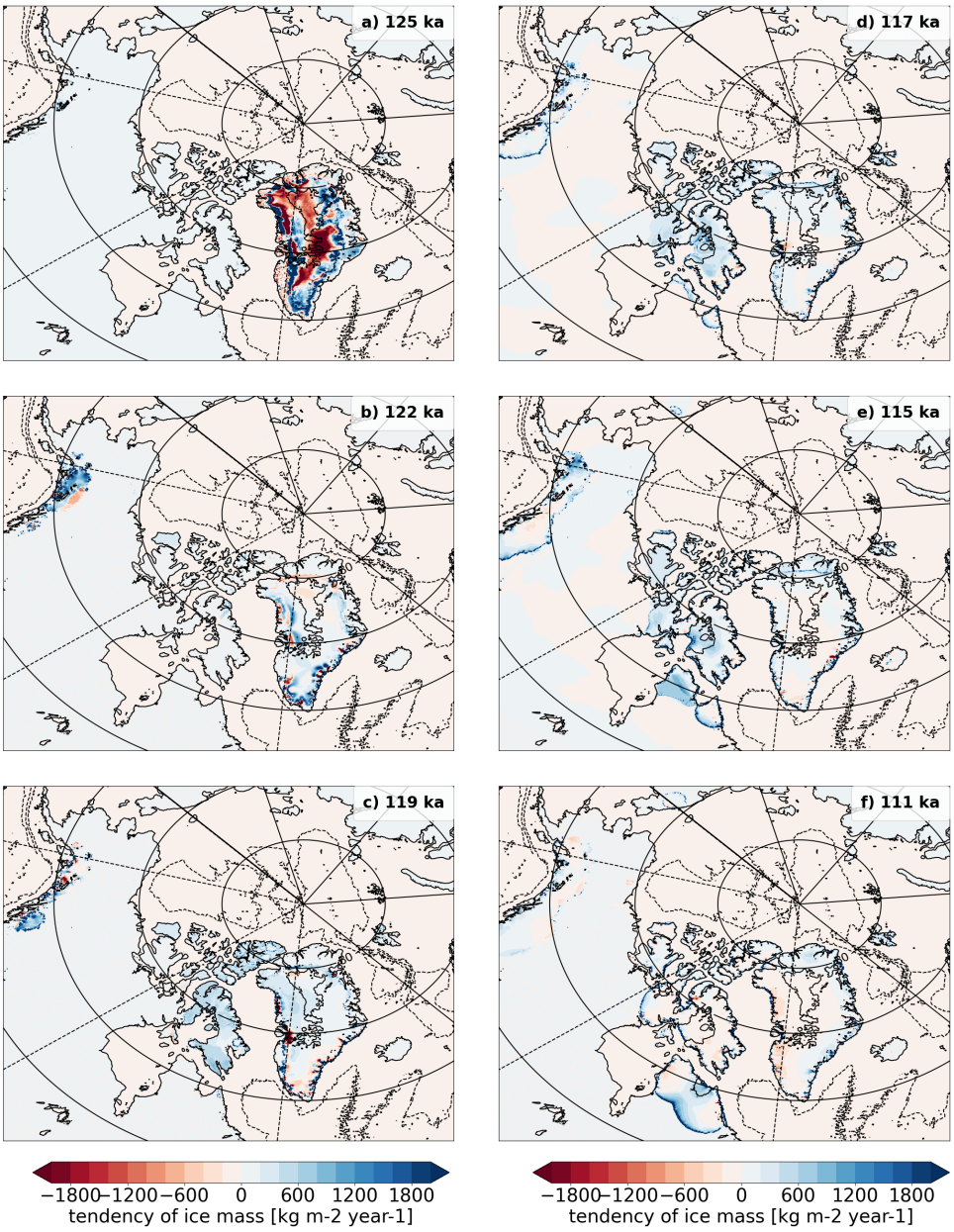

FIGURE C.1: Tendency of ice amount for time slices 125 ka, 122 ka, 119 ka, 117 ka, 115k ka, and 111 ka for $125^{\mathrm{PI}}_{\mathrm{anom}}$.

D. Scaling factors for different iceberg size classes

TABLE D.1: Scaling factors for iceberg experiments performed in chapter 6

Area A [km^2]	Scaling factor
$A <= 0.1$	100
$0.1 < A <= 1$	50
$1 < A <= 10$	10
$10 < A <= 100$	1
$100 < A <= 1,000$	1
$A > 1,000$	1

E. Temperature biases for different ocean basins

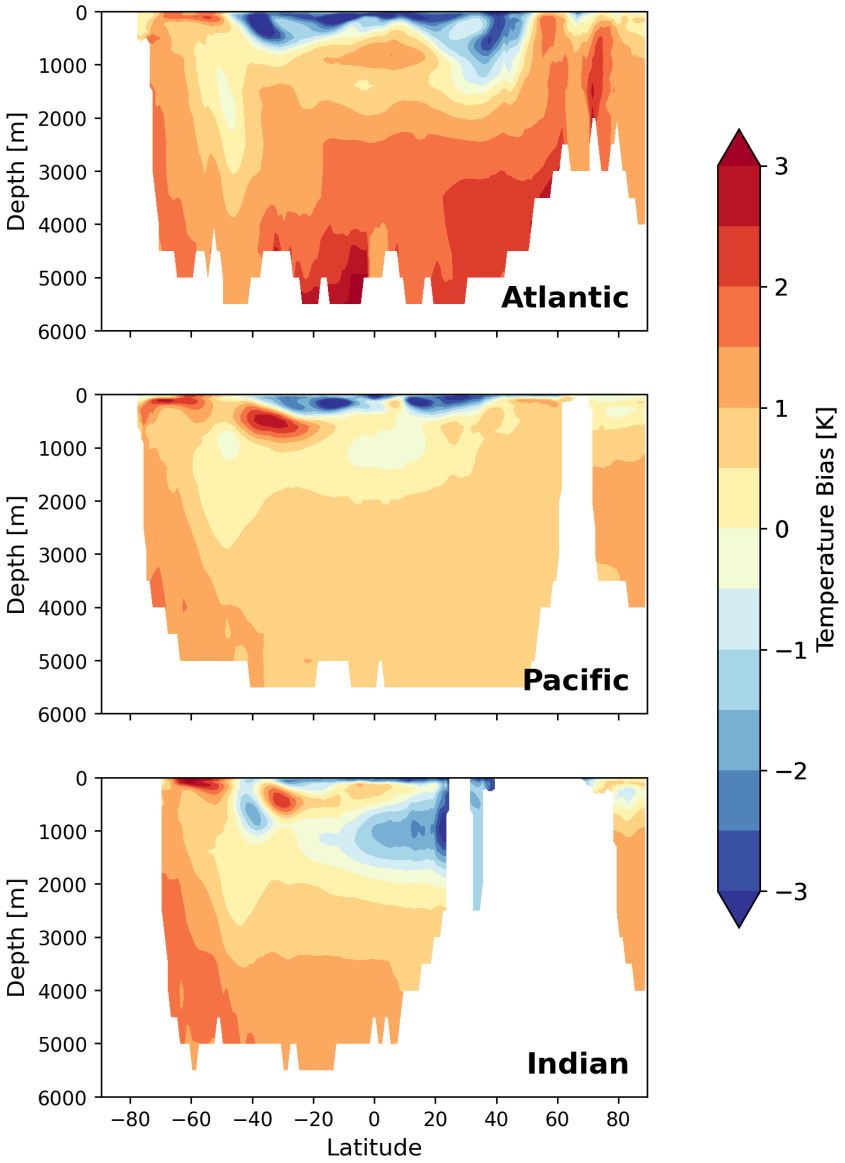

FIGURE E.1: Temperature biases for different ocean basins with AWI-ESM.

Bibliography

Ackermann, L., C. Danek, P. Gierz, and G. Lohmann (2020). "AMOC Recovery in a multicentennial scenario using a coupled atmosphere-ocean-ice sheet model". In: *Geophysical Research Letters* 47.16.

Alvarez-Solas, J., A. Robinson, M. Montoya, and C. Ritz (2013). "Iceberg discharges of the last glacial period driven by oceanic circulation changes". In: *Proceedings of the National Academy of Sciences* 110.41, pp. 16350–16354.

Andrews, J. and M. Mahaffy (1976). "Growth rate of the Laurentide Ice Sheet and sea level lowering (with emphasis on the 115,000 BP sea level low)". In: *Quaternary Research* 6.2, pp. 167–183.

Armstrong McKay, D. I., A. Staal, J. F. Abrams, R. Winkelmann, B. Sakschewski, S. Loriani, I. Fetzer, S. E. Cornell, J. Rockström, and T. M. Lenton (2022). "Exceeding 1.5°C global warming could trigger multiple climate tipping points". In: *Science* 377.6611. Publisher: American Association for the Advancement of Science, eabn7950.

Bahadory, T., L. Tarasov, and H. Andres (2021). "Last glacial inception trajectories for the Northern Hemisphere from coupled ice and climate modelling". In: *Climate of the Past* 17.1, pp. 397–418.

Bakker, P., V. Masson-Delmotte, B. Martrat, S. Charbit, H. Renssen, M. Gröger, U. Krebs-Kanzow, G. Lohmann, D. J. Lunt, M. Pfeiffer, et al. (2014). "Temperature trends during the Present and Last Interglacial periods–a multi-model-data comparison". In: *Quaternary Science Reviews* 99, pp. 224–243.

Bamber, J. L., R. M. Westaway, B. Marzeion, and B. Wouters (2018). "The land ice contribution to sea level during the satellite era". In: *Environ. Res. Lett.* 13.6, p. 063008.

Barbi, D., N. Wieters, P. Gierz, M. Andrés-Martínez, D. Ural, F. Chegini, S. Khosravi, and L. Cristini (2021). "ESM-Tools version 5.0: a modular infrastructure for stand-alone and coupled Earth system modelling (ESM)". In: *Geoscientific Model Development* 14.6, pp. 4051–4067.

Barker, S., J. Chen, X. Gong, L. Jonkers, G. Knorr, and D. Thornalley (2015). "Icebergs not the trigger for North Atlantic cold events". In: *Nature* 520.7547. Number: 7547 Publisher: Nature Publishing Group, pp. 333–336.

Barker, S., P. Diz, M. J. Vautravers, J. Pike, G. Knorr, I. R. Hall, and W. S. Broecker (2009). "Interhemispheric Atlantic seesaw response during the last deglaciation". In: *Nature* 457.7233, pp. 1097–1102.

Barker, S., G. Knorr, M. J. Vautravers, P. Diz, and L. C. Skinner (2010). "Extreme deepening of the Atlantic overturning circulation during deglaciation". In: *Nature Geoscience* 3.8, pp. 567–571.

Benn, D. I., T. Cowton, J. Todd, and A. Luckman (2017). "Glacier calving in Greenland". In: *Current Climate Change Reports* 3, pp. 282–290.

Berger, A. (1978). "Long-term variations of daily insolation and Quaternary climatic changes". In: *Journal of Atmospheric Sciences* 35.12, pp. 2362–2367.

Bianchi, G. G. and I. N. McCave (1999). "Holocene periodicity in North Atlantic climate and deep-ocean flow south of Iceland". In: *Nature* 397.6719, pp. 515–517.

Bigg, G. R., M. R. Wadley, D. P. Stevens, and J. A. Johnson (1997). "Modelling the dynamics and thermodynamics of icebergs". In: *Cold Regions Science and Technology* 26.2, pp. 113–135.

Boers, N. and M. Rypdal (2021). "Critical slowing down suggests that the western Greenland Ice Sheet is close to a tipping point". In: *Proceedings of the National Academy of Sciences* 118.21. Publisher: Proceedings of the National Academy of Sciences, e2024192118.

Bond, G., H. Heinrich, W. Broecker, L. Labeyrie, J. McManus, J. Andrews, S. Huon, R. Jantschik, S. Clasen, C. Simet, K. Tedesco, M. Klas, G. Bonani, and S. Ivy (1992). "Evidence for massive discharges of icebergs into the North Atlantic ocean during the last glacial period". In: *Nature* 360.6401. Number: 6401 Publisher: Nature Publishing Group, pp. 245–249.

Böning, C. W., E. Behrens, A. Biastoch, K. Getzlaff, and J. L. Bamber (2016). "Emerging impact of Greenland meltwater on deepwater formation in the North Atlantic Ocean". In: *Nature Geoscience* 9.7, pp. 523–527.

Broecker, W., G. Bond, M. Klas, E. Clark, and J. McManus (1992). "Origin of the northern Atlantic's Heinrich events". In: *Climate Dynamics* 6.3, pp. 265–273.

Broecker, W. S. (2000). "Was a change in thermohaline circulation responsible for the Little Ice Age?" In: *Proceedings of the National Academy of Sciences* 97.4, pp. 1339–1342.

Broecker, W. S., D. M. Peteet, and D. Rind (1985). "Does the ocean–atmosphere system have more than one stable mode of operation?" In: *Nature* 315.6014, pp. 21–26.

Bryan, F. (1986). "High-latitude salinity effects and interhemispheric thermohaline circulations". In: *Nature* 323.6086, pp. 301–304.

Budge, J. S. and D. G. Long (2018). "A Comprehensive Database for Antarctic Iceberg Tracking Using Scatterometer Data". In: *IEEE Journal of Selected Topics in Applied Earth Observations and Remote Sensing* 11.2. Conference Name: IEEE Journal of Selected Topics in Applied Earth Observations and Remote Sensing, pp. 434–442.

Bueler, E. and J. Brown (2009). "Shallow shelf approximation as a "sliding law" in a thermomechanically coupled ice sheet model". In: *Journal of Geophysical Research: Earth Surface* 114.F3.

Caley, T., J. Giraudeau, B. Malaizé, L. Rossignol, and C. Pierre (2012). "Agulhas leakage as a key process in the modes of Quaternary climate changes". In: *Proceedings of the National Academy of Sciences* 109.18, pp. 6835–6839.

Calov, R, A. Robinson, M Perrette, and A. Ganopolski (2015). "Simulating the Greenland ice sheet under present-day and palaeo constraints including a new discharge parameterization". In: *The Cryosphere* 9.1, pp. 179–196.

Calov, R., A. Ganopolski, M. Claussen, V. Petoukhov, and R. Greve (2005a). "Transient simulation of the last glacial inception. Part I: glacial inception as a bifurcation in the climate system". In: *Climate Dynamics* 24, pp. 545–561.

Calov, R., A. Ganopolski, V. Petoukhov, M. Claussen, V. Brovkin, and C. Kubatzki (2005b). "Transient simulation of the last glacial inception. Part II: sensitivity and feedback analysis". In: *Climate Dynamics* 24, pp. 563–576.

Calov, R. and R. Greve (2005). "A semi-analytical solution for the positive degree-day model with stochastic temperature variations". In: *Journal of Glaciology* 51.172, pp. 173–175.

Canadell, J. G., P. M. Monteiro, M. H. Costa, L. C. Da Cunha, P. M. Cox, A. V. Eliseev, S. Henson, M. Ishii, S. Jaccard, C. Koven, et al. (2021). *Global carbon and other biogeochemical cycles and feedbacks*.

Charbit, S., D Paillard, and G Ramstein (2008). "Amount of CO2 emissions irreversibly leading to the total melting of Greenland". In: *Geophysical Research Letters* 35.12.

Charbit, S., C. Ritz, and G. Ramstein (2002). "Simulations of Northern Hemisphere ice-sheet retreat:: sensitivity to physical mechanisms involved during the Last Deglaciation". In: *Quaternary Science Reviews* 21.1-3, pp. 243–265.

Clark, P. U. and A. C. Mix (2002). "Ice sheets and sea level of the Last Glacial Maximum". In: *Quaternary Science Reviews* 21.1-3, pp. 1–7.

Clark, P. U., N. G. Pisias, T. F. Stocker, and A. J. Weaver (2002). "The role of the thermohaline circulation in abrupt climate change". In: *Nature* 415.6874, pp. 863–869.

Clarke, G. K. (2005). "Subglacial processes". In: *Annu. Rev. Earth Planet. Sci.* 33, pp. 247–276.

Clarke, L. E. (2007). *Scenarios of Greenhouse Gas Emissions and Atmospheric Concentrations: Report*. Vol. 2. US Climate Change Science Program.

Claussen, M., L Mysak, A Weaver, M. Crucifix, T. Fichefet, M.-F. Loutre, S. Weber, J. Alcamo, V. Alexeev, A. Berger, et al. (2002). "Earth system models of intermediate complexity: closing the gap in the spectrum of climate system models". In: *Climate dynamics* 18, pp. 579–586.

Colbourn, G, A Ridgwell, and T. Lenton (2015). "The time scale of the silicate weathering negative feedback on atmospheric CO2". In: *Global Biogeochemical Cycles* 29.5, pp. 583–596.

Cuffey, K. M. and S. J. Marshall (2000). "Substantial contribution to sea-level rise during the last interglacial from the Greenland ice sheet". In: *Nature* 404.6778. Number: 6778 Publisher: Nature Publishing Group, pp. 591–594.

Cuffey, K. M. and W. S. B. Paterson (2010). *The physics of glaciers*. Academic Press.

Cunningham, S., S. Alderson, B. King, and M. Brandon (2003). "Transport and variability of the Antarctic circumpolar current in drake passage". In: *Journal of Geophysical Research: Oceans* 108.C5.

Danek, C., P. Scholz, and G. Lohmann (2019). "Effects of high resolution and spinup time on modeled North Atlantic circulation". In: *Journal of Physical Oceanography* 49.5, pp. 1159–1181.

Danilov, S., D. Sidorenko, Q. Wang, and T. Jung (2017). "The Finite-volumE Sea ice–Ocean Model (FESOM2)". In: *Geoscientific Model Development* 10.2. Publisher: Copernicus GmbH, pp. 765–789.

Danilov, S., Q. Wang, D. Sidorenko, P. Scholz, T. Semmler, and H. Gössling (2023). "FESOM Meshes". In: *https://fesom.de/models/meshessetups/*.

De Lavergne, C., J. B. Palter, E. D. Galbraith, R. Bernardello, and I. Marinov (2014). "Cessation of deep convection in the open Southern Ocean under anthropogenic climate change". In: *Nature Climate Change* 4.4, pp. 278–282.

Delworth, T. L., A. J. Broccoli, A. Rosati, R. J. Stouffer, V Balaji, J. A. Beesley, W. F. Cooke, K. W. Dixon, J. Dunne, K. Dunne, et al. (2006). "GFDL's CM2 global coupled climate models. Part I: Formulation and simulation characteristics". In: *Journal of Climate* 19.5, pp. 643–674.

Delworth, T. L., A. Rosati, W. Anderson, A. J. Adcroft, V. Balaji, R. Benson, K. Dixon, S. M. Griffies, H.-C. Lee, R. C. Pacanowski, G. A. Vecchi, A. T. Wittenberg, F. Zeng, and R. Zhang (2012). "Simulated Climate and Climate Change in the GFDL CM2.5 High-Resolution Coupled Climate Model". In: *Journal of Climate* 25.8. Publisher: American Meteorological Society Section: Journal of Climate, pp. 2755–2781.

Depoorter, M. A., J. L. Bamber, J. A. Griggs, J. T. M. Lenaerts, S. R. M. Ligtenberg, M. R. van den Broeke, and G. Moholdt (2013). "Calving fluxes and basal melt rates of Antarctic ice shelves". In: *Nature* 502.7469. Number: 7469 Publisher: Nature Publishing Group, pp. 89–92.

Devilliers, M., D. Swingedouw, J. Mignot, J. Deshayes, G. Garric, and M. Ayache (2021). "A realistic Greenland ice sheet and surrounding glaciers and ice caps melting in a coupled climate model". In: *Clim Dyn* 57.9, pp. 2467–2489.

Dima, M. and G. Lohmann (2010). "Evidence for two distinct modes of large-scale ocean circulation changes over the last century". In: *Journal of Climate* 23.1, pp. 5–16.

Dima, M., D. R. Nichita, G. Lohmann, M. Ionita, and M. Voiculescu (2021). "Early-onset of Atlantic Meridional Overturning Circulation weakening in response to atmospheric CO2 concentration". In: *npj Climate and Atmospheric Science* 4.1, p. 27.

Driesschaert, E., T. Fichefet, H. Goosse, P. Huybrechts, I. Janssens, A. Mouchet, G. Munhoven, V. Brovkin, and S. Weber (2007). "Modeling the influence of Greenland ice sheet melting on the Atlantic meridional overturning circulation during the next millennia". In: *Geophysical Research Letters* 34.10.

Dutton, A., A. E. Carlson, A. J. Long, G. A. Milne, P. U. Clark, R DeConto, B. P. Horton, S. Rahmstorf, and M. E. Raymo (2015). "Sea-level rise due to polar ice-sheet mass loss during past warm periods". In: *science* 349.6244, aaa4019.

Eden, C. and C. Böning (2002). "Sources of eddy kinetic energy in the Labrador Sea". In: *Journal of Physical Oceanography* 32.12, pp. 3346–3363.

Enderlin, E. M., C. J. Carrigan, W. H. Kochtitzky, A. Cuadros, T. Moon, and G. S. Hamilton (2018). "Greenland iceberg melt variability from high-resolution satellite observations". In: *The Cryosphere* 12.2. Publisher: Copernicus GmbH, pp. 565–575.

England, M. R., T. J. Wagner, and I. Eisenman (2020). "Modeling the breakup of tabular icebergs". In: *Science advances* 6.51, eabd1273.

Ferrari, R., S. M. Griffies, A. G. Nurser, and G. K. Vallis (2010). "A boundary-value problem for the parameterized mesoscale eddy transport". In: *Ocean Modelling* 32.3-4, pp. 143–156.

Flato, G., J. Marotzke, B. Abiodun, P. Braconnot, S. C. Chou, W. Collins, P. Cox, F. Driouech, S. Emori, V. Eyring, et al. (2014). "Evaluation of climate models". In: *Climate change 2013: the physical science basis. Contribution of Working Group I to the Fifth Assessment Report of the Intergovernmental Panel on Climate Change*. Cambridge University Press, pp. 741–866.

Frölicher, T. L., J. L. Sarmiento, D. J. Paynter, J. P. Dunne, J. P. Krasting, and M. Winton (2015). "Dominance of the Southern Ocean in anthropogenic carbon and heat uptake in CMIP5 models". In: *Journal of Climate* 28.2, pp. 862–886.

Ganopolski, A, R Calov, and M. Claussen (2010). "Simulation of the last glacial cycle with a coupled climate ice-sheet model of intermediate complexity". In: *Climate of the Past* 6.2, pp. 229–244.

Ganopolski, A. and V. Brovkin (2017). "Simulation of climate, ice sheets and CO 2 evolution during the last four glacial cycles with an Earth system model of intermediate complexity". In: *Climate of the Past* 13.12, pp. 1695–1716.

Gent, P. R. and J. C. McWilliams (1990). "Isopycnal mixing in ocean circulation models". In: *Journal of Physical Oceanography* 20.1, pp. 150–155.

Gierz, P., G. Lohmann, and W. Wei (2015). "Response of Atlantic overturning to future warming in a coupled atmosphere-ocean-ice sheet model". In: *Geophysical Research Letters* 42.16, pp. 6811–6818.

Gladstone, R. M., G. R. Bigg, and K. W. Nicholls (2001). "Iceberg trajectory modeling and meltwater injection in the Southern Ocean". In: *Journal of Geophysical Research: Oceans* 106.C9, pp. 19903–19915.

Gleick, P. (1993). *Water in Crisis: Chapter 2 (Oxford University Press) 1993*.

Goelzer, H., P. Huybrechts, M.-F. Loutre, and T. Fichefet (2016). "Last Interglacial climate and sea-level evolution from a coupled ice sheet–climate model". In: *Climate of the Past* 12.12, pp. 2195–2213.

Golledge, N. R., E. D. Keller, N. Gomez, K. A. Naughten, J. Bernales, L. D. Trusel, and T. L. Edwards (2019). "Global environmental consequences of twenty-first-century ice-sheet melt". In: *Nature* 566.7742, pp. 65–72.

Gordon, A. L. (1966). "Potential temperature, oxygen and circulation of bottom water in the Southern Ocean". In: *Deep Sea Research and Oceanographic Abstracts*. Vol. 13. 6. Elsevier, pp. 1125–1138.

Griffies, S. M. (1998). "The gent–mcwilliams skew flux". In: *Journal of Physical Oceanography* 28.5, pp. 831–841.

Griffies, S. M., A. Gnanadesikan, R. C. Pacanowski, V. D. Larichev, J. K. Dukowicz, and R. D. Smith (1998). "Isoneutral diffusion in a z-coordinate ocean model". In: *Journal of Physical Oceanography* 28.5, pp. 805–830.

Grosfeld, K., M. Schröder, E. Fahrbach, R. Gerdes, and A. Mackensen (2001). "How iceberg calving and grounding change the circulation and hydrography in the Filchner Ice Shelf-Ocean System". In: *Journal of Geophysical Research: Oceans* 106.C5, pp. 9039–9055.

Hagemann, S. and L. Dümenil (1997). "A parametrization of the lateral waterflow for the global scale". In: *Climate Dynamics* 14.1, pp. 17–31.

Hasenclever, J., G. Knorr, L. H. Rüpke, P. Köhler, J. Morgan, K. Garofalo, S. Barker, G. Lohmann, and I. R. Hall (2017). "Sea level fall during glaciation stabilized atmospheric CO2 by enhanced volcanic degassing". In: *Nature Communications* 8.1, p. 15867.

Heinrich, H. (1988). "Origin and consequences of cyclic ice rafting in the Northeast Atlantic Ocean during the past 130,000 years". In: *Quaternary Research* 29.2, pp. 142–152.

Hellmer, H. H. and D. J. Olbers (1989). "A two-dimensional model for the thermohaline circulation under an ice shelf'. In: *Antarctic Science* 1.4. Publisher: Cambridge University Press, pp. 325–336.

Herrington, A. R. and C. J. Poulsen (2011). "Terminating the Last Interglacial: The role of ice sheet–climate feedbacks in a GCM asynchronously coupled to an ice sheet model". In: *Journal of climate* 25.6, pp. 1871–1882.

Heuzé, C. (2021). "Antarctic Bottom Water and North Atlantic Deep Water in CMIP6 models". In: *Ocean Science* 17.1. Publisher: Copernicus GmbH, pp. 59–90.

Holland, D. M. and A. Jenkins (1999). "Modeling Thermodynamic Ice–Ocean Interactions at the Base of an Ice Shelf'. In: *Journal of Physical Oceanography* 29.8. Publisher: American Meteorological Society Section: Journal of Physical Oceanography, pp. 1787–1800.

Hu, A., G. A. Meehl, W. Han, and J. Yin (2009). "Transient response of the MOC and climate to potential melting of the Greenland Ice Sheet in the 21st century". In: *Geophysical Research Letters* 36.10.

– (2011). "Effect of the potential melting of the Greenland Ice Sheet on the Meridional Overturning Circulation and global climate in the future". In: *Deep Sea Research Part II: Topical Studies in Oceanography* 58.17-18, pp. 1914–1926.

Huybrechts, P., H. Goelzer, I. Janssens, E. Driesschaert, T. Fichefet, H. Goosse, and M.-F. Loutre (2011). "Response of the Greenland and Antarctic ice sheets

to multi-millennial greenhouse warming in the Earth system model of intermediate complexity LOVECLIM". In: *Surveys in Geophysics* 32, pp. 397–416.

IPCC (2022). *The Ocean and Cryosphere in a Changing Climate: Special Report of the Intergovernmental Panel on Climate Change*. 1st ed. Cambridge University Press.

Jackson, L. (2013). "Shutdown and recovery of the AMOC in a coupled global climate model: the role of the advective feedback". In: *Geophysical Research Letters* 40.6, pp. 1182–1188.

Jacobs, S. S., H. H. Helmer, C. S. M. Doake, A. Jenkins, and R. M. Frolich (1992). "Melting of ice shelves and the mass balance of Antarctica". In: *Journal of Glaciology* 38.130. Publisher: Cambridge University Press, pp. 375–387.

Johnson, G. C. (2008). "Quantifying Antarctic bottom water and North Atlantic deep water volumes". In: *Journal of Geophysical Research: Oceans* 113.C5.

Jongma, J. I., E. Driesschaert, T. Fichefet, H. Goosse, and H. Renssen (2009). "The effect of dynamic–thermodynamic icebergs on the Southern Ocean climate in a three-dimensional model". In: *Ocean Modelling* 26.1, pp. 104–113.

Jungclaus, J. H., N. Fischer, H. Haak, K. Lohmann, J. Marotzke, D. Matei, U. Mikolajewicz, D. Notz, and J. S. von Storch (2013). "Characteristics of the ocean simulations in the Max Planck Institute Ocean Model (MPIOM) the ocean component of the MPI-Earth system model". In: *Journal of Advances in Modeling Earth Systems* 5.2, pp. 422–446.

Jungclaus, J., H Haak, M Esch, E Roeckner, and J Marotzke (2006). "Will Greenland melting halt the thermohaline circulation?" In: *Geophysical Research Letters* 33.17.

Kageyama, M., S. Charbit, C. Ritz, M. Khodri, and G. Ramstein (2004). "Quantifying ice-sheet feedbacks during the last glacial inception". In: *Geophysical Research Letters* 31.24.

Kalnay, E., M. Kanamitsu, R. Kistler, W. Collins, D. Deaven, L. Gandin, M. Iredell, S. Saha, G. White, J. Woollen, et al. (1996). "The NCEP/NCAR 40-year reanalysis project". In: *Bulletin of the American meteorological Society* 77.3, pp. 437–472.

Keigwin, L., G. Jones, S. Lehman, and E. Boyle (1991). "Deglacial meltwater discharge, North Atlantic deep circulation, and abrupt climate change". In: *Journal of Geophysical Research: Oceans* 96.C9, pp. 16811–16826.

Kikstra, J. S., Z. R. Nicholls, C. J. Smith, J. Lewis, R. D. Lamboll, E. Byers, M. Sandstad, M. Meinshausen, M. J. Gidden, J. Rogelj, et al. (2022). "The IPCC Sixth Assessment Report WGIII climate assessment of mitigation pathways:

from emissions to global temperatures". In: *Geoscientific Model Development* 15.24, pp. 9075–9109.

King, M. D., I. M. Howat, S. Jeong, M. J. Noh, B. Wouters, B. Noël, and M. R. van den Broeke (2018). "Seasonal to decadal variability in ice discharge from the Greenland Ice Sheet". In: *The Cryosphere* 12.12, pp. 3813–3825.

Kistler, R., E. Kalnay, W. Collins, S. Saha, G. White, J. Woollen, M. Chelliah, W. Ebisuzaki, M. Kanamitsu, V. Kousky, et al. (2001). "The NCEP–NCAR 50-year reanalysis: monthly means CD-ROM and documentation". In: *Bulletin of the American Meteorological society* 82.2, pp. 247–268.

Knorr, G. and G. Lohmann (2003). "Southern Ocean origin for the resumption of Atlantic thermohaline circulation during deglaciation". In: *Nature* 424.6948, pp. 532–536.

– (2007). "Rapid transitions in the Atlantic thermohaline circulation triggered by global warming and meltwater during the last deglaciation". In: *Geochemistry, Geophysics, Geosystems* 8.12.

Köhler, P., C. Nehrbass-Ahles, J. Schmitt, T. F. Stocker, and H. Fischer (2017). "A 156 kyr smoothed history of the atmospheric greenhouse gases CO 2, CH 4, and N 2 O and their radiative forcing". In: *Earth System Science Data* 9.1, pp. 363–387.

Koldunov, N. V., V. Aizinger, N. Rakowsky, P. Scholz, D. Sidorenko, S. Danilov, and T. Jung (2019). "Scalability and some optimization of the Finite-volumE Sea ice–Ocean Model, Version 2.0 (FESOM2)". In: *Geoscientific Model Development* 12.9, pp. 3991–4012.

Krebs-Kanzow, U., P. Gierz, C. B. Rodehacke, S. Xu, H. Yang, and G. Lohmann (2021). "The diurnal Energy Balance Model (dEBM): a convenient surface mass balance solution for ice sheets in Earth system modeling". In: *The Cryosphere* 15.5, pp. 2295–2313.

Latif, M., E. Roeckner, U. Mikolajewicz, and R. Voss (2000). "Tropical Stabilization of the Thermohaline Circulation in a Greenhouse Warming Simulation". In: *Journal of Climate* 13.11. Publisher: American Meteorological Society Section: Journal of Climate, pp. 1809–1813.

Lenaerts, J. T., D. Le Bars, L. Van Kampenhout, M. Vizcaino, E. M. Enderlin, and M. R. Van Den Broeke (2015). "Representing Greenland ice sheet freshwater fluxes in climate models". In: *Geophysical Research Letters* 42.15, pp. 6373–6381.

Lenton, T. M., J. Rockström, O. Gaffney, S. Rahmstorf, K. Richardson, W. Steffen, and H. J. Schellnhuber (2019). "Climate tipping points — too risky to bet against". In: *Nature* 575.7784. Bandiera_abtest: a Cg_type: Comment

Number: 7784 Publisher: Nature Publishing Group Subject_term: Climate change, Climate sciences, Environmental sciences, Policy, pp. 592–595.

Levermann, A., T. Albrecht, R. Winkelmann, M. A. Martin, M. Haseloff, and I. Joughin (2012). "Kinematic first-order calving law implies potential for abrupt ice-shelf retreat". In: *The Cryosphere* 6.2. Publisher: Copernicus GmbH, pp. 273–286.

Lind, S., R. B. Ingvaldsen, and T. Furevik (2018). "Arctic warming hotspot in the northern Barents Sea linked to declining sea-ice import". In: *Nature climate change* 8.7, pp. 634–639.

Liu, W., A. Fedorov, and F. Sévellec (2019). "The mechanisms of the Atlantic meridional overturning circulation slowdown induced by Arctic sea ice decline". In: *Journal of Climate* 32.4, pp. 977–996.

Liu, W., Z. Liu, and A. Hu (2013). "The stability of an evolving Atlantic meridional overturning circulation". In: *Geophysical Research Letters* 40.8, pp. 1562–1568.

Liu, Y., R. Hallberg, O. Sergienko, B. L. Samuels, M. Harrison, and M. Oppenheimer (2018). "Climate response to the meltwater runoff from Greenland ice sheet: evolving sensitivity to discharging locations". In: *Climate Dynamics* 51, pp. 1733–1751.

Lohmann, G. (2003). "Atmospheric and oceanic freshwater transport during weak Atlantic overturning circulation". In: *Tellus A: Dynamic Meteorology and Oceanography* 55.5, pp. 438–449.

Manabe, S., K. Bryan, and M. J. Spelman (1990). "Transient response of a global ocean-atmosphere model to a doubling of atmospheric carbon dioxide". In: *Journal of Physical Oceanography* 20.5, pp. 722–749.

Manabe, S. and R. J. Stouffer (1993). "Century-scale effects of increased atmospheric C02 on the ocean–atmosphere system". In: *Nature* 364.6434, pp. 215–218.

– (1995). "Simulation of abrupt climate change induced by freshwater input to the North Atlantic Ocean". In: *Nature* 378.6553, pp. 165–167.

Marcott, S. A., P. U. Clark, L. Padman, G. P. Klinkhammer, S. R. Springer, Z. Liu, B. L. Otto-Bliesner, A. E. Carlson, A. Ungerer, J. Padman, F. He, J. Cheng, and A. Schmittner (2011). "Ice-shelf collapse from subsurface warming as a trigger for Heinrich events". In: *PNAS* 108.33. ISBN: 9781104772109 Publisher: National Academy of Sciences Section: Physical Sciences, pp. 13415–13419.

Marino, G., R. Zahn, M. Ziegler, C. Purcell, G. Knorr, I. R. Hall, P. Ziveri, and H. Elderfield (2013). "Agulhas salt-leakage oscillations during abrupt climate changes of the Late Pleistocene". In: *Paleoceanography* 28.3, pp. 599–606.

Marinov, I, A Gnanadesikan, J. Toggweiler, and J. L. Sarmiento (2006). "The southern ocean biogeochemical divide". In: *Nature* 441.7096, pp. 964–967.

Marsh, R., V. O. Ivchenko, N. Skliris, S. Alderson, G. R. Bigg, G. Madec, A. T. Blaker, Y. Aksenov, B. Sinha, A. C. Coward, J. Le Sommer, N. Merino, and V. B. Zalesny (2015). "NEMO–ICB (v1.0): interactive icebergs in the NEMO ocean model globally configured at eddy-permitting resolution". In: *Geoscientific Model Development* 8.5. Publisher: Copernicus GmbH, pp. 1547–1562.

Martin, T. and A. Adcroft (2010). "Parameterizing the fresh-water flux from land ice to ocean with interactive icebergs in a coupled climate model". In: *Ocean Modelling* 34.3, pp. 111–124.

"Mass balance of the Greenland Ice Sheet from 1992 to 2018" (2020). In: *Nature* 579.7798, pp. 233–239.

Masson-Delmotte, V., P. Zhai, H.-O. Pörtner, D. Roberts, J. Skea, P. Shukla, A. Pirani, W. Moufouma-Okia, C. Péan, R. Pidcock, S. Connors, J. Matthews, Y. Chen, X. Zhou, M. Gomis, E. Lonnoy, T. Maycock, M. Tignor, and T. Waterfield (2018). "Annex I: Glossary [Matthews, J.B.R. (ed.)]" In: *Global Warming of 1.5°C. An IPCC Special Report on the impacts of global warming of 1.5°C above pre-industrial levels and related global greenhouse gas emission pathways, in the context of strengthening the global response to the threat of climate change, sustainable development, and efforts to eradicate poverty.*

Masson-Delmotte, V., P. Zhai, A. Pirani, S. L. Connors, C. Péan, S. Berger, N. Caud, Y Chen, L Goldfarb, M. Gomis, et al. (2021). "Climate change 2021: the physical science basis". In: *Contribution of working group I to the sixth assessment report of the intergovernmental panel on climate change* 2.

McManus, J. F., R. Francois, J.-M. Gherardi, L. D. Keigwin, and S. Brown-Leger (2004). "Collapse and rapid resumption of Atlantic meridional circulation linked to deglacial climate changes". In: *Nature* 428.6985, pp. 834–837.

Merino, N., J. Le Sommer, G. Durand, N. C. Jourdain, G. Madec, P. Mathiot, and J. Tournadre (2016). "Antarctic icebergs melt over the Southern Ocean: Climatology and impact on sea ice". In: *Ocean Modelling* 104, pp. 99–110.

Mikolajewicz, U., M. Vizcaino, J. Jungclaus, and G. Schurgers (2007). "Effect of ice sheet interactions in anthropogenic climate change simulations". In: *Geophysical Research Letters* 34.18.

Milankovitch, M. (1941). "Canon of insolation and the iceage problem". In: *Koniglich Serbische Akademice Beograd Special Publication* 132.

Mouginot, J., E. Rignot, A. A. Bjørk, M. Van den Broeke, R. Millan, M. Morlighem, B. Noël, B. Scheuchl, and M. Wood (2019). "Forty-six years of Greenland Ice Sheet mass balance from 1972 to 2018". In: *Proceedings of the national academy of sciences* 116.19, pp. 9239–9244.

Neshyba, S. and E. G. Josberger (1980). "On the Estimation of Antarctic Iceberg Melt Rate". In: *Journal of Physical Oceanography* 10.10. Publisher: American Meteorological Society Section: Journal of Physical Oceanography, pp. 1681–1685.

Niu, L., G. Lohmann, P. Gierz, E. J. Gowan, and G. Knorr (2021). "Coupled climate-ice sheet modelling of MIS-13 reveals a sensitive Cordilleran Ice Sheet". In: *Global and Planetary Change* 200, p. 103474.

Niu, L., G. Lohmann, and E. J. Gowan (2019a). "Climate noise influences ice sheet mean state". In: *Geophysical Research Letters* 46.16, pp. 9690–9699.

Niu, L., G. Lohmann, S. Hinck, E. J. Gowan, and U. Krebs-Kanzow (2019b). "The sensitivity of Northern Hemisphere ice sheets to atmospheric forcing during the last glacial cycle using PMIP3 models". In: *Journal of Glaciology* 65.252, pp. 645–661.

Nowicki, S. M., A. Payne, E. Larour, H. Seroussi, H. Goelzer, W. Lipscomb, J. Gregory, A. Abe-Ouchi, and A. Shepherd (2016). "Ice sheet model intercomparison project (ISMIP6) contribution to CMIP6". In: *Geoscientific model development* 9.12, pp. 4521–4545.

Olbers, D. and H. Hellmer (2010). "A box model of circulation and melting in ice shelf caverns". In: *Ocean Dynamics* 60, pp. 141–153.

Orsi, A. H., G. C. Johnson, and J. L. Bullister (1999). "Circulation, mixing, and production of Antarctic Bottom Water". In: *Progress in Oceanography* 43.1, pp. 55–109.

Pattyn, F. and M. Morlighem (2020). "The uncertain future of the Antarctic Ice Sheet". In: *Science* 367.6484. Publisher: American Association for the Advancement of Science, pp. 1331–1335.

Peltier, W. R. (2002). "On eustatic sea level history: Last Glacial Maximum to Holocene". In: *Quaternary Science Reviews* 21.1-3, pp. 377–396.

Plach, A., K. H. Nisancioglu, A. Born, P. M. Langebroek, C. Guo, M. Imhof, T. F. Stocker, et al. (2018). "Eemian Greenland SMB strongly sensitive to model choice". In: *Climate of the Past* 14.10, pp. 1463–1485.

Purkey, S. G. and G. C. Johnson (2013). "Antarctic Bottom Water warming and freshening: Contributions to sea level rise, ocean freshwater budgets, and global heat gain". In: *Journal of Climate* 26.16, pp. 6105–6122.

Quiquet, A, C Ritz, H. Punge, and D Salas y Mélia (2013). "Greenland ice sheet contribution to sea level rise during the last interglacial period: a modelling study driven and constrained by ice core data". In: *Climate of the Past* 9.1, pp. 353–366.

Rachmayani, R., M. Prange, D. J. Lunt, E. J. Stone, and M. Schulz (2017). "Sensitivity of the Greenland Ice Sheet to interglacial climate forcing: MIS 5e versus MIS 11". In: *Paleoceanography* 32.11, pp. 1089–1101.

Rackow, T. (2011). "Modellierung der Eisbergdrift als Erweiterung eines Finite-Elemente-Meereis-Ozean-Modells". Publication Title: EPIC3156 p. diplom. Universität Bremen, Alfred-Wegener-Institut für Polar- und Meeresforschung.

Rackow, T., H. F. Goessling, T. Jung, D. Sidorenko, T. Semmler, D. Barbi, and D. Handorf (2018). "Towards multi-resolution global climate modeling with ECHAM6-FESOM. Part II: climate variability". In: *Climate Dynamics* 50. Publisher: Springer.

Rackow, T., D. V. Sein, T. Semmler, S. Danilov, N. V. Koldunov, D. Sidorenko, Q. Wang, and T. Jung (2019). "Sensitivity of deep ocean biases to horizontal resolution in prototype CMIP6 simulations with AWI-CM1.0". In: *Geoscientific Model Development* 12.7. Publisher: Copernicus GmbH, pp. 2635–2656.

Rackow, T., C. Wesche, R. Timmermann, H. H. Hellmer, S. Juricke, and T. Jung (2017). "A simulation of small to giant Antarctic iceberg evolution: Differential impact on climatology estimates". In: *Journal of Geophysical Research: Oceans* 122.4, pp. 3170–3190.

Rahmstorf, S. (1996). "On the freshwater forcing and transport of the Atlantic thermohaline circulation". In: *Climate Dynamics* 12, pp. 799–811.

– (2002). "Ocean circulation and climate during the past 120,000 years". In: *Nature* 419.6903. Bandiera_abtest: a Cg_type: Nature Research Journals Number: 6903 Primary_atype: Reviews Publisher: Nature Publishing Group, pp. 207–214.

Rahmstorf, S., J. E. Box, G. Feulner, M. E. Mann, A. Robinson, S. Rutherford, and E. J. Schaffernicht (2015). "Exceptional twentieth-century slowdown in Atlantic Ocean overturning circulation". In: *Nature climate change* 5.5, pp. 475–480.

Rahmstorf, S., G. Foster, and A. Cazenave (2012). "Comparing climate projections to observations up to 2011". In: *Environmental Research Letters* 7.4, p. 044035.

Raiswell, R., L. G. Benning, M. Tranter, and S. Tulaczyk (2008). "Bioavailable iron in the Southern Ocean: the significance of the iceberg conveyor belt". In: *Geochemical transactions* 9.1, pp. 1–9.

Redi, M. H. (1982). "Oceanic isopycnal mixing by coordinate rotation". In: *Journal of Physical Oceanography* 12.10, pp. 1154–1158.

Reeh, N. (1991). "Parameterization of melt rate and surface temperature in the Greenland ice sheet". In: *Polarforschung* 59.3, pp. 113–128.

Reese, R., T. Albrecht, M. Mengel, X. Asay-Davis, and R. Winkelmann (2018). "Antarctic sub-shelf melt rates via PICO". In: *The Cryosphere* 12.6. Publisher: Copernicus GmbH, pp. 1969–1985.

Reick, C. H., T. Raddatz, V. Brovkin, and V. Gayler (2013). "Representation of natural and anthropogenic land cover change in MPI-ESM". In: *Journal of Advances in Modeling Earth Systems* 5.3, pp. 459–482.

Riahi, K., A. Grübler, and N. Nakicenovic (2007). "Scenarios of long-term socio-economic and environmental development under climate stabilization". In: *Technological forecasting and social change* 74.7, pp. 887–935.

Ridley, J., J. M. Gregory, P. Huybrechts, and J. Lowe (2010). "Thresholds for irreversible decline of the Greenland ice sheet". In: *Climate Dynamics* 35, pp. 1049–1057.

Robinson, A., R. Calov, and A. Ganopolski (2011). "Greenland ice sheet model parameters constrained using simulations of the Eemian Interglacial". In: *Climate of the Past* 7.2, pp. 381–396.

Rosier, S. H. R., R. Reese, J. F. Donges, J. De Rydt, G. H. Gudmundsson, and R. Winkelmann (2021). "The tipping points and early warning indicators for Pine Island Glacier, West Antarctica". In: *The Cryosphere* 15.3. Publisher: Copernicus GmbH, pp. 1501–1516.

Ruddiman, W. F. (2001). *Earth's climate: past and future*. Macmillan.

Saha, S., S. Moorthi, H.-L. Pan, X. Wu, J. Wang, S. Nadiga, P. Tripp, R. Kistler, J. Woollen, D. Behringer, et al. (2010). "The NCEP climate forecast system reanalysis". In: *Bulletin of the American Meteorological Society* 91.8, pp. 1015–1058.

Schmidt, S. and U. Send (2007). "Origin and composition of seasonal Labrador Sea freshwater". In: *Journal of Physical Oceanography* 37.6, pp. 1445–1454.

Schmitz Jr, W. J. (1995). "On the interbasin-scale thermohaline circulation". In: *Reviews of Geophysics* 33.2, pp. 151–173.

Scholz, P., D. Sidorenko, S. Danilov, Q. Wang, N. Koldunov, D. Sein, and T. Jung (2022). "Assessment of the Finite-VolumE Sea ice–Ocean Model (FESOM2. 0)–Part 2: Partial bottom cells, embedded sea ice and vertical mixing library CVMix". In: *Geoscientific Model Development* 15.2, pp. 335–363.

Scholz, P., D. Sidorenko, O. Gurses, S. Danilov, N. Koldunov, Q. Wang, D. Sein, M. Smolentseva, N. Rakowsky, and T. Jung (2019). "Assessment of

the Finite VolumE Sea Ice Ocean Model (FESOM2.0), Part I: Description of selected key model elements and comparison to its predecessor version". In: *Geoscientific Model Development Discussions*, pp. 1–42.

Semmler, T., S. Danilov, P. Gierz, H. F. Goessling, J. Hegewald, C. Hinrichs, N. Koldunov, N. Khosravi, L. Mu, T. Rackow, D. V. Sein, D. Sidorenko, Q. Wang, and T. Jung (2020). "Simulations for CMIP6 With the AWI Climate Model AWI-CM-1-1". In: *Journal of Advances in Modeling Earth Systems* 12.9, e2019MS002009.

Shaffer, G., S. M. Olsen, and C. J. Bjerrum (2004). "Ocean subsurface warming as a mechanism for coupling Dansgaard-Oeschger climate cycles and ice-rafting events". In: *Geophysical Research Letters* 31.24.

Shi, X. and G. Lohmann (2016). "Simulated response of the mid-Holocene Atlantic meridional overturning circulation in ECHAM6-FESOM/MPIOM". In: *Journal of Geophysical Research: Oceans* 121.8, pp. 6444–6469.

Shikazono, N. and N. Shikazono (2012). "Components of the Earth System". In: *Introduction to Earth and Planetary System Science: New View of Earth, Planets and Humans*, pp. 11–41.

Sidorenko, D., H. Goessling, N. Koldunov, P. Scholz, S. Danilov, D. Barbi, W. Cabos, O. Gurses, S. Harig, C. Hinrichs, S. Juricke, G. Lohmann, M. Losch, L. Mu, T. Rackow, N. Rakowsky, D. Sein, T. Semmler, X. Shi, C. Stepanek, J. Streffing, Q. Wang, C. Wekerle, H. Yang, and T. Jung (2019). "Evaluation of FESOM2.0 Coupled to ECHAM6.3: Preindustrial and HighResMIP Simulations". In: *Journal of Advances in Modeling Earth Systems* 11.11, pp. 3794–3815.

Sidorenko, D., T. Rackow, T. Jung, T. Semmler, D. Barbi, S. Danilov, K. Dethloff, W. Dorn, K. Fieg, H. F. Gößling, D. Handorf, S. Harig, W. Hiller, S. Juricke, M. Losch, J. Schröter, D. Sein, and Q. Wang (2015). "Towards multi-resolution global climate modeling with ECHAM6–FESOM. Part I: model formulation and mean climate". In: *Climate Dynamics* 44.3. Number: 3 Publisher: Springer, pp. 757–780.

Silvano, A., S. R. Rintoul, B. Peña-Molino, W. R. Hobbs, E. van Wijk, S. Aoki, T. Tamura, and G. D. Williams (2018). "Freshening by glacial meltwater enhances melting of ice shelves and reduces formation of Antarctic Bottom Water". In: *Science advances* 4.4, eaap9467.

Stammer, D, N Agarwal, P Herrmann, A. Köhl, and C. Mechoso (2011). "Response of a coupled ocean–atmosphere model to Greenland ice melting". In: *Surveys in geophysics* 32, pp. 621–642.

Starr, A., I. R. Hall, S. Barker, T. Rackow, X. Zhang, S. R. Hemming, H. J. L. van der Lubbe, G. Knorr, M. A. Berke, G. R. Bigg, A. Cartagena-Sierra, F. J. Jiménez-Espejo, X. Gong, J. Gruetzner, N. Lathika, L. J. LeVay, R. S. Robinson, and M. Ziegler (2021). "Antarctic icebergs reorganize ocean circulation during Pleistocene glacials". In: *Nature* 589.7841. Number: 7841 Publisher: Nature Publishing Group, pp. 236–241.

Sterl, A., R. Bintanja, L. Brodeau, E. Gleeson, T. Koenigk, T. Schmith, T. Semmler, C. Severijns, K. Wyser, and S. Yang (2012). "A look at the ocean in the EC-Earth climate model". In: *Clim Dyn* 39.11, pp. 2631–2657.

Stern, A. A., A. Adcroft, and O. Sergienko (2016). "The effects of Antarctic iceberg calving-size distribution in a global climate model". In: *Journal of Geophysical Research: Oceans* 121.8, pp. 5773–5788.

Stern, A. A., E. Johnson, D. M. Holland, T. J. Wagner, P. Wadhams, R. Bates, E. P. Abrahamsen, K. W. Nicholls, A. Crawford, J. Gagnon, and J.-E. Tremblay (2015). "Wind-driven upwelling around grounded tabular icebergs". In: *Journal of Geophysical Research: Oceans* 120.8, pp. 5820–5835.

Stevens, B., M. Giorgetta, M. Esch, T. Mauritsen, T. Crueger, S. Rast, M. Salzmann, H. Schmidt, J. Bader, K. Block, R. Brokopf, I. Fast, S. Kinne, L. Kornblueh, U. Lohmann, R. Pincus, T. Reichler, and E. Roeckner (2013). "Atmospheric component of the MPI-M Earth System Model: ECHAM6". In: *Journal of Advances in Modeling Earth Systems* 5.2, pp. 146–172.

Stocker, T. (2014). *Climate change 2013: the physical science basis: Working Group I contribution to the Fifth assessment report of the Intergovernmental Panel on Climate Change*. Cambridge university press.

Stocker, T. F. and A. Schmittner (1997). "Influence of CO2 emission rates on the stability of the thermohaline circulation". In: *Nature* 388.6645, pp. 862–865.

Stone, E., D. Lunt, J. Annan, and J. Hargreaves (2013). "Quantification of the Greenland ice sheet contribution to Last Interglacial sea level rise". In: *Climate of the Past* 9.2, pp. 621–639.

Streffing, J., D. Sidorenko, T. Semmler, L. Zampieri, P. Scholz, M. Andrés-Martínez, N. Koldunov, T. Rackow, J. Kjellsson, H. Goessling, M. Athanase, Q. Wang, J. Hegewald, D. V. Sein, L. Mu, U. Fladrich, D. Barbi, P. Gierz, S. Danilov, S. Juricke, G. Lohmann, and T. Jung (2022). "AWI-CM3 coupled climate model: description and evaluation experiments for a prototype post-CMIP6 model". In: *Geoscientific Model Development* 15.16. Publisher: Copernicus GmbH, pp. 6399–6427.

Stuart, K. M. and D. G. Long (2011). "Tracking large tabular icebergs using the SeaWinds Ku-band microwave scatterometer". In: *Deep Sea Research Part II: Topical Studies in Oceanography*. Free-Drifting Icebergs in the Southern Ocean 58.11, pp. 1285–1300.

Swingedouw, D. and P. Braconnot (2007). "Effect of the Greenland ice-sheet melting on the response and stability of the AMOC in the next centuries". In: *Ocean Circulation: Mechanisms and Impacts—Past and Future Changes of Meridional Overturning* 173, pp. 383–392.

Talley, L. D. (2013). "Closure of the global overturning circulation through the Indian, Pacific, and Southern Oceans: Schematics and transports". In: *Oceanography* 26.1, pp. 80–97.

Tarasov, L. and W. R. Peltier (2003). "Greenland glacial history, borehole constraints, and Eemian extent". In: *Journal of Geophysical Research: Solid Earth* 108.B3.

– (2004). "A geophysically constrained large ensemble analysis of the deglacial history of the North American ice-sheet complex". In: *Quaternary Science Reviews* 23.3-4, pp. 359–388.

Thibodeau, B., C. Not, J. Zhu, A. Schmittner, D. Noone, C. Tabor, J. Zhang, and Z. Liu (2018). "Last century warming over the Canadian Atlantic shelves linked to weak Atlantic meridional overturning circulation". In: *Geophysical Research Letters* 45.22, pp. 12–376.

Tournadre, J., N. Bouhier, F. Girard-Ardhuin, and F. Rémy (2016). "Antarctic icebergs distributions 1992–2014". In: *Journal of Geophysical Research: Oceans* 121.1, pp. 327–349.

Trusel, L. D., S. B. Das, M. B. Osman, M. J. Evans, B. E. Smith, X. Fettweis, J. R. McConnell, B. P. Noël, and M. R. van den Broeke (2018). "Nonlinear rise in Greenland runoff in response to post-industrial Arctic warming". In: *Nature* 564.7734, pp. 104–108.

Vizcaíno, M., U. Mikolajewicz, M. Gröger, E. Maier-Reimer, G. Schurgers, and A. M. Winguth (2008). "Long-term ice sheet–climate interactions under anthropogenic greenhouse forcing simulated with a complex Earth System Model". In: *Climate dynamics* 31, pp. 665–690.

Vries, P. de and S. L. Weber (2005). "The Atlantic freshwater budget as a diagnostic for the existence of a stable shut down of the meridional overturning circulation". In: *Geophysical Research Letters* 32.9.

Wallace, J. M. and P. V. Hobbs (2006). *Atmospheric science: an introductory survey*. Vol. 92. Elsevier.

Wang, H., S. Legg, and R. Hallberg (2018). "The effect of Arctic freshwater pathways on North Atlantic convection and the Atlantic meridional overturning circulation". In: *Journal of Climate* 31.13, pp. 5165–5188.

Wang, Q., S. Danilov, D. Sidorenko, R. Timmermann, C. Wekerle, X. Wang, T. Jung, and J. Schröter (2014). "The Finite Element Sea Ice-Ocean Model (FESOM) v. 1.4: formulation of an ocean general circulation model". In: *Geoscientific Model Development* 7.2, pp. 663–693.

Weaver, A. J., J. Sedláček, M. Eby, K. Alexander, E. Crespin, T. Fichefet, G. Philippon-Berthier, F. Joos, M. Kawamiya, K. Matsumoto, et al. (2012). "Stability of the Atlantic meridional overturning circulation: A model intercomparison". In: *Geophysical Research Letters* 39.20.

Weertman, J. (1964). "Rate of growth or shrinkage of nonequilibrium ice sheets". In: *Journal of Glaciology* 5.38, pp. 145–158.

Weijer, W, M. Maltrud, M. Hecht, H. Dijkstra, and M. Kliphuis (2012). "Response of the Atlantic Ocean circulation to Greenland Ice Sheet melting in a strongly-eddying ocean model". In: *Geophysical Research Letters* 39.9.

Willeit, M. and A. Ganopolski (2018). "The importance of snow albedo for ice sheet evolution over the last glacial cycle". In: *Climate of the Past* 14.5, pp. 697–707.

Williams, G., L Herraiz-Borreguero, F. Roquet, T Tamura, K. Ohshima, Y Fukamachi, A. Fraser, L Gao, H Chen, C. McMahon, et al. (2016). "The suppression of Antarctic bottom water formation by melting ice shelves in Prydz Bay". In: *Nature communications* 7.1, p. 12577.

Winkelmann, R, M. A. Martin, M. Haseloff, T. Albrecht, E Bueler, C Khroulev, and A. Levermann (2011). "The Potsdam parallel ice sheet model (PISM-PIK)–Part 1: Model description". In: *The Cryosphere* 5.3, pp. 715–726.

Wise, M., K. Calvin, A. Thomson, L. Clarke, B. Bond-Lamberty, R. Sands, S. J. Smith, A. Janetos, and J. Edmonds (2009). "Implications of limiting CO2 concentrations for land use and energy". In: *Science* 324.5931, pp. 1183–1186.

Yang, Q., T. H. Dixon, P. G. Myers, J. Bonin, D. Chambers, M. Van Den Broeke, M. H. Ribergaard, and J. Mortensen (2016). "Recent increases in Arctic freshwater flux affects Labrador Sea convection and Atlantic overturning circulation". In: *Nature communications* 7.1, p. 10525.

Yau, A. M., M. L. Bender, A. Robinson, and E. J. Brook (2016). "Reconstructing the last interglacial at Summit, Greenland: Insights from GISP2". In: *Proceedings of the National Academy of Sciences* 113.35, pp. 9710–9715.

Zhang, Q., B. Liu, S. Li, and T. Zhou (2023). "Understanding models' global sea surface temperature bias in mean state: from CMIP5 to CMIP6". In: *Geophysical Research Letters* 50.4.